8-2016

Trust-Based Control of (Semi)Autonomous Mobile Robotic Systems

Hamed Saeidi
Clemson University

Recommended Citation

Trust-Based Control of (Semi)Autonomous Mobile Robotic Systems

A Dissertation
Presented to
the Graduate School of
Clemson University

In Partial Fulfillment
of the Requirements for the Degree
Doctor of Philosophy
Mechanical Engineering

by
Hamed Saeidi
August 2016

Advised by:
Dr. Yue Wang, Committee Chair
Dr. Kapil Chalil Madathil
Dr. Ardalan Vahidi
Dr. John R. Wagner

Abstract

Despite great achievements made in (semi)autonomous robotic systems, human participation is still an essential part, especially for decision-making about the autonomy allocation of robots in complex and uncertain environments. However, human decisions may not be optimal due to limited cognitive capacities and subjective human factors. In human-robot interaction (HRI), trust is a major factor that determines humans use of autonomy. Over/under trust may lead to disproportionate autonomy allocation, resulting in decreased task performance and/or increased human workload. In this work, we develop automated decision-making aids utilizing computational trust models to help human operators achieve a more effective and unbiased allocation. Our proposed decision aids resemble the way that humans make an autonomy allocation decision, however, are unbiased and aim to reduce human workload, improve the overall performance, and result in higher acceptance by a human.

We consider two types of autonomy control schemes for (semi)autonomous mobile robotic systems. The first type is a two-level control scheme which includes switches between either manual or autonomous control modes. For this type, we propose automated decision aids via a computational trust and self-confidence model. We provide analytical tools to investigate the steady-state effects of the proposed autonomy allocation scheme on robot performance and human workload. We also develop an autonomous decision pattern correction algorithm using a nonlinear model predictive control to help the human gradually adapt to a better allocation pattern. The second type is a mixed-initiative bilateral teleoperation control scheme which requires mixing of autonomous and manual control. For this type, we utilize computational two-way trust models. Here, mixed-initiative is enabled by scaling the manual and autonomous control inputs with a function of computational human-to-robot trust. The haptic force feedback cue sent by the robot is dynamically scaled with a function of computational robot-to-human trust to reduce humans physical workload.

Using the proposed control schemes, our human-in-the-loop tests show that the trust-based automated decision aids generally improve the overall robot performance and reduce the operator workload compared to a manual allocation scheme. The proposed decision aids are also generally preferred and trusted by the participants. Finally, the trust-based control schemes are extended to the single-operator-multi-robot applications. A theoretical control framework is developed for these applications and the stability and convergence issues under the switching scheme between different robots are addressed via passivity based measures.

Acknowledgments

Publications

- H. Saeidi, and Y. Wang, "Incorporating Trust and Self-Confidence in the Control of Semi-autonomous Robotic Systems", IEEE Transactions on Human Machine Systems, 2015, under review.

- H. Saeidi, J. R. Wagner, and Y. Wang, "Trust-Based Bilateral Teleoperation of Multi-Robot Systems", *submitted to IEEE Conference on Decision and Control*, 2016.

- B. Sadrfaridpour, H. Saeidi, and Y. Wang, "An Integrated Framework for Human-Robot Collaborative Assembly in Hybrid Manufacturing Cells", accepted for presentation in *Conference on Automation Science and Engineering*, 2016.

- H. Saeidi, F. McLane, B. Sadrfaridpour, E. Sand, S. Fu, J. Rodriguez, J. R. Wagner, and Y. Wang, "Trust-Based Mixed-Initiative Bilateral Teleoperation of Mobile Robotic Systems", *American Control Conference*, pp. 6177-6182, Boston, MA, July 5-8, 2016.

- S. Fu, H. Saeidi, E. Sand, B. Sadrfaridpour, J. Rodriguez, Y. Wang, and J. R. Wagner, "A Haptic Interface with Adjustable Feedback for Unmanned Aerial Vehicles (UAVs) Model, Control, and Test", *American Control Conference*, Boston, MA, July 5-8, pp. 467-472, 2016.

- B. Sadrfaridpour, H. Saeidi, J. Burke, K. Madathil, and Y. Wang, "Modeling and Control of Trust in Human-Robot Collaborative Manufacturing", *The Intersection of Robust Intelligence (RI) and Trust in Autonomous Systems*, pp. 115-141, Springer, 2016.

- H. Saeidi, and Y. Wang, "Trust and Self-Confidence Based Autonomy Allocation of Robotic Systems", *IEEE conference on decision and control*, Osaka, Japan, December 15-18, pp. 60526057, 2015.

- N. Wan, S. A. Fayazi, H. Saeidi, and A. Vahidi, "Optimal Power Management of an Electric Bicycle based on Terrain Preview and Considering Human Fatigue Dynamics", *American Control Conference*, June 4-6, Portland, Oregon, USA, 2014.

- B. Sadrfaridpour, H. Saeidi, Y. Wang, and J. Burke, "Modeling and Control of Trust in Human and Robot Collaborative Manufacturing", *Association for the Advancement of Artificial Intelligence Spring Symposium Series*, March 24-26, Stanford, California, USA, 2014.

- H. Saeidi, M. Naraghi, and A. A. Raie, "A neural network self-tuner based on input shapers behavior for anti sway system of gantry cranes", *Journal of Vibration and Control*, vol. 19, no. 13, pp. 1936-1949, 2013.

- H. Saeidi, M. Naraghi, and A. A. Raie, "Design and Implementation of a Neural Network Controller for Anti Sway System of Gantry Cranes", *Journal of Iranian Society of Mechanical Engineers*, vol. 14 , no. 1, pp. 74-94, 2012.

Table of Contents

Table of Contents - Continued

List of Tables

List of Figures

List of Figures - Continued

Chapter 1

Introduction

1.1 Research Motivation and Background

Despite great achievements made in (semi)autonomous robotic systems, human participation is still an essential part for decision-making about autonomy allocation of robots, especially in complex and uncertain environments [27]. That is, human is responsible to determine when to take over the control of robot and for how long. Factors such as environmental disturbances, as well as limited sensing and computing capabilities can lead to poor performance of autonomous controllers [4, 67, 113]. On the other hand, it has been shown that even when all the necessary information is provided, human decisions always have bias and hence may not be optimal due to limited cognitive and learning capacities [12, 21, 40, 51, 100]. Moreover, in many telepresence robotic applications [58, 60, 111], human performance degrades sporadically due to factors such as limited feedback of the remote environment as well as communication delay [17, 31]. Therefore, new breed of robotics control solutions aim to combine the strength of both human and autonomous controllers via (semi)autonomous shared or supervisory control systems [27, 71, 114] to improve the performance and capabilities of the resulting team (Figure 1.1). Furthermore, this has the benefit of reducing manpower and workload of the human operators.

In (semi)autonomous robotics systems, there are various levels of autonomy (LoAs) ranging from simple two-level control (i.e. teleoperation and full autonomy) up to 10 different levels [10, 93] which appear in different types of shared and supervisory control schemes. The main difference between the shared and the supervisory control is that in supervisory control, human generally
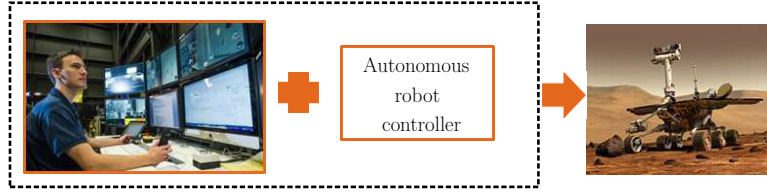
Figure 1.1: Example of (Semi)autonomous Robotic Control Systems

executes commands in an outer loop and mostly adjusts parameters for lower control loops (e.g. determining roles for individual autonomous robots in a team [27]) based on his/her observations; while in shared control, human plays the same role as other autonomous controllers or human operators in a collaborative control scheme (e.g. shared control of a wheelchair [80]). Shared and supervisory control have a wide range of applications in aviation [32], manufacturing [64], transportation [106], rehabilitation and health care [80], robotics ranging from single-operator-single-robot to multiple-operator-multiple-robot architectures [2, 5, 23, 43, 66, 91, 94, 111], and etc. In such applications, various components and LoAs increase the complexity of the system for the human as the primary decision maker in autonomy allocation. Therefore, in most supervisory or shared control robotic systems, automated decision aids have been augmented to help a human operator make better decisions regarding autonomy allocation to the robots [27, 71]. Ideally, these aids should reduce human cognitive workload during decision-making as well as improve performance of the joint human-robot system [77]. However, due to improper human-robot interaction (HRI) and human-automation interaction (HAI), those decision aids have not always been successful in enhancing performance [16]. For example, failure in the speed sensors and the subsequent disengagement of the autopilot, led to confusion of pilots and the crash of Air France 447 in 2009 [112]. Thus, the incorrect reaction of pilots to the problem resulted in the loss of control and the crash. Such issues usually stem from human factors such as reduced situational awareness, decision biases, and improper trust [76]. Thus, it is crucial to consider the human-in-the-loop behaviour when the shared or supervisory control scheme is designed. In this dissertation we focus on the trust related issues as one of the major human factors.

Generally, trust in another person (machine) can be categorized into dispositional trust and history-based trust [70]. The dispositional trust is defined as the initial trust felt upon the first encounter of another person (machine) even without any interaction. The history-based trust, however, is built based on the interactions between the person and another person (machine). In this

dissertation, we consider the history-based trust which is dynamically evolving. The study of role of trust in automation and autonomous agents dates back to the prominent work of Lee and Moray in 1992 [62]. Via a simulated juice production line, they showed how the trust of operators change dynamically after the failures of automation and how it affects the use of manual or autonomous control. Inspired by this work, research on the role of trust in automation and autonomous agents has been extended to different applications such as manufacturing [14, 49, 74], military applications [25, 35], autonomous computer network agents [28], (semi)autonomous cars [106] and robotics [26]. The results indicate that in the shared or supervisory control applications, operators generally tend to use the automated system more often when their trust is higher and vice versa [29]. It has also been shown that improper trust can lead to misuse (underreliance) or disuse (overreliance) of the autonomous system [78]. As shown in Figure 1.2, this can lead to increased workload of human and reduced performance of the joint system. Various types of solutions have been proposed in the literature. Proper training of operators [5], use of anthropomorphic avatars for autonomous agents [75], and calibration of humans trust via situational awareness transparency [15], are some of the examples of these solutions. These works mostly consider the problem from an ergonomic perspective. However, in this dissertation we take a dynamic system approach with focus on mobile robotic systems. Examples of such dynamic and control system perspective solutions include, real-time and dynamic scheduling algorithms for supervision of robots [19, 37, 107, 110], adaptive and flexible manufacturing [82–84], and near real-time human-robot trust measures to adapt mobile robots for higher operator trust [116]. This dissertation particularly seeks the incorporation of unbiased and objective computational models of trust to provide autonomous decision aids about the allocation of autonomy in shared control of mobile robotic systems such that

1. A more efficient allocation of autonomy is achieved by reducing human workload and improving the joint task performance.

2. The autonomous decision-making method remains close to human so as to entail higher acceptance and preference by human operators.

Figure 1.2: The effects of improper trust on the shared control mobile robotic systems.

1.2 Research Contributions

In order to fulfill the goals mentioned at the end of Section 1.1, clear definition of the applications and problems should be given. Throughout this dissertation, these problems are considered from both theoretical and experimental points of view via rigorous mathematical language as well as extensive human-in-the-loop experiments. We utilize several objective measures such as average tracking error during task, human performance, and operator utilization level as well as subjective measures such as perceived task load or trust to evaluate the proposed control schemes. The subjective trust assessment is usually obtained via post-experiment questionnaires [6, 35, 50]. It should be noted that this dissertation does not focus on the methods to measure real-time subjective trust since this topics deserve a separate comprehensive study such as the method given in [116]. In the following, we categorize the contributions of this dissertation in three applications and clarify which problems or research questions are addressed in each category.

1.2.1 Teleautonomous Operations for (Semi)Autonomous Mobile Robotic Systems

This category assumes teleautonomous operations for robot guidance and navigation where a robot can be controlled via switches between an in-situ autonomous robot controller (autonomous control mode) and a skilled human operator through teleoperation (manual control mode). Therefore, the applications that include the decision-making between two alternative control choices are considered. These systems are also called traded control systems [44, 54, 81]. Based on these assumptions, we seek to answer the following questions

- What is a human-like but unbiased decision-making method so as to provide decision aid suggestions to the operator about the allocation of autonomy?

- How can we predict the human workload/utilization level and overall task performance when such a decision suggestion scheme is followed?

- Does an individual accept and prefer such a decision aid suggestion?

- How to help the operator to overcome the bias in individual decision-making via the proposed scheme?

To answer these questions, Chapter 2 incorporates analysis of human trust and self-confidence into the design of automated decision aids for robot autonomy allocation such that an unbiased and more effective control allocation can be achieved. By trust here we mean trust of human to an autonomous robot and self-confidence can be interpreted as the trust of an individual to himself/herself in accomplishing a specific task [63]. Human factors research has shown that in two-level control mode applications considered in this section, humans's use of automation/robots depends on the difference between their trust in automation/robots and their self-confidence in controlling the machine manually with more difference indicating more inclinations towards a specific control mode [49,61,63,115]. As the first contribution of this chapter, a performance-centric, computational trust and self-confidence model based on objective and unbiased measures of human and robot performance, and correspondingly trust and self-confidence based autonomy allocation scheme is proposed. As the second contribution of Chapter 2, quantitative analysis on robot performance and human workload under the proposed trust and self-confidence based control mode allocation scheme is performed. Specifically, bounds on robot performance, dwell time in each mode, as well as bounds on human utilization ratio under steady-state are derived. As the third contribution, experiments are designed using a robot simulator with human-in-the-loop to test the proposed model and control allocation scheme. Test results show that the proposed scheme can capture human decision-making pattern in autonomy allocation on average, improve the overall robot performance and at the same time reduce the operator workload compared to a manual allocation scheme. Moreover, our proposed control allocation scheme is more likely to be accepted compared to a performance maximization scheme and also generally preferred and trusted by the participants compared to both manual and robot performance maximization schemes. Furthermore, as the fourth contribution, a decision pattern correction algorithm is developed based on the trust and self-confidence model to gradually correct human bias in autonomy allocation and improve performance of the joint system. A nonlinear model predictive control (NMPC) [1] corrective control is utilized considering the HRI system dynamics and human incentive models as constraints to ease the adaptation process for human. The details are provided in Chapter 2.

1.2.2 Mixed Initiative Control of (Semi)Autonomous Mobile Robotic Systems

This category considers mixed-initiative bilateral teleoperation. In a mixed-initiative control scheme, a robot control task is shared between human and an in-situ autonomous controller, i.e., the control dynamically blends the manual and autonomous inputs [18, 31, 98, 101, 114]. This blending makes the mixed-initiative method different than the control method in Chapter 2 (briefly introduced in Section 1.2.1) which considers only manual or only autonomous control at each moment. In a bilateral haptic teleoperation scheme, a human operator controls a robot remotely through some control device while receiving a haptic force feedback cue (such as [36, 58]) so that the operator can control the robot more effectively [2, 69, 73]. To combine strengths of both the bilateral teleoperation and mixed-initiative schemes, in Chapter 3, we develop a trust-based mixed-initiative bilateral teleoperation scheme for shared manual and autonomous control with haptic feedback in mobile robot applications. The research questions of interest in this category include:

- What is a suitable theoretical and practical framework to incorporate human-like decision-making in the proposed scheme such that overall task performance increases and both physical and cognitive workloads of human decrease?

- How can we guarantee the stability of such a complex system when different components of the system vary based on trust while the overall system is on the fly?

- Does the human accept and prefer such a decision aid method?

To address these questions, in Chapter 3, the blending between manual and autonomous control will be mediated by human-to-robot trust and the intensity of the haptic force feedback will be adjusted according to robot-to-human trust. Built on the literature, computational models of two-way trust, i.e., human-to-robot trust and robot-to-human trust, are utilized as metrics to dynamically adjust the control authorities between manual and autonomous control as well as the level of haptic feedback provided to the operator for improved joint performance. This is the first contribution of Chapter 3. The force feedback is scaled down when the robot-to-human trust is higher so that the operator perceives smaller forces and hence reduces physical workload [20]. The proposed scheme entails major changes in two key components compared to the conventional bilateral teleoperation: the communication channel and the slave side. These changes are due to the introduction of variable

scales for both control inputs and haptic cues. Improper implementation of these changes can lead to stability issues of the overall control scheme. Therefore, as a common tool in teleoperation systems, we perform passivity analysis for the overall trust-based mixed-initiative bilateral teleoperation scheme. The passivity theory provides an energy-based perspective to analyze system property which under mild assumptions conveys system stability [45, 95]. As the second contribution of Chapter 3, we propose a wave/scattering transformation such that a passive, and hence stable, communication channel is established between the master device and the teleoperated slave robot in the presence of variable power scaling and time-varying delays. We also guarantee passivity of the slave robot in the presence of scaled local autonomous control and artificial force feedback algorithm via passivity observers (PO) and passivity controllers (PC).

Usually, when passivity-based methods are utilized in the teleoperation schemes, signal transparency is scarified in order to guarantee stability. Thus, there is usually a challenge to adjust the parameters and gains inside the control loop to make a balance between stability and transparency [46]. We address this problem for the proposed trust-based scheme via theoretical extensions that deal with general guidelines for the adjustment of several parameters inside the proposed scheme such that the transparency of velocity commands and force feedback cues are improved during the passivation process. We also extend the design of a feedback r-passivity scheme for the haptic controller device such that the haptic device allows a wider range of force feedback scaling while still the passivity and stability of the entire scheme is guaranteed. This helps to improve the quality of force feedback perception by the operator.

Finally, the trust-based mixed-initiative teleoperation scheme has been experimentally tested via an experimental setup developed in the Interdisciplinary and Intelligence Research (I^2R) lab which utilizes real robots including a Parrot AR. Drone. 2.0 UAV and a Khepera III ground robot. The results indicate the effectiveness of our proposed scheme in improving task performance and reducing operator workload compared to the exclusively bilateral teleoperation (see Chapter 3 for full details). This method is also preferred and trusted by the participants compared to a manual teleoperation, a mixed-initiative bilateral schema with manual control allocation, and a performance maximization scheme.

1.2.3   Bilateral Teleoperation of (Semi)Autonomous Multi-Robot Systems

As the final step in this dissertation, we build on our previous contributions briefly discussed earlier in Sections 1.2.1 and 1.2.2 and develop a trust-based control scheme for applications in bilateral teleoperation in single-operator-multiple-robot systems. Such systems aim to reduce the manpower by allowing one operator to control a team of robots and also increase the robustness and flexibility by including several team members [27]. In the multiple-robot framework considered in this dissertation, trust-based measures are utilized to help the human to switch between different robots and control them in order to improve the task performance [33] [92]. In this situation, due to the switching in the components of the teleoperation, instability issues may occur that prevents implementation of the proposed scheme. In general, instability may occur in switched dynamics systems even if all of the subcomponents of such a system exhibit stable internal dynamics [9]. Therefore, by incorporating a trust-based control in the single-operator-multiple-robot we try to answer the following questions

- What is a suitable decision aid and control framework to incorporate a human-like decision-making in the multi-robot systems for increased task performance and reduced workload of human?

- For such a system, how can we guarantee the overall stability while real-time trust-based adjustments on the structure and different components of the system are implemented?

In order to answer these questions, in Chapter 4, human-to-robot trust is used in order to select a new leader robot to be controlled by human within a specific time period. Similar to the Section 1.2.2, the force feedback cues are scaled with a variable scale as a function of robot-to-human trust in order to help the operator with various levels of feedback and reduce the physical workload. In order to guarantee the stability under the effects of delay as well as trust-based switching and variable scaling, we perform passivity analysis for the overall system. Moreover, we guarantee a passive smooth filtering of the discontinuities in the velocity and force feedback signals in order to reduce the confusion of operator. Such discontinuities occur due to the switching between different leaders. Finally, for the developed scheme, we prove a good collective position tracking and synchronization performance of the multi-robot system. These contributions are discussed in detail in Chapter 4

1.3 Dissertation Outline

The organization of the rest of this dissertation is as follows. First a trust and self-confidence based autonomy allocation scheme for teleautonomous operations is presented in Chapter 2. Chapter 3 presents the two-way trust-based control allocation scheme for mixed-initiative bilateral teleoperation applications. We extend the trust-based control schemes to the multi-robot applications in Chpater 4. Finally, Chapter 5 poses ongoing and open problems discovered during this dissertation and concludes this manuscript.

Chapter 2

Incorporating Trust and Self-Confidence Analysis in the Guidance and Control of (Semi)autonomous Mobile Robotic Systems

2.1 Introduction

As it was mentioned in Section 1.2.1, this chapter considers the analysis of human trust and self-confidence into the design of automated decision aids for robot autonomy allocation. Teleautonomous applications in robot guidance and navigation are studied here in which a robot can be controlled through switches between an in-situ autonomous robot controller (autonomous control mode) and a skilled human operator through teleoperation (manual control mode). In such two alternative choice applications (also called as traded control [44, 54, 81]), it has been found that when humans use automation/robots, the difference between their trust in automation/robots and their self-confidence in controlling the machine determines their use of automation/robots [49, 63, 115].

Due to innate individual bias [63], manual autonomy allocation may lead to disproportionate allocation and consequent autonomy misuse (overreliance) or disuse (underreliance) [52, 77]. Although a considerable amount of work has been done in HRI for improving task performance from a physical perspective [11], human cognitive aspects have rarely been addressed and quantified. Therefore, as the first contribution of this chapter, we propose a performance-centric, computational trust and self-confidence model based on objective and unbiased measures of human and robot performance, and correspondingly trust and self-confidence based autonomy allocation scheme to avoid misuse/disuse [76]. Different from other optimal autonomy allocation schemes [3,18,98], because our proposed scheme follows human autonomy allocation pattern, higher user acceptance is expected. Our experiment results, presented in Section 2.4.1.3, support this hypothesis.

Although previous related works [28, 38, 63] have studied human decision-making models and autonomy allocation affected by trust and self-confidence, there lacks analytical evaluation of the effects of such autonomy allocation schemes on robot performance and human workload. While in this chapter, as the second contribution, we provide a detailed analysis on the joint human-robot system dynamics in a rigorous mathematical framework. Specifically, we derive bounds on robot performance, dwell time in each mode, as well as bounds on human utilization ratio under steady-state under the proposed trust and self-confidence based control mode allocation scheme. As the third contribution, two experiments are designed via robot simulators with human-in-the-loop to examine the proposed model and control allocation scheme. The experiment results show that the proposed scheme can capture human decision-making pattern in autonomy allocation on average. The experiments also indicate that under the proposed scheme, the overall robot performance increases by 11.76% and at the same time the operator's perceived workload reduces by 10.07% compared to a manual allocation scheme. Moreover, our proposed control allocation scheme is 23.42% more likely to be accepted compared to a performance maximization scheme and also generally preferred and trusted by the participants compared to both manual and robot performance maximization schemes.

Finally, based on the trust and self-confidence model, an automated decision pattern correction algorithm is proposed to correct human bias in autonomy allocation gradually in order to improve performance of the system. We utilize human incentives models from behavioral science [8, 53] to ease the adaptation process. These models consider the operator's perceived value of robot performance as well as his/her natural tendency of avoiding cognitive effort. Compared to other human decision-making pattern correction algorithms in robotic applications [13, 99], we

incorporate the models of human incentive to avoid abrupt or forced changes in human decision-making pattern, which eliminates human confusion as well as resistance to pattern correction [13]. We derive the pattern correction algorithm based on nonlinear model predictive control (NMPC) [1] considering the HRI system dynamics and human incentive models as constraints. This algorithm gradually suggests new decision thresholds to the human operator so as to modify their decision pattern. This algorithm is also examined experimentally.

The organization of the rest of the chapter is as follows. Section 2.2 describes the trust and self-confidence model. Section 2.3 presents a trust and self-confidence based control mode allocation scheme and analysis. Section 2.4 presents a human subject experiment to test the analytical results of Sections 2.2 and 2.3. We present the NPMC pattern correction algorithm in Section 2.5 and conclude the chapter in Section 2.6.

2.2 Human-to-Robot Trust and Human Self-Confidence (TSC) Model

In this section, we develop the trust and self-confidence model (2.1), called TSC, and present the linear and nonlinear models of robot and human performances utilized in the TSC model. We rely on results from well-acknowledged human factors research [38, 63] to develop the TSC model. These models simplify the HRI dynamics, while still keeping the essence of the problem and are appropriate for high-level abstraction and decision-making. We show how these simple models can account for experimental data and hence justify their applicability[1]. To the best of the authors' knowledge, the analytical and experimental study of trust and self-confidence based autonomy allocation has not been well explored in the literature. Therefore, in this work, we seek to develop such a robot control allocation scheme and experimentally validate the effectiveness of the proposed scheme.

2.2.1 TSC model

We develop a performance-centric, computational TSC model to describe the difference between human-to-robot trust and human self-confidence. First, we introduce the general process

---

[1]More complex stochastic models can be developed to capture the uncertainty in human behaviors, which however will make the HRI system dynamics very difficult for analysis and probably result in biased and uncertain decisions. These are exactly what we want to avoid in the allocation scheme.

of how a human allocates autonomy. The authors in [38, 63] found through experiments that a human operator's choice between autonomous control and manual control is based on three major factors: i) the difference between trust in the autonomous controller and self-confidence in controlling the system manually, ii) individual bias towards autonomous or manual control, and iii) small stochastic uncertainty due to imperfect perception of capabilities of autonomous or manual control. However, factors (ii) and (iii) are not desirable since they can introduce disproportionate control allocation and consequent machine misuse (overreliance) or disuse (underreliance). To overcome such misuse/disuse, we propose the following two solution steps:

- Step 1: Developing a human-like control allocation scheme while eliminating the negative effects of individual bias and perception uncertainty (Sections 2.2 and 2.3).

- Step 2: Helping the human operator to adapt to an improved autonomy allocation pattern based on the developed control allocation scheme (Section 2.5).

In Step 1, we first develop a performance-centric, computational trust and self-confidence model called TSC. Robot performance has been shown as a key factor that affects human-to-robot trust [26, 41]. Meanwhile, when a human has high (low) performance on a task, their self-confidence is high (low) accordingly [26]. Therefore, to describe the difference between trust and self-confidence, under a performance-centric criteria, we propose the following TSC model as a function of both human and robot performance:

$$TSC(k) = a_T P_r(k) - b_T P_h(k), \tag{2.1}$$

where $P_r(k)$ and $P_h(k)$ are robot and human performance. The performance will be objectively measured in real-time so as to computationally evaluate the TSC model without human bias and/or uncertainty. We define a_T and b_T as

$$a_T = \frac{\overline{P}_h + \underline{P}_h}{\overline{P}_r \overline{P}_h - \underline{P}_r \underline{P}_h} > 0, \quad b_T = \frac{\overline{P}_r + \underline{P}_r}{\overline{P}_r \overline{P}_h - \underline{P}_r \underline{P}_h} > 0, \tag{2.2}$$

where $\overline{P}_r$ and $\underline{P}_r$ are the maximum and minimum robot performance, and $\overline{P}_h$, $\underline{P}_h$ are the maximum and minimum human performance. These choices of a_T and b_T normalize the values of TSC within $[-1, 1]$ for the sake of analysis.

13

Remark 1 *Notice that the $TSC(k)$ model (2.1) does not necessarily reflect the actual trust and self-confidence, which is subjective, latent and often difficult to measure directly and model precisely. The computational model we propose here uses objective measurements of robot and human performance. It does not include individual bias or decision uncertainty and is hence objective, deterministic, and can reflect robot and human trustworthiness, respectively. Our goal is to provide a performance-centric evaluation of trust and self-confidence in the control of mobile robots for trajectory tracking and navigation applications. Based on this objective TSC model, we will design an unbiased decision aid to help the operator improve performance. Unlike other performance-based control allocation schemes [13, 47, 56], the TSC-based scheme is human-like and hence has higher user acceptance (to be examined experimentally in Section 2.4.1.3).* ●

2.2.2   Robot Performance Model

In order to present the robot performance model, we make the following assumptions according to data collected from field robotics experiments [24]:

Assumption 1 *Consider a semi(autonomous) mobile robot in applications such as surveillance, trajectory tracking, and exploration within an environment with a fixed level of complexity. When such a robot is left in the autonomous mode and neglected for a long time, its performance in terms of domain exploration, trajectory tracking, and object detection decays over time and converges to a minimum value. Factors such as environmental disturbance, limited sensing and computing capabilities can lead to such a gradual performance degradation. For example, in a trajectory tracking task, the accuracy of odometry data for ground robots degrades with time because of accumulative measurement error, which will result in a gradual increment of navigation error [113].*

Assumption 2 *When a skilled human operator keeps controlling the robot, because of human's superior capabilities in vision processing, cognitive reasoning, and flexibility in maneuvering robot motion, the robot performance increases over time. Furthermore, if the operator performance is lower, they are less efficient in controlling the robot and hence the robot performance will increase at a slower rate.*

14

Based on *Assumptions 1 and 2*, we propose the following model for abstracting high-level robot performance:

$$P_r(k+1) = a_{pr}P_r(k) + (1-a_{pr})\underline{P}_r + M(k)b_{pr}P_h(k), \tag{2.3}$$

where $a_{pr} \in (0,1)$, b_{pr} are some positive constant, and $M(k) \in \{0,1\}$ changes according to the control mode with $M(k) = 1$ for the manual mode and $M(k) = 0$ for the autonomous mode. For any $0 < a_{pr} < 1$, when the autonomous mode is activated, i.e. $M(k) = 0$, the robot performance decreases over time and converges to $\underline{P}_r$. To guarantee that under the manual mode ($M(k) = 1$), the robot performance can increase up to $\overline{P}_r$ when the human performance is maximum (i.e. $P_h = \overline{P}_h$), we choose $b_{pr} = (1-a_{pr})\frac{\overline{P}_r - \underline{P}_r}{\overline{P}_h}$. Thus, with lower human performance (i.e. $\underline{P}_h < P_h < \overline{P}_h$), the robot performance is a value between $(\underline{P}_r, \overline{P}_r)$.

Remark 2 *In this chapter, we focus on navigation and tracking tasks for mobile robots given the robot characteristics and control algorithms implemented to allow its autonomy. The model (2.3) abstracts the high-level robot performance such as average trajectory tracking accuracy or average navigated area in the task space, which is in harmony with other well-acknowledged robotics research (see Fig. 6 in [22] as an example). This type of high-level robot performance is usually evaluated over a finite observation window and represent an average behaviour of the system dynamics in this time window [79, 96] (see Fig. 2.3 for example). The instantaneous performance of robot, however, is noisy and does not specifically follow any linear model. Note that different humans and robots have different values for $\overline{P}_r$, $\underline{P}_r$, $\underline{P}_h$, $\overline{P}_h$.* •

To better explain and justify the model, below we give an example of the robotic applications considered in this chapter.

Trajectory Tracking Example Consider an experimental testbed as shown in Fig. 2.1, which consists of a Stage real-time robot simulator (http://playerstage.sourceforge.net/), a Logitech joystick controller, a control panel, and performance GUI. These components are integrated via the Robot Operating System (ROS) (http://www.ros.org/). The Stage simulator simulates a Pioneer ground mobile robot along with its working environment, and the joystick allows the operator to control the robot in the manual mode and activate (deactivate) the autonomous robot controller. The human operator can control the robot along a desired trajectory between the guide posts. The

robot can also use its laser scanner to navigate along the trajectory autonomously, via finding the guide posts. The autonomous controller consists of two proportional controllers that correct the heading and linear velocities of the robot based on positions of the guide posts detected by the laser scanner. The robot keeps moving towards the guide posts in order to find the next part of the trajectory. The performance GUI and the control panel will be used to help the participants with the control allocation of robot (see Section 2.4).
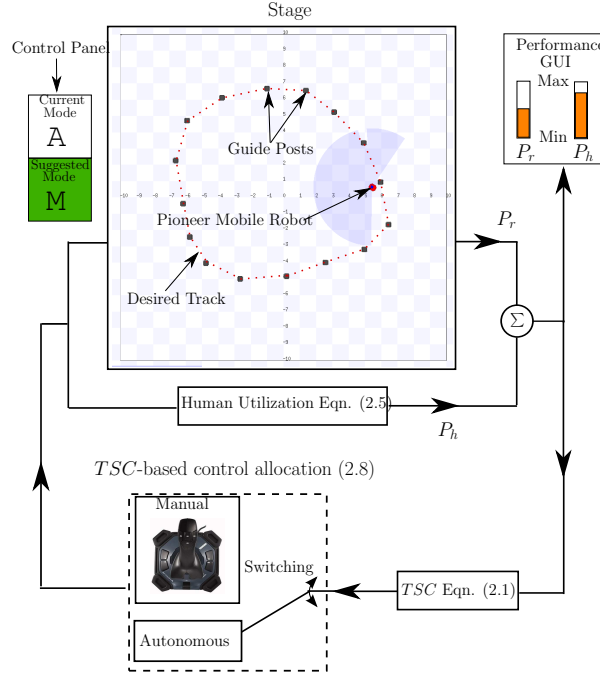
Figure 2.1: Trajectory tracking example testbed.

The task goal is to control the robot as fast and close to the desired trajectory as possible. We use the average traveled distance close to and along the desired trajectory over a finite and moving time window as a metric to evaluate robot performance [79]. The robot performance can therefore be measured in real-time by the following expression

$$Z_{P_r}(k) = \frac{1}{W} \sum_{i=k-W}^{k} \Delta d(i) \frac{e_{\max} - e(i)}{e_{\max}}, \tag{2.4}$$

where k is the current moment, W is the length of the moving time window, $\Delta d(i)$ is the distance traveled in one time step i, $e_{\max}$ is the maximum acceptable deviation from the desired trajectory and $e(i)$ is the tracking error (deviation) from the trajectory at moment i. Therefore, larger tracking

error and smaller traveled distance result in a lower robot performance. In this case study, based on the dimensions of the environment, trajectory and the robot, $e_{\max}$ is chosen as 2 meters such that a good performance measure for this task can be obtained.

Now let us compare the trajectories in Fig. 2.2. It can be observed from the figure that a skilled human operator shows better maneuverability than the autonomous controller when controlling the robot to follow the desired trajectory. This is probably because that the use of laser scanner limits both range and accuracy for finding the posts in the autonomous controller. Therefore, when the robot is left in the autonomous mode, the average traveled distance along the desired trajectory gradually reduces to a minimum value. On the other hand, when the human takes over the control of robot, he (she) can in general increase the robot performance. Hence, based on the performance measure Z_{P_r}, the evolution of robot performance P_r satisfies *Assumptions 1 and 2*.
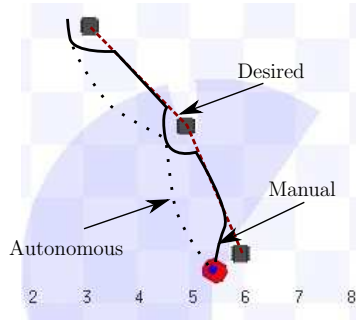
Figure 2.2: Comparison of robot trajectories: desired trajectory (red dashed curves), trajectory under manual control (black curves), and trajectory under autonomous control (dotted black curves).

We performed an identification process for a pilot operator to find the values of parameters (a_{pr}, b_{pr}, $\underline{P}_r$ and $\overline{P}_r$) in model (2.3) such that the robot performance $P_r(k)$ curve fits the measurements $Z_{P_r}(k)$ collected and calculated according to (2.4) for the trajectory tracking example. Figs. 2.3a and b show the identification results. During the identification experiments, the operator first controls the robot in the manual mode and takes the robot performance to the maximum value. After that, the robot is left for a long enough time to reach the minimum performance. We used a $W = 100$ second time window and a sample time of 0.1 second. Then, the collected data and the model structure (2.3) are used in the MATLAB System Identification Toolbox [104] to identify the unknown model parameters. Using the Auto Regressive and Extra Input (ARX) model fitting method in this toolbox, the parameters are obtained: $\underline{P}_r = 0.24$, $\overline{P}_r = 0.39$, $a_{pr} = 0.996$, $b_{pr} = 0.0013$. This set of parameters are obtained for the pilot operator. These processes were
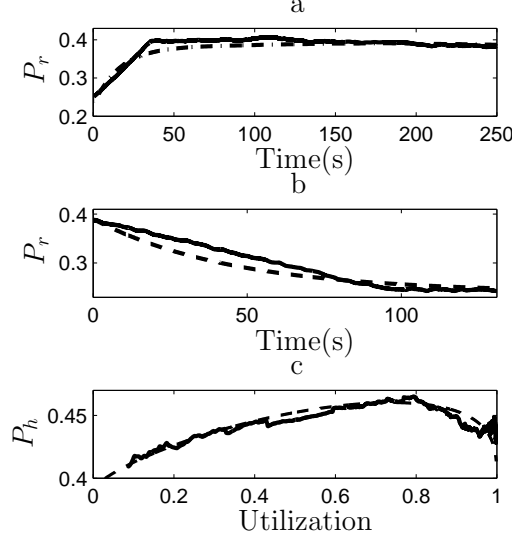
Figure 2.3: Identification of: a) robot performance under manual control, b) robot performance under autonomous control, c) human performance. Solid lines show measurements, and dashed lines show fitted models.

repeated for each participant in the experimental study presented in Section 2.4 (see Table 2.1).

2.2.3 Human Performance Model

Next, we present the model for the performance of a skilled operator when controlling the robot via a control device such as joystick. This model considers the performance of the operator in sending correct control commands to the robot. We first define the utilization ratio of human operator, $r(k)$, as an indication of the amount of time that the human operator has been busy with controlling the robot [88, 108]:

$$r(k + 1) = a_r r(k) + b_r M(k),$$

$$a_r = 1 - \frac{1}{\tau} \in (0, 1), \quad b_r = \frac{1}{\tau} \in (0, 1), \tag{2.5}$$

where τ is the time constant [108]. With this model, under manual control (i.e. $M(k) = 1$) the utilization $r(k)$ gradually increases and under autonomous mode (i.e. $M(k) = 0$) it gradually decreases within $[0, 1]$. Further, we define $\beta \in (0, 1)$ as an index of task difficulty and a smaller β represents a more difficult task [108]. Here, we use the following nonlinear human performance model based on Yerkes-Dodson (YD) law [117] which describes the relationship between the human

18

arousal (represented by the utilization ratio $r(k)$ [88]), task difficulty, and performance

$$P_h(k) = (\overline{P}_h - \underline{P}_h) \left(\frac{r(k)}{\beta}\right)^\beta \left(\frac{1 - r(k)}{1 - \beta}\right)^{1-\beta} + \underline{P}_h. \tag{2.6}$$

The human performance is $P_h(k)$ bounded between $[\underline{P}_h, \overline{P}_h]$. Initially, $P_h(k)$ increases with $r(k)$. As $r(k)$ exceeds β, i.e., an optimal level of workload, $P_h(k)$ decreases [108].

In the trajectory tracking example of Fig. 2.1, the human performance is evaluated as the average maneuverability of the operator with the joystick controller over the same fixed time window W. More specifically, the operator's performance is evaluated by the effectiveness of velocity commands s/he sends to the robot in order to keep it moving fast and close to the desired trajectory. The real-time human performance measure chosen for this experiment is

$$Z_{P_h}(k) = \frac{1}{W} \sum_{i=k-w}^{k} \left[vel(i) \frac{e_{\max} - e(i)}{e_{\max}} + \omega(i) \frac{e(i)}{e_{\max}} \right], \tag{2.7}$$

where $vel(i)$ and $\omega(i)$ are the linear and angular velocity commands sent to the robot and other variables are defined same as before. With this performance metric, if the human is unable to control the robot fast or close to the trajectory, the performance is lower.

During the manual trajectory tracking experiment introduced in Section 2.2.2, we also identified the model parameters (a_r, b_r, $\underline{P}_h$, $\overline{P}_h$ and β) in Equations (2.5) and (2.6) such that the obtained model (i.e. $P_h(k)$ versus $r(k)$ curve) fits the measurements collected using the $Z_{P_h}(k)$ measure in (2.7). The result for the pilot operator is shown in Fig. 2.3c. We used the same time window W and sample time as in the robot performance identification test. Using the nonlinear model fitting method "PEM" in the MATLAB System Identification Toolbox, we identified the parameters for the pilot operator: $\underline{P}_h = 0.391$, $\overline{P}_h = 0.4602$, $a_r = 0.9991$, $b_r = 0.0009$, $\beta = 0.74$. Similar process was repeated for each participant (see Table 2.1).

2.2.4 Joint Human-Robot System TSC Analysis

Let us now consider the relationship of TSC with respect to the system states P_r and r. According to Equation (2.1) and as shown in Fig. 2.4, when $r = \beta$ (i.e. the human performance is $\overline{P}_h$) and $P_r = \underline{P}_r$, the TSC value is minimum ($TSC = -1$). When $r = 0$ (no human intervention, i.e. under-utilized human) or $r = 1$ (over-utilized human), the human performance is $\underline{P}_h$, and

19

$P_r = \overline{P}_r$, TSC is maximum ($TSC = 1$). TSC is bounded in $(-1, 1)$ for any other situations.
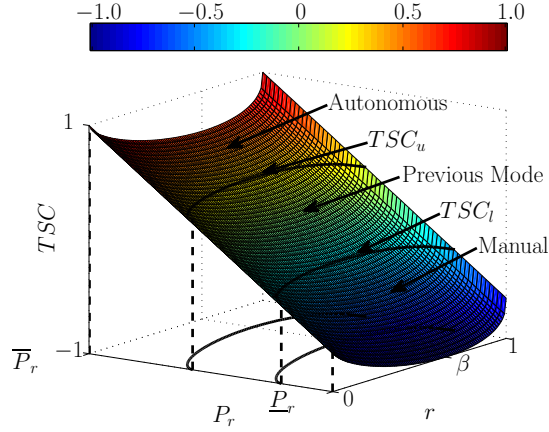
Figure 2.4: TSC-based control mode switching rule.

Based on dynamics (2.3), (2.5) and (2.6), we can show that an exclusively autonomous control mode (i.e. $M(k) = 0$, $\forall k$) results in steady-state utilization $r_{ss} = 0$, human performance $P_{hss} = \underline{P}_h$, and robot performance $P_{rss} = \underline{P}_r$. An exclusively manual control mode in turn results in the following steady-state values: $r_{ss} = 1, P_{hss} = \underline{P}_h, P_{rss} = \underline{P}_r + \frac{\overline{P}_r - \underline{P}_r}{\overline{P}_h}\underline{P}_h$. Thus, the exclusively autonomous mode and the exclusively manual mode end in undesirable human utilization and low robot performance as a result of human under-utilization and over-utilization, respectively. To avoid such situations, in Section 2.3 we will develop a TSC-based scheme to switch between these two control modes. To conclude the current section, we make the following assumption to be used in the derivation of the TSC-based allocation scheme.

Assumption 3 *Since the dynamics of $r(k)$, $P_h(k)$, $P_r(k)$ and $TSC(k)$ are governed by continuous and bounded functions in Equations (2.3), (2.5) and (2.6), we can assume that the rates of change of these variables are bounded:*

(a) $\Delta r(k) \triangleq r(k+1) - r(k), |\Delta r(k)| \leq \delta_r$

(b) $\Delta P_h(k) \triangleq P_h(k+1) - P_h(k), |\Delta P_h(k)| \leq \delta_{P_h}$

(c) $\Delta P_r(k) \triangleq P_r(k+1) - P_r(k), |\Delta P_r(k)| \leq \delta_{P_r}$

where $\delta_r > 0$, $\delta_{P_h} > 0$, and $\delta_{P_r} > 0$ are the absolute values of the maximum changes of $r(k)$, $P_h(k)$, and $P_r(k)$ in one time step, respectively. Accordingly, the rate of change of TSC in one time step is bounded by

20

(d) $\Delta TSC(k) \triangleq TSC(k+1) - TSC(k), |\Delta TSC(k)| \leq \delta_{TSC}$, *with* $\delta_{TSC} > 0$.

Remark 3 *The value of* $\Delta TSC(k)$ *is assumed to be bounded by* $\delta_{TSC} > 0$ *because* TSC *is a function of* P_r *and* P_h *which have bounded changes at each time step as a result of stable and bounded dynamics in Equations (2.3), (2.5) and (2.6). The value of* δ_{TSC} *can be calculated using the values of* δ_{P_h} *and* δ_{P_r} *and Equation (2.1), i.e.* $\delta TSC = \max(|a_T \delta_{P_r} - b_T \delta_{P_h}|) = a_T \delta_{P_r} + b_T \delta_{P_h}$. *The values of* δ_{P_h} *and* δ_{P_r} *can be obtained by finding the maximum* $\Delta P_h(k)$ *and* $\Delta P_r(k)$ *from the fitted curves of system dynamics (2.3), (2.5) and (2.6). Since these parameters are time-invariant,* δ_{TSC} *is fixed for the corresponding* TSC*-based control allocation scheme given the system dynamics. As an example, for the pilot operator the values* $\delta P_r = 0.00069$, $\delta P_h = 0.00021$ *are obtained and hence* δ_{TSC} *is calculated as* 0.0084, *which is a small value compared to the* $[-1, 1]$ *range for* TSC. $\quad\bullet$

2.3 TSC-Based Switching Control & Bounds on Robot Performance and Human Utilization

2.3.1 TSC-Based Switching Control for Mode Allocation

We propose the following control mode switching rule

$$
M(k) = \begin{cases} 0 & \text{if } TSC(k) \geq TSC_u \\ 1 & \text{if } TSC(k) \leq TSC_l \\ M(k-1) & \text{otherwise,} \end{cases} \tag{2.8}
$$

where TSC_l and TSC_u are the lower and upper decision thresholds. Fig. 2.4 illustrates the decision rule (2.8) on the $r - P_r$ plane, where the system switches to the manual mode if the TSC level is below TSC_l, to the autonomous mode if TSC is above TSC_u, and remains in the previous mode in other cases. This switching rule resembles the way that humans allocate autonomy [38], i.e. when TSC is low (can be negative), humans rely on themselves to accomplish a task and vice versa. In Section 2.4, we design experiments to test and show the consistency of the proposed TSC-based scheme (2.8) with human autonomy allocation behaviour. Here, we first investigate conditions to guarantee that the switching rule (2.8) is feasible, i.e. we examine if the choices of decision thresholds TSC_l and TSC_u are reachable given the system dynamics (2.1), (2.3), (2.5), and (2.6). In other words, TSC_u (TSC_l) should not be chosen too high (low) such that these levels are reachable in

finite time. This makes sure that if $TSC(k)$ reaches TSC_u at some time k, the system will choose the autonomous mode and keep this mode till $TSC(k)$ drops to TSC_l again. On the other hand, if $TSC(k)$ reaches TSC_l, the system will choose the manual mode and keep this mode till $TSC(k)$ reaches TSC_u. Otherwise, a regular switching will not occur and the resulting single control mode will drive the system to either the under-utilization or over-utilization of human.

The conditions to guarantee switches are derived in the form of the lower (upper) bounds on TSC_l (TSC_u), i.e. TSC_{lb} (TSC_{ub}) given by Equation (2.9) (Equation (2.10)) are provided in the following theorem.

Theorem 1 *If the decision thresholds are chosen such that $TSC_{lb} < TSC_l < TSC_u < TSC_{ub}$, where TSC_{lb} and TSC_{ub} are given by Equations (2.9) and (2.10), the switching rule (2.8) can be activated regularly.*

$$TSC_{lb} \triangleq a_T b_1' - b_T \underline{P}_h, \quad b_1' \triangleq \underline{P}_r + \frac{b_T \delta_{p_h}}{a_T(1 - a_{pr})}. \tag{2.9}$$

$$TSC_{ub} = \begin{cases} a_3' \overline{P}_h + b_3' & \text{if } a_3' < 0 \\ b_3' & \text{if } a_3' = 0 \\ a_3' \underline{P}_h + b_3' & \text{if } a_3' > 0, \end{cases} \tag{2.10}$$

$$a_3' \triangleq a_T \frac{b_{pr}}{1 - a_{pr}} - b_T, \ b_3' \triangleq a_T \left(\underline{P}_r - \frac{b_T \delta_{P_h}}{a_T(1 - a_{pr})} \right).$$

We first present the following lemmas the results of which are used to prove the theorem.

Lemma 1 *Given the TSC model (2.1) and HRI system dynamics (2.3), (2.5) and (2.6), we have $\Delta TSC(k) < 0$ under $M(k) = 0$ if TSC_l is chosen such that $TSC_l > TSC_{lb}$ where TSC_{lb} is defined as in Equation (2.9).*

Proof. Given the $TSC(k)$ in Equation (2.1) and the lower bound TSC_{lb} of TSC_l in Equation (2.9), we have

$$
\begin{aligned}
TSC(k) &> TSC_{lb} \\
a_T P_r(k) - b_T P_h(k) &> a_T b_1' - b_T \underline{P}_h \\
a_T P_r(k) &> a_T b_1' + b_T(P_h(k) - \underline{P}_h),
\end{aligned}
$$

22

and since $a_T > 0, b_T > 0$, and $P_h \geq \underline{P}_h$ we obtain $P_r(k) > b_1'$. The change in robot performance is given by

$$\Delta P_r(k) = (1 - a_{pr})(\underline{P}_r - P_r(k)) + M(k)b_{pr}P_h(k).$$

Hence, the change in $TSC(k)$ based on Equation (2.1) is

$$\Delta TSC(k) = a_T((1 - a_{pr})(\underline{P}_r - P_r(k)) + M(k)b_{pr}P_h(k)) - b_T \Delta P_h(k). \qquad (2.11)$$

Based on *Assumption 3(b)*, $\Delta TSC(k)$ in Equation (2.11) under $M(k) = 0$ is upper bounded by

$$\Delta TSC(k) \leq a_T(1 - a_{pr})(\underline{P}_r - P_r(k)) + b_T \delta_{p_h}. \qquad (2.12)$$

Because $P_r(k) > b_1'$, we have

$$a_T(1 - a_{pr})P_r(k) > a_T(1 - a_{pr})b_1'$$
$$a_T(1 - a_{pr})P_r(k) > a_T(1 - a_{pr})\underline{P}_r + b_T \delta_{p_h}$$
$$\text{or, } a_T(1 - a_{pr})(\underline{P}_r - P_r(k)) + b_T \delta_{p_h} < 0$$

which implies that the upper bound (2.12) is negative, and then $\Delta TSC(k) < 0$ is satisfied. ∎

Lemma 2 *Given the TSC model (2.1) and HRI system dynamics (2.3), (2.5) and (2.6), we have $\Delta TSC(k) > 0$ under $M(k) = 1$ if TSC_u is chosen such that $TSC_u < TSC_{ub}$ where TSC_{ub} is defined as in Equation (2.10).*

Proof. We begin the proof when $a_3' < 0$. Given the upper bound TSC_{ub} of TSC_u in Equation (2.10), we have

$$TSC(k) < TSC_{ub} = a_3'\overline{P}_h + b_3' \leq a_3'P_h(k) + b_3'.$$

Similarly, for $a_3' = 0$, we have $TSC(k) < b_3' = a_3'P_h(k) + b_3'$. Finally, for $a_3' > 0$, we have

$$TSC(k) < a_3'\underline{P}_h + b_3' \leq a_3'P_h(k) + b_3'.$$

Substituting a'_3 and b'_3 into $TSC(k) < a'_3 P_h(k) + b'_3$ and combining with Equation (2.1) gives

$$
\begin{aligned}
a_T P_r(k) - b_T P_h(k) &< \left(a_T \frac{b_{pr}}{1 - a_{pr}} - b_T \right) P_h(k) + a_T \left(\underline{P}_r - \frac{b_T \delta_{P_h}}{a_T(1 - a_{pr})} \right), \\
a_T P_r(k) &< a_T \frac{b_{pr}}{1 - a_{pr}} P_h(k) + a_T \left(\underline{P}_r - \frac{b_T \delta_{P_h}}{a_T(1 - a_{pr})} \right), \\
P_r(k) &< a'_2 P_h(k) + b'_2,
\end{aligned}
$$

where $a'_2 \triangleq \frac{b_{pr}}{1 - a_{pr}}$ and $b'_2 \triangleq \underline{P}_r - \frac{b_T \delta_{P_h}}{a_T(1 - a_{pr})}$. Based on *Assumption 3(b)*, $\Delta TSC(k)$ in Equation (2.11) under $M(k) = 1$ is lower bounded by

$$
\Delta TSC(k) \geq a_T((1 - a_{pr})(\underline{P}_r - P_r(k)) + b_{pr} P_h(k)) - b_T \delta_{P_h}. \tag{2.13}
$$

Because $P_r(k) < a'_2 P_h(k) + b'_2$, we have

$$
a_T(1 - a_{pr}) P_r(k) < a_T(1 - a_{pr}) a'_2 P_h(k) + a_T(1 - a_{pr}) b'_2
$$

$$
a_T(1 - a_{pr}) P_r(k) < a_T b_{pr} P_h(k) + a_T(1 - a_{pr}) \underline{P}_r - b_T \delta_{P_h}
$$

or, $a_T((1 - a_{pr})(\underline{P}_r - P_r(k)) + b_{pr} P_h(k)) - b_T \delta_{P_h} > 0$ which implies that the lower bound (2.13) is positive, and hence $\Delta TSC(k) > 0$ is satisfied. ∎

Now, we present the proof of the Theorem 1 in the following.

Proof. To enable the switches from autonomous mode to manual mode at the time step k, the condition $TSC(k) \leq TSC_l$ must be satisfied. Based on Fig. 2.4, we need to have $\Delta TSC(k) < 0$ at this time step when the autonomous mode is activated ($M(k) = 0$). According to Lemma 1, this happens when $TSC_l > TSC_{lb}$ where TSC_{lb} is defined according to (2.9). Similarly, to enable the switches from manual mode to autonomous mode at the time step k, we need to have $\Delta TSC(k) > 0$ under $M(k) = 1$. According to Lemma 2, this can be guaranteed when $TSC_u < TSC_{ub}$ where TSC_{ub} is defined according to (2.10). Therefore, if $TSC_{lb} < TSC_l < TSC_u < TSC_{ub}$ holds, a regular switching between the manual and autonomous control modes is guaranteed. ∎

Remark 4 *Notice that the system parameters should allow $TSC_{ub} > TSC_{lb}$, otherwise, this method of switching is not possible. These bounds are static values calculated after identifying the system parameters. Different decision thresholds TSC_l and TSC_u that fall within these bounds (i.e. $TSC_{lb} < TSC_l < TSC_u < TSC_{ub}$) can be chosen to analyze the system dynamic behaviours.* •

Notice that if the system starts initially outside the region $TSC_l \leq TSC(k) \leq TSC_u$, under this condition and switching rule (2.8), it should eventually end up in this region. Further, unlike continuous-time systems, due to the discrete transitions of system dynamics (2.1), (2.3), (2.5), and (2.6), a current state $TSC(k)$ in the region $[TSC_l, TSC_u]$ might lead to a next state outside of the region. This is the so-called type-P trajectory of the state dynamics for a practical discrete-time system [39]. Thus, the actual switches may occur at values a bit higher (lower) than TSC_u (TSC_l). Based on *Assumption 3*(d), the system will eventually stay in

$$TSC_l - \delta_{TSC} \leq TSC(k) \leq TSC_u + \delta_{TSC}. \tag{2.14}$$

Also note that due to the change of human workload, the steady-state results of the HRI system will be oscillatory instead of converging to a certain fixed value.

2.3.2 Bounds on Robot Performance

Based on Equations (2.1), (2.14) and bounds on P_h inside the region $[TSC_l - \delta_{TSC}, TSC_u + \delta_{TSC}]$, the steady-state bounds on the robot performance can be obtained as follows

$$
\begin{aligned}
P_{rl} &\leq P_r(k) \leq P_{ru}, \\
P_{rl} &\triangleq \max\left(\frac{TSC_l - \delta_{TSC} + b_T \underline{P}_h}{a_T}, \underline{P}_r\right), \\
P_{ru} &\triangleq \min\left(\frac{TSC_u + \delta_{TSC} + b_T \overline{P}_h}{a_T}, \overline{P}_r\right).
\end{aligned}
\tag{2.15}
$$

Note that the initial robot performance, $P_r(0)$, can be outside of this bound. Next, we derive the maximum dwell time under *1)* an exclusively autonomous mode for the robot performance to decrease from the upper bound P_{ru} to the lower bound P_{rl}, and *2)* an exclusively manual mode for the robot performance to increase from P_{rl} to P_{ru}. The derived maximum dwell time will be used in Section 2.3.3 to calculate bounds on human utilization.

2.3.2.1 Maximum Dwell Time under the Autonomous Mode

Lemma 3 *Under the switching law (2.8), the maximum dwell time to stay in the region $[TSC_l - \delta_{TSC}, TSC_u + \delta_{TSC}]$ under the exclusively autonomous mode at steady-state is*

$$\tau_{da} = \left\lfloor \left| \frac{\ln\left(\frac{P_{rl} - \underline{P}_r}{P_{ru} - \underline{P}_r} \right)}{\ln(a_{pr})} \right| \right\rfloor, \tag{2.16}$$

where $\lfloor \cdot \rfloor$ is the floor function.

Proof. Denote τ_a as the dwell time in the region $[TSC_l - \delta_{TSC}, TSC_u + \delta_{TSC}]$ under the autonomous mode at steady state. Under the autonomous mode ($M(k) = 0$), using Equation (2.3), the robot performance at τ_a time steps from the current state $P_r(k)$ is calculated by

$$
\begin{aligned}
P_r(k+1) &= a_{pr} P_r(k) + (1 - a_{pr})\underline{P}_r, \\
P_r(k+2) &= a_{pr}^2 P_r(k) + a_{pr}(1 - a_{pr})\underline{P}_r + (1 - a_{pr})\underline{P}_r \\
&\vdots \\
P_r(k+\tau_a) &= a_{pr}^{\tau_a} P_r(k) + (1 - a_{pr})\underline{P}_r \sum_{i=0}^{\tau_a - 1} a_{pr}^i, \\
&= a_{pr}^{\tau_a}\left(P_r(k) - \underline{P}_r\right) + \underline{P}_r,
\end{aligned}
\tag{2.17}
$$

where $P_r(k+\tau_a)$ can decrease from $P_r(k)$ (at $\tau_a = 0$) to $\underline{P}_r$ (at $\tau_a = \infty$). To calculate the maximum dwell time under $M(k) = 0$, let $P_r(k) = P_{ru}$ initially. Based on (2.17), from P_{ru} to any arbitrary $P_r(k + \tau_a)$ in $[P_{rl}, P_{ru}]$, we have

$$P_{rl} \leq P_r(k+\tau_a) = a_{pr}^{\tau_a}\left(P_{ru} - \underline{P}_r\right) + \underline{P}_r. \tag{2.18}$$

Since $0 < a_{pr} < 1$, we can rewrite (2.18) as

$$\tau_a \leq \frac{\ln\left(\frac{P_{rl} - \underline{P}_r}{P_{ru} - \underline{P}_r} \right)}{\ln(a_{pr})}. \tag{2.19}$$

Because the dwell time in the discrete-time setting should be an integer, the maximum dwell time that satisfies (2.19) is τ_{da} given by (2.16). Note that when $P_{rl} = \underline{P}_r$, (2.16) gives $\tau_{da} = \infty$. ∎

Remark 5 *The results of Equation (2.16) are graphically depicted in Fig. 2.5. In this figure, P_r*

is plotted as a function of the dwell time in the autonomous mode τ_a with initial value of P_{ru}. As it can be seen in this figure, smaller values of P_{rl}, correspond to the larger values of the dwell time τ_{da} (with $\tau_{da} = \infty$ when $P_{rl} = \underline{P}_r$). This is compatible with the solution to the first order difference equation presented in Equation (2.17). •
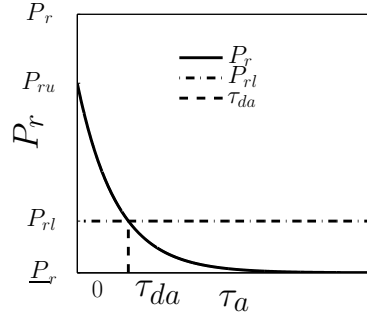
Figure 2.5: Maximum dwell time in the autonomous mode τ_{da} under the switching law (2.8).

2.3.2.2 Maximum Dwell Time under the Manual Mode

Lemma 4 *Under the switching law (2.8), the maximum dwell time to stay in the region $[TSC_l - \delta_{TSC}, TSC_u + \delta_{TSC}]$ under the exclusively manual mode at steady-state, denoted as τ_{dm}, is bounded by $\tau_{dml} \leq \tau_{dm} \leq \tau_{dmu}$ where*

$$\tau_{dml} = \left\lceil \frac{\ln\left(\frac{\underline{P}_r + c_{\overline{P}_h} - P_{ru}}{\underline{P}_r + c_{\overline{P}_h} - P_{rl}}\right)}{\ln(a_{pr})} \right\rceil , \quad c_{\overline{P}_h} \triangleq \overline{P}_r - \underline{P}_r, \tag{2.20}$$

$$\tau_{dmu} = \left\lceil \frac{\ln\left(\frac{\underline{P}_r + c_{\underline{P}_h} - P_{ru}}{\underline{P}_r + c_{\underline{P}_h} - P_{rl}}\right)}{\ln(a_{pr})} \right\rceil , \quad c_{\underline{P}_h} \triangleq \frac{\underline{P}_h(\overline{P}_r - \underline{P}_r)}{\overline{P}_h}, \tag{2.21}$$

Proof. Denote τ_m as the dwell time in the region $[TSC_l - \delta_{TSC}, TSC_u + \delta_{TSC}]$ under the manual mode at steady state. Under the manual mode ($M(k) = 1$), using Equation (2.3), the robot

27

performance at τ_m time steps from the current time instant k is calculated by

$$P_r(k+1) = a_{pr}P_r(k) + (1 - a_{pr})\underline{P}_r + b_{pr}P_h(k),$$

$$P_r(k+2) = a_{pr}^2 P_r(k) + a_{pr}((1 - a_{pr})\underline{P}_r + b_{pr}P_h(k))$$

$$+ (1 - a_{pr})\underline{P}_r + b_{pr}P_h(k+1)$$

$$\vdots$$

$$P_r(k+\tau_m) = a_{pr}^{\tau_m}P_r(k) + (1 - a_{pr})\underline{P}_r \sum_{i=0}^{\tau_m-1} a_{pr}^i$$

$$+ b_{pr} \sum_{i=0}^{\tau_m-1} a_{pr}^{\tau_m-1-i}P_h(k+i). \tag{2.22}$$

Since $P_h(k)$ is a nonlinear function of human utilization $r(k)$, it might not be possible to find an explicit expression for τ_m based on a simplified form of (2.22). Instead, we estimate bounds for (2.22) knowing that $\underline{P}_h \leq P_h(k) \leq \overline{P}_h$ when $TSC(k)$ is in the region $[TSC_l - \delta_{TSC}, TSC_u + \delta_{TSC}]$. Consider the extreme cases $P_h(k) \equiv \underline{P}_h$ and $P_h(k) \equiv \overline{P}_h$ in (2.22), we estimate respectively, the bounds τ_{dmu}, τ_{dml} on maximum dwell time under the manual mode such that $P_r(k)$ increases from P_{rl} to $P_r(k+\tau_m)$ in τ_m time steps.

We first consider $P_h(k) \equiv \overline{P}_h$. Because $\sum_{i=0}^{\tau_m-1} a_{pr}^{\tau_m-1-i} = \sum_{i=0}^{\tau_m-1} a_{pr}^i$ and $b_{pr}\overline{P}_h = (1 - a_{pr})c_{\overline{P}_h}$ where $c_{\overline{P}_h}$ is defined in Equation (2.20), Equation (2.22) becomes

$$\begin{aligned}
P_r(k+\tau_m) &= (1 - a_{pr})\left(\underline{P}_r + c_{\overline{P}_h}\right) \sum_{i=0}^{\tau_m-1} a_{pr}^i + a_{pr}^{\tau_m}P_r(k) \\
&= a_{pr}^{\tau_m}\left(P_r(k) - \underline{P}_r - c_{\overline{P}_h}\right) + \underline{P}_r + c_{\overline{P}_h}, \tag{2.23}
\end{aligned}$$

where $P_r(k+\tau_m)$ can increase from $P_r(k)$ (at $\tau_m = 0$) to $\underline{P}_r + c_{\overline{P}_h} = \overline{P}_r$ (at $\tau_m = \infty$). To calculate the maximum dwell time under $M(k) = 1$, let $P_r(k) = P_{rl}$ initially. We next calculate the lower bound τ_{dml} on the maximum dwell time τ_{dm} for $P_r(k)$ to increase from P_{rl} to P_{ru}. Based on (2.23), from P_{rl} to any arbitrary $P_r(k+\tau_m)$ in $[P_{rl}, P_{ru}]$ under $M(k) = 1$ and with $P_h(k) \equiv \overline{P}_h$, it must follow that

$$P_{ru} \geq a_{pr}^{\tau_m}\left(P_{rl} - \underline{P}_r - c_{\overline{P}_h}\right) + \underline{P}_r + c_{\overline{P}_h}. \tag{2.24}$$

28

Since $0 < a_{pr} < 1$, we can rewrite (2.24) as

$$\tau_m \leq \frac{\ln\left(\frac{\underline{P}_r + c_{\overline{P}_h} - P_{ru}}{\underline{P}_r + c_{\overline{P}_h} - P_{rl}}\right)}{\ln(a_{pr})}. \tag{2.25}$$

Since the dwell time τ_m is an integer, the maximum dwell time that satisfies (2.25) is τ_{dml} given by Equation (2.20). Note that (2.20) gives $\tau_{dml} = \infty$ for the case $P_{ru} = \overline{P}_r$.

Similarly for $P_h(k) \equiv \underline{P}_h$, Equation (2.22) becomes

$$P_r(k + \tau_m) = a_{pr}^{\tau_m}\left(P_r(k) - \underline{P}_r - c_{\underline{P}_h}\right) + \underline{P}_r + c_{\underline{P}_h}, \tag{2.26}$$

which gives

$$P_{ru} \geq a_{pr}^{\tau_m}\left(P_{rl} - \underline{P}_r - c_{\underline{P}_h}\right) + \underline{P}_r + c_{\underline{P}_h}.$$

and results in the upper bound τ_{dmu} (2.21) on the maximum dwell time τ_{dm} for $P_r(k)$ to increase from P_{rl} to P_{ru}. Notice that for $P_h(k) \equiv \underline{P}_h$, using similar derivations, $P_r(k)$ can increase from P_{rl} to $\underline{P}_r + c_{\underline{P}_h}$ (at $\tau_{dmu} = \infty$ with $c_{\underline{P}_h}$ defined in (2.21)). Therefore, this bound calculation holds for $P_{ru} \leq \underline{P}_r + c_{\underline{P}_h}$ since $\underline{P}_r + c_{\underline{P}_h}$ is the maximum achievable P_r under the $\underline{P}_h$. ∎

Remark 6 *The results of Equations (2.20) and (2.21) are graphically depicted in Fig. 2.6. In this figure, P_r are plotted as a function of the dwell time in the manual mode τ_m with initial value P_{rl}. The plots represent the solutions to the first order difference equations (2.23) and (2.26), which can increase from P_{rl} to $\overline{P}_r$ and $\underline{P}_r + c_{\underline{P}_h}$, respectively. It can be observed that larger values of P_{ru} correspond to larger values of the dwell time τ_{dml} and τ_{dmu}. This can be verified via Equations (2.20) and (2.21).* •

Proposition 1 *The relationship $\tau_{dml} < \tau_{dmu}$ indicates that the maximum dwell time in the manual mode under $\overline{P}_h$ is smaller than that under $\underline{P}_h$.*

Proof. *For the sake of brevity, we first define two constants P_{ri} and P_{ra} as follows*

$$P_{ri} \triangleq \underline{P}_r + c_{\underline{P}_h}, \quad P_{ra} \triangleq \underline{P}_r + c_{\overline{P}_h}, \tag{2.27}$$

where $c_{\overline{P}_h}$ and $c_{\underline{P}_h}$ are defined in (2.20) and (2.21) respectively. From the definitions in (2.27), it

29

is easy to show that $P_{ra} > P_{ri}$ because $\frac{\underline{P}_h(\overline{P}_r - \underline{P}_r)}{\overline{P}_h} < \overline{P}_r - \underline{P}_r$ and hence $c_{\underline{P}_h} < c_{\overline{P}_h}$. It follows that

$$
\begin{aligned}
P_{ra}(P_{ru} - P_{rl}) &> P_{ri}(P_{ru} - P_{rl}), \\
-P_{ra}P_{rl} - P_{ru}P_{ri} &> -P_{ru}P_{ra} - P_{ri}P_{rl}, \\
P_{ra}P_{ri} - P_{ra}P_{rl} - P_{ru}P_{ri} + P_{ru}P_{rl} &> P_{ri}P_{ra} - P_{ri}P_{rl} - P_{ru}P_{ra} + P_{ru}P_{rl}, \\
(P_{ra} - P_{ru})(P_{ri} - P_{rl}) &> (P_{ri} - P_{ru})(P_{ra} - P_{rl}), \quad (2.28)
\end{aligned}
$$

where P_{rl} and P_{ru} are defined in (2.15). We have $P_{ra} - P_{rl} > 0$ because $P_{ra} = \underline{P}_r + c_{\overline{P}_h} = \underline{P}_r + \overline{P}_r - \underline{P}_r = \overline{P}_r$. We also have $P_{ri} - P_{rl} > 0$ because according to the explanations about (2.21), $P_{rl} < P_{ru} \leq \underline{P}_r + c_{\underline{P}_h} = P_{ri}$. Therefore, the inequality (2.28) becomes

$$
\begin{aligned}
\frac{P_{ra} - P_{ru}}{P_{ra} - P_{rl}} &> \frac{P_{ri} - P_{ru}}{P_{ri} - P_{rl}}, \\
\ln\left(\frac{P_{ra} - P_{ru}}{P_{ra} - P_{rl}}\right) &> \ln\left(\frac{P_{ri} - P_{ru}}{P_{ri} - P_{rl}}\right). \quad (2.29)
\end{aligned}
$$

Since $\ln(a_{pr}) < 0$, (2.29) becomes

$$
\begin{aligned}
\frac{\ln\left(\frac{P_{ra} - P_{ru}}{P_{ra} - P_{rl}}\right)}{\ln(a_{pr})} &< \frac{\ln\left(\frac{P_{ri} - P_{ru}}{P_{ri} - P_{rl}}\right)}{\ln(a_{pr})}, \\
\frac{\ln\left(\frac{\underline{P}_r + c_{\overline{P}_h} - P_{ru}}{\underline{P}_r + c_{\overline{P}_h} - P_{rl}}\right)}{\ln(a_{pr})} &< \frac{\ln\left(\frac{\underline{P}_r + c_{P_c \min} - P_{ru}}{\underline{P}_r + c_{\underline{P}_h} - P_{rl}}\right)}{\ln(a_{pr})}, \\
\tau_{dml} &< \tau_{dmu}.
\end{aligned}
$$

$\blacksquare$

This result is compatible with intuition since when the operator has a higher performance in controlling the robot, he (she) can increase the robot performance in a shorter amount of time. $\bullet$

2.3.3 Human Utilization Bounds

It is difficult to obtain the actual bounds on human utilization by finding an exact solution to the nonlinear system dynamics (2.5) and (2.6) under the switching law (2.8). Instead, we estimate the bounds based on periodic switches determined by the bounds of maximum dwell time τ_{da}, τ_{dml} and τ_{dmu} given by Equations (2.16), (2.20), and (2.21) (as shown in Fig. 2.7). Because we use the
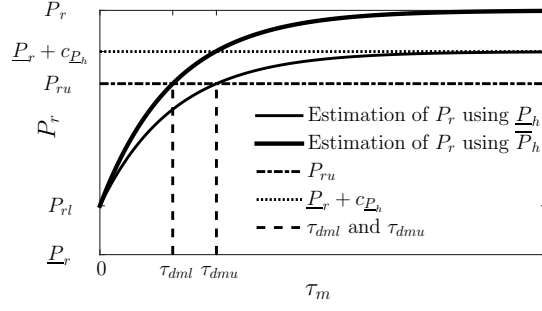
Figure 2.6: Bounds τ_{dml} and τ_{dmu} of the maximum dwell time in the manual mode under the switching law (2.8).

bounds on maximum dwell time in the periodic solution, the actual bounds on $r(k)$ at the steady-state should be bounded between the bounds on periodic switches (see the illustration of r_l and r_u in Fig. 2.7).
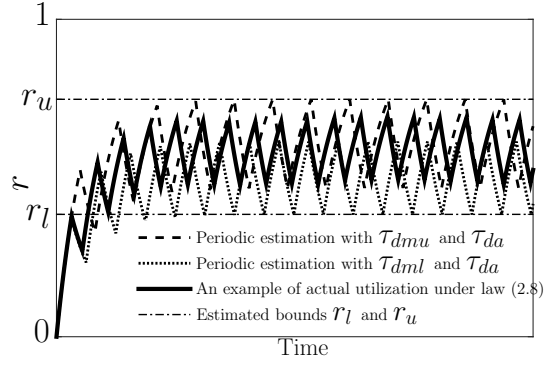
Figure 2.7: Human utilization bound estimation.

Lemma 5 *The human utilization level after n time steps (from the current time step k) under the manual mode is obtained by*

$$r(k+n) = a_r^n r(k) + 1 - a_r^n = (r(k) - 1)a_r^n + 1, \tag{2.30}$$

and under the autonomous mode is obtained by

$$r(k+1) = a_r r(k) \Rightarrow \cdots \Rightarrow r(k+n) = a_r^n r(k). \tag{2.31}$$

31

Proof. We show how to calculate the human utilization level after n time steps (from the current time step k) under the manual and autonomous mode, respectively.

Under the manual mode $(M(k) = 1)$, using (2.5), we obtain

$$r(k + n) = a_r^n r(k) + b_r \sum_{i=0}^{n-1} a_r^i. \tag{2.32}$$

The term $b_r \sum_{i=0}^{n-1} a_r^i$, in (2.32) is a geometric series and is equivalent to $b_r \sum_{i=0}^{n-1} a_r^i = b_r \frac{1-a_r^n}{1-a_r}$ and we also know from (2.5) that $b_r = 1 - a_r$. Therefore, we can rewrite (2.32) as

$$r(k + n) = a_r^n r(k) + 1 - a_r^n = (r(k) - 1)a_r^n + 1,$$

which is Equation (2.30). Under the autonomous mode $(M(k) = 0)$, using (2.5), we obtain

$$r(k + 1) = a_r r(k) \Rightarrow \cdots \Rightarrow r(k + n) = a_r^n r(k),$$

which is Equation (2.31). ∎

Theorem 2 *Under the switching law (2.8), the human utilization $r(k)$ is bounded in $[r_l, r_u]$ where*

$$r_l = \frac{(1 - a_r^{\tau_{dml}})a_r^{\tau_{da}}}{1 - a_r^{\tau_{dml}+\tau_{da}}}, \quad r_u = \frac{1 - a_r^{\tau_{dmu}}}{1 - a_r^{\tau_{dmu}+\tau_{da}}}, \tag{2.33}$$

with τ_{da}, τ_{dml} and τ_{dmu} given by Equations (2.16), (2.20), and (2.21) in Lemmas 3 and 4.

Proof. Consider the case when the system is periodically switching between the manual and autonomous mode with τ_m dwell time under the manual mode and τ_a dwell time under the autonomous mode.

We first consider the case when the system is initially in the manual mode with a utilization level $r(k)$. Under $M(k) = 1$, based on Equation (2.30) in Lemma 5, the human utilization level after τ_m time steps from the current time step k is

$$r(k + \tau_m) = (r(k) - 1)a_r^{\tau_m} + 1. \tag{2.34}$$

Then, when the system switches to the autonomous mode and stays in this mode for τ_a, using Equation (2.31) in Lemma 5 and Equation (2.34), we obtain the utilization level after τ_a as

$$r(k + \tau_m + \tau_a) \quad = \quad (r(k) - 1)a_r^{\tau_m + \tau_a} + a_r^{\tau_a}. \tag{2.35}$$

Then let the system switch back to the manual mode again and keep this mode for another τ_m, we can obtain

$$r(k + 2\tau_m + \tau_a) = (r(k) - 1)a_r^{2\tau_m + \tau_a} + a_r^{\tau_m + \tau_a} - a_r^{\tau_m} + 1.$$

Another τ_a steps under the autonomous mode result in

$$r(k + 2\tau_m + 2\tau_a) = (r(k) - 1)a_r^{2\tau_m + 2\tau_a} + a_r^{\tau_m + 2\tau_a} - a_r^{\tau_m + \tau_a} + a_r^{\tau_a}.$$

Following this pattern for n periods in the manual mode and then n periods in the autonomous mode yields:

$$\begin{aligned}
r(k &+ n(\tau_m + \tau_a)) \\
&= r(k)a_r^{n(\tau_m + \tau_a)} - a_r^{n(\tau_m + \tau_a)} + a_r^{(n-1)\tau_m + n\tau_a} \\
&\quad + \ldots - a_r^{2\tau_m + 2\tau_a} + a_r^{\tau_m + 2\tau_a} - a_r^{\tau_m + \tau_a} + a_r^{\tau_a} \\
&= r(k)a_r^{n(\tau_m + \tau_a)} + a_r^{(n-1)(\tau_m + \tau_a)}(1 - a_r^{\tau_m})a_r^{\tau_a} \\
&\quad + \ldots + a_r^{\tau_m + \tau_a}(1 - a_r^{\tau_m})a_r^{\tau_a} + (1 - a_r^{\tau_m})a_r^{\tau_a} \\
&= r(k)a_r^{n(\tau_m + \tau_a)} + (1 - a_r^{\tau_m})a_r^{\tau_a} \sum_{i=0}^{n-1} a_r^{(\tau_m + \tau_a)i}. \tag{2.36}
\end{aligned}$$

When $n \to \infty$ in the steady-state, since $0 < a_r < 1$, the first term in (2.36) goes to zero. The second term forms a geometric series and gives a lower bound on utilization

$$\underline{r} \triangleq (1 - a_r^{\tau_m})a_r^{\tau_a} \frac{1}{1 - a_r^{\tau_m + \tau_a}}. \tag{2.37}$$

So far, we have obtained the lower bound on human utilization, denoted as $\underline{r}$, when the system starts from manual mode and has equal periods of manual and autonomous control modes. The

other possibility is to continue with one more period of manual mode of τ_m, based on Equation (2.36), we obtain

$$r(k + (n + 1)\tau_m + n\tau_a) = r(k)a_r^{\tau_m} a_r^{n(\tau_m + \tau_a)} + (1 - a_r^{\tau_m}) \sum_{i=0}^{n} a_r^{(\tau_m + \tau_a)i}.$$

When $n \to \infty$, we obtain an upper bound on utilization, i.e.

$$\overline{r} \triangleq (1 - a_r^{\tau_m}) \frac{1}{1 - a_r^{\tau_m + \tau_a}}, \tag{2.38}$$

where $\overline{r}$ is the upper bound on human utilization level when we have one more period of manual mode of τ_m. Since $0 < a_r < 1$, $\tau_m > 0$ and $\tau_a > 0$, the bound $\overline{r}$ in (2.38) is larger than the bound $\underline{r}$ in (2.37). Therefore, assuming that the system is initially in the manual mode, (2.37) and (2.38) give the lower and upper bounds for human utilization level in the steady-state, respectively. Similarly, we can obtain the same bounds for the case when the system is initially in the autonomous mode. The proofs are relatively straightforward and hence omitted here. These results indicate that, regardless of the initial utilization level $r(k)$ and control mode, the periodic switches result in specific lower and upper bounds for the human utilization level as functions of τ_m and τ_a under steady-state.

Combining the maximum dwell time expressions τ_{da}, τ_{dml} and τ_{dmu}, we can find two periodic solutions and accordingly four bounds on human utilization (see Fig. 2.7). We take the minimum (maximum) estimated utilization as the lower (upper) bound of the human utilization under the switching condition (2.8). According to the explanations about Equations (2.37) and (2.38) and reminding that $\tau_{dmu} > \tau_{dml}$, when we substitute τ_{dml} and τ_{da} in (2.37), we obtain the minimum estimation for the lower bound of $r(k)$ which is equal to r_l in (2.33). Similarly, when we substitute τ_{dmu} and τ_{da} in (2.38), we obtain the maximum estimation for the upper bound of $r(k)$ which is equal to r_u in (2.33). ∎

2.4   Case Studies

In the following, we provide two case studies. The first case study focuses on giving examples on how the theoretical contributions of this chapter apply to the (semi)autonomous robotic problems and provides different steps of such problems from a control theory perspective. This study involves a small number of human subject and paves the way for further different studies. Then, a second case

study on the applications in the teleoperation of Unmanned Aerial Vehicles (UAVs) is provided which focuses on broadening the robotics applications considered in this chapter and more importantly a through statistical analysis of such application via a larger group of human test subjects.

2.4.1 Case Study I: Ground Robot Teleoperation

Utilizing the testbed introduced in Section 2.2, we conducted several experiments with human-in-the-loop. The project institutional review board (IRB) has been approved for these experiments. The experiments include two sessions. During the first session, a brief tutorial about the experiment was given and an identification process was performed to identify the model parameters for each participant (Section 2.4.1.1) as well as their control allocations scheme. In the second session, all of the subjects participated in 5 different tests, as detailed in Section 2.4.1.2, based on a random test order for each participant. Section 2.4.1.3 presents the results of the experiments via several objective and subjective measures. The objectives of this case study include i) examining the consistency of the TSC-based switching method with human autonomy allocation pattern, ii) validating the robot performance and human utilization bounds (2.15) and (2.33) when the switching rule (2.8) is followed, and iii) comparing the results of different test conditions via subjective and objective measures.

2.4.1.1 Parameter Identification

Before utilizing the proposed switching control (2.8), we need to identify the parameters of the human and robot performance dynamics (2.3), (2.5) and (2.6) for each participant. 5 male Clemson University graduate students between the ages of 22 and 33 participated in the study. We selected participants with video gaming experience in order to expedite the training process (*Assumption 2*) and guarantee that they can consistently control the robot throughout different experiments. Using an identification process similar to method explained in Section 2.2, the results in Table 2.1 are obtained. In this table, TSC_{lb} and TSC_{ub} are also calculated for each participant via Equations (2.9) and (2.10), respectively.

2.4.1.2 Independent and Dependent Variables

The independent variable (IV) is the switching control scheme which includes five levels (test conditions). There are 7 dependent variables (DV) including: robot performance, human

35

	Participants				
	1	2	3	4	5
a_r	0.999	0.9995	0.9995	0.9995	0.9994
b_r	0.001	0.0005	0.0005	0.0005	0.0006
$\underline{P_h}$	0.425	0.365	0.39	0.38	0.37
$\overline{P_h}$	0.465	0.407	0.43	0.434	0.409
β	0.95	0.81	0.8	0.75	0.71
a_{pr}	0.998	0.9953	0.997	0.9958	0.9964
b_{pr}	0.0007	0.0013	0.0008	0.0012	0.0011
$\underline{P_r}$	0.24	0.24	0.24	0.24	0.24
$\overline{P_r}$	0.4	0.35	0.35	0.362	0.362
δ_{P_h}	5.44E-5	6.28E-5	6.3E-5	1.0E-4	1.01E-4
δ_{P_r}	1.71E-4	3.82E-4	2.9E-4	4.05E-4	3.45E-4
δ_{TSC}	0.0022	0.0047	0.0048	0.0041	0.0035
TSC_{lb}	-0.465	-0.404	-0.369	-0.289	-0.319
TSC_{ub}	0.686	0.441	0.436	0.314	0.507

Table 2.1: The parameters of dynamic models (2.3), (2.5) and (2.6) identified for the 5 participants in the study.

utilization, human performance, perceived workload, satisfaction, trust, and the percentage of the followed automated control allocation suggestions which are detailed in Section 2.4.1.3.iii. The IV levels are detailed as follows.

Manual Control Allocation In this case, the operator is free to choose when to control the robot through the joystick and when to switch to the autonomous mode. The operator uses the performance GUI (shown in Fig. 2.1) to decide how to allocate the control modes. We denote this condition as **C1**.

Automated Decision Aids using the TSC model The operator receives suggestions about control mode allocation calculated based on the TSC-based scheme (2.8). In condition 2 (**C2**), the participant is allowed not to follow the suggested modes, while in condition 3 (**C3**), the participant must follow them. Before applying the TSC-based control scheme, two decision thresholds TSC_l and TSC_u need to be chosen for each participant based on the parameters identified in Table 2.1. The process is shown in Algorithm 1. The desired decision thresholds are chosen such that r_l and r_u enclose the optimal level β and P_{ru} is close to the $\overline{P_r}$[2]. The results are shown in Table 2.2. Notice that the chosen decision threshold satisfy $TSC_{lb} < TSC_l < TSC_u < TSC_{ub}$ for each participant.

---

[2]The robot performance maximization scheme is separately considered in the test conditions **C4**-**C5** in Section 2.4.1.2.

Parameters	Participants				
	1	**2**	**3**	**4**	**5**
TSC_l	0.15	0.0	0.0	0.05	0.05
TSC_u	0.62	0.35	0.27	0.25	0.45
P_{rl}	0.32	0.28	0.287	0.285	0.289
P_{ru}	0.39	0.336	0.335	0.342	0.351
r_l	0.63	0.613	0.634	0.587	0.649
r_u	1.0	0.815	0.82	0.786	1.0

Table 2.2: Decision thresholds chosen for tests **C2**-**C3** and the resulting robot performance and human utilization bounds.

Once the decision thresholds are chosen, the TSC-based control allocation aid is implemented. The control panel in Fig. 2.1 shows an example of the moment when the TSC-based algorithm suggests the operator to switch to the manual control mode by showing a blinking "Suggested Control Mode" (M in the green box).

Algorithm 1 Parameter Identification and Decision Threshold Selection

---
1: Parameter identification for Eqns. (2.1), (2.3), (2.5) and (2.6)
2: **procedure** CHOOSING TSC_l AND TSC_u
3:    **while** desired r and P_r bounds are not obtained **do**
4:        Choose TSC_l and TSC_u (Theorem 1)
5:        Check if the steady-state bounds on r and P_r are desirable (Equations (2.15) and (2.33))
6:    **end while**
7: **end procedure**

Automated Decision Aids for Robot Performance Maximization   The operator receives suggestions about control mode allocation via the P_r maximization control allocation scheme presented in Algorithm 2. In condition 4 (**C4**), the participant is allowed not to follow the suggested mode. In condition 5 (**C5**), the participant must follow the suggestions. Using this method, $P_r(k)$ remains in a region close to the maximum value while the operator also gets some break from the manual mode when $P_r(k)$ reaches the maximum value.

2.4.1.3   Results

In the following results, participants were asked to complete 8 laps in the trajectory tracking example in each test condition.

i) Consistency of TSC-Based Control Allocation with Human Pattern   We track the human control allocation behavior under **C1** for each participant based on the individual specific

Algorithm 2 Implementation of the robot performance maximization switching scheme

---
 1: **while** Experiment is running **do**
 2:     Measure the real-time value of $P_r(k)$ value
 3:     **if** $P_r(k) = \overline{P}_r$ **then**
 4:         Suggest the autonomous control mode
 5:     **else if** $P_r(k) \leq \underline{P}_r + 0.9(\overline{P}_r - \underline{P}_r)$ **then**
 6:         Suggest the manual control mode
 7:     **else**
 8:         Do not suggest any control mode changes
 9:     **end if**
10: **end while**

Decision Thresholds		Participants				
		1	**2**	**3**	**4**	**5**
TSC_l	μ	-0.24	-0.199	0.096	-0.02	0.08
	σ	0.06	0.06	0.13	0.04	0.21
TSC_u	μ	0.61	0.50	0.51	0.43	0.59
	σ	0.07	0.05	0.29	0.11	0.13

Table 2.3: Decision threshold captured via the TSC model in a manual control allocation scheme (condition **C1**).

parameters in Table 2.1. Two sets (totally 16 laps) of tests were conducted by each participant and the results are shown in Table 2.3 in the form of average values of TSC_l and TSC_u. Considering the average values of TSC_l and TSC_u and the corresponding standard deviations, it can be seen that participants 1, 2, 4 and 5 on average follow a TSC-based switching pattern similar to rule (2.8). Participant 3 sometimes switched to the manual mode when TSC is higher while some other times to the autonomous mode when TSC is relatively lower. This makes the thresholds TSC_u and TSC_l not clearly distinguishable and hence not consistent with the switching rule (2.8). This might be related to the stochastic uncertainty in manual decision-making which is reflected in the higher standard deviations for this participant. For the entire set of participants, 84.5% switches occur within $TSC_u \pm 0.15$ and $TSC_l \pm 0.15$ of the values in Table 2.3. For better illustration, the switching scheme and the corresponding TSC level for participant 2 are shown in Fig. 2.8 as an example.

ii) Robot Performance and Human Utilization Bounds under TSC-Based Control Allocation We now examine the accuracy of the estimated bounds for condition **C3**. As an example, the experimental data for robot and human performances, human utilization as well as TSC level for participant 1 are shown in Fig. 2.9. As seen in this figure, the theoretical results for the bounds r_l, r_u, P_{rl} and P_{ru} obtained by (2.33) and (2.15) (see the first column of Table 2.2), match the
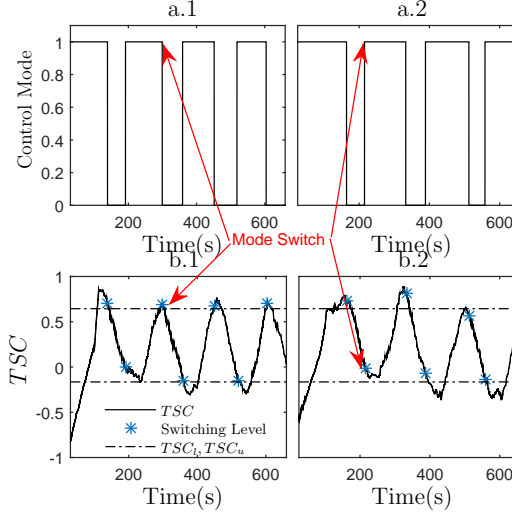
Figure 2.8: Tracking of autonomy allocation pattern of participant 2 using the TSC model in two tests: a) the control mode $M(k)$, and b) the corresponding TSC level.

experimental data to a great extent. Some small differences are due to the conservative estimation of these bounds as well as a small lag in human response to the suggestions.
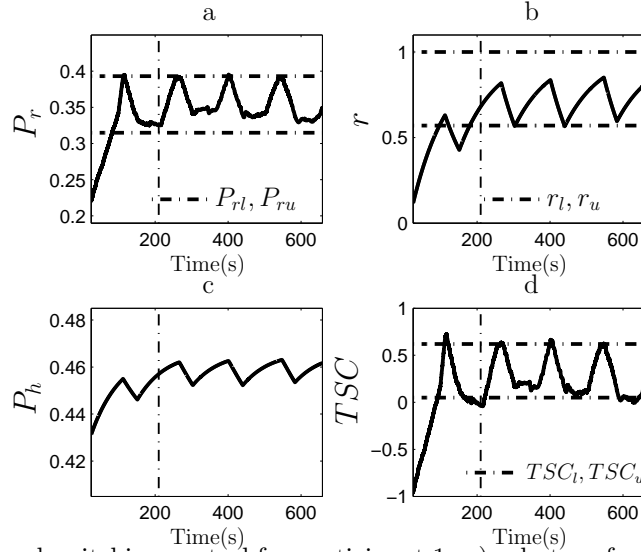
Figure 2.9: TSC-based switching control for participant 1: a) robot performance, b) human utilization level, c) human performance, and d) TSC. Vertical doted-dashed lines represent a time index for the beginning of the system steady-state.

iii) Comparison via Subjective and Objective Measures For subjective measures, we evaluated perceived workload, satisfaction, and trust after each test. The results are shown in Table 2.4.

Control	TLX		Sat		Trust	
Scheme	μ	σ	μ	σ	μ	σ
C1	42.44	16.28	3.85	0.75	5.71	0.84
C2	38.83	19.64	3.9	0.79	5.95	0.74
C3	37.6	19.41	4.05	0.99	5.88	1.25
C4	49.06	12.01	3.7	0.92	5.22	1.35
C5	41.6	15.02	3.65	0.98	5.28	1.39

Table 2.4: Comparison of the control switching schemes over the entire set of participants via subjective measures of task load index (TLX), satisfaction (Sat), and Trust.

NASA TLX [103] was used to measure the perceived workload. We evaluated the satisfaction of participants with a post-test questionnaire in which, participant's satisfaction, comfort as well as feeling of being in control of the task were assessed via a 1-5 Likert scale. We also use the well-acknowledged trust questionnaire proposed in [50] to measure participants' trust in the semi(autonomous) control scheme. The results in Table 2.4 indicate higher trust and satisfaction as well as lower workload of operators in the TSC-based schemes (**C2** and **C3**) compared to the manual and robot performance maximization schemes.

We utilize objective measures of P_r, P_h and r in Equations (2.3), (2.5) and (2.6) to compare test conditions **C1-C5**. The results are presented in Table 2.5.

Remark 7 *Notice that the robot performance shown in this table varies within the range $P_r \in [0.24, 0.4]$. Although this seems to be very small difference, based on the measurements in this experiment, the minimum robot performance $\underline{P}_r = 0.24$ corresponds to an average tracking error of 0.704 m and velocity of 0.39 m/s; while the maximum robot performance $\overline{P}_r = 0.4$ corresponds to an average tracking error of 0.38 m and velocity of 0.49 m/s. We use the following equation to compare P_r in Table 2.5 under conditions* **C1-C5**:

$$P_{r\%}(Ci) = \frac{mean(P_r(Ci)) - \underline{P}_r}{\overline{P}_r - \underline{P}_r} \times 100\%, \quad i \in \{1, ..., 5\}. \tag{2.39}$$

•

Thus, using (2.39), we calculate that the TSC-based schemes (**C2-C3**) can improve robot performance (8.75% increase under **C2** and 6.9% under **C3**) compared to manual control allocation scheme **C1**. Meanwhile, even lower average human utilization level was achieved (1.5% reduction under **C2** and 2.8% under **C3**). This is probably because of better decision thresholds chosen in the TSC-based scheme. The robot performance under the performance maximization schemes are

Control	P_r		P_h		r	
Scheme	μ	σ	μ	σ	μ	σ
C1	0.318	0.026	0.418	0.026	0.651	0.1
C2	0.332	0.021	0.426	0.018	0.636	0.115
C3	0.329	0.02	0.426	0.019	0.623	0.129
C4	0.343	0.022	0.43	0.019	0.739	0.104
C5	0.348	0.020	0.429	0.02	0.758	0.109

Table 2.5: Comparison of the control switching schemes over the entire set of participants using objective measures.

Conditions	Participants					Overall	
	1	2	3	4	5	μ	σ
C2	100	100	50	100	42.86	78.57	29.45
C4	85.71	40	68.75	100	25	63.89	31.17

Table 2.6: Percentage of the followed suggestions.

higher than that under the TSC-based scheme (11.86% for **C5** compared to **C3**), however, at the cost of higher human utilization (13.5% increase for **C5** compared to **C3**).

We also tracked the percentage of time that the participants followed suggestions of the automated decision aid during the test conditions **C2** and **C4**. Whenever a suggestion was shown to the operator, if the operator followed the suggestion before a 15 seconds deadline, we considered this as an accepted and hence followed suggestion. The results are shown in Table 2.6. It can be seen that on average, the participants followed the TSC-based suggestion with a 14.68% more acceptance likelihood than the robot performance maximization scheme. The above results show the advantages of the proposed TSC-based scheme since: i) it improves the overall robot performance, human performance, and reduces human utilization and the perceived workload compared to the manual control allocation, and ii) it is human-like and entails more acceptance, satisfaction, and trust by human operators compared to the performance maximization and manual allocation schemes.

2.4.2 Case Study II: UAV teleoperation

For a thorough statistical analysis as well as extending the proposed scheme to robotic applications with unstructured environments, we designed a new testbed as shown in Figure 2.10. This testbed follows the same principals for the control switching scheme as the testbed in Figure 2.1. However, in this experiment the operators control an Unmanned Aerial Vehicle (UAV) to follow a ground robot as precisely as possible. The robot performance is defined as the average tracking
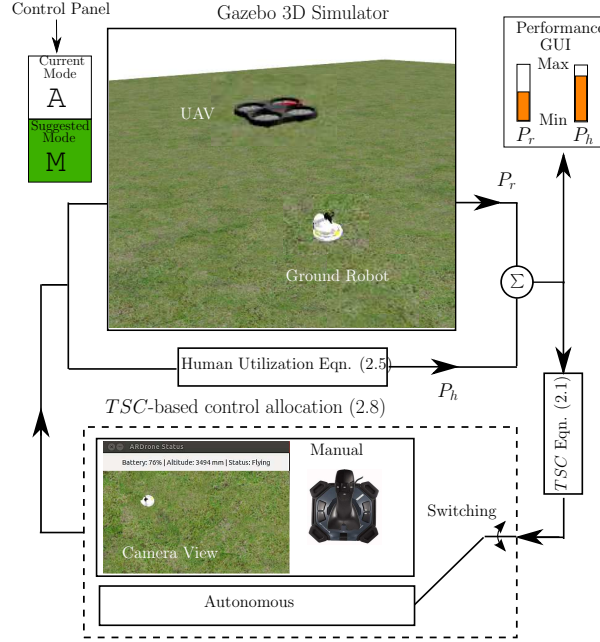
Figure 2.10: UAV teleoperation testbed.

accuracy in a past time window according to $Z_{P_r}(k) = \frac{1}{W} \sum_{j=k-W}^{k} \frac{e_{\max}-e(j)}{e_{\max}}$. The human perfor-
mance is defined as the quality of the operator commands $\mathbf{u}_h$ on the joystick compared to an ideal
control command $\mathbf{u}_i$ that has the perfect information about the motion of ground robot and tracking
error. The human inputs $\mathbf{u}_h$ are obtained from the joystick readings, while the ideal control inputs
$\mathbf{u}_i$ can be calculated from the exact positions and velocities of the UAV and ground robot available
in the simulator. The human performance is measured by $Z_{P_h}(k) = \frac{1}{W} \sum_{j=k-W}^{k} \frac{u_i(j)-u_h(j)}{du_{\max}}$ where
$du_{\max} > 0$ is a normalization constant. In this setting, the autonomous controller cannot detect the
location of the ground robot as precisely as human can do. Therefore, the tracking accuracy grad-
ually decreases under autonomous mode compared to the manual mode. Based on the preliminary
results obtained in the Section 2.4.1.3, we hypothesize that a human-like TSC-based automated
decision aid system,

a) Can improve the overall task performance compared to the manual mode via using objective
   measures and a more efficient autonomy allocation,

b) Can reduce operator's workload in decision-making

c) Will be accepted and trusted by human operator compared to the task performance optimization
   scheme since it includes human's decision-making pattern as well as objective measures

42

In the following, we provide the details of different components of this experiment.

2.4.2.1 Independent and Dependant Variables

Similar to the previous experiment, only one independent variable (IV) is considered here, i.e., the control allocation scheme including five levels as explained in conditions **C1**-**C5** in Section 2.4.1.2. We utilize the same DVs from the previous case study.

2.4.2.2 Participants

Twenty participants (7 female and 13 male) took part in this study. The participants were between the ages of 22-34 with different occupations including student, visiting professor, post-doctoral fellow, physician, and homemaker. The participants completed two trials for each test condition. The test orders were determined via a complete balanced Latin Square design. The experimental data corresponding to participants 4 and 5 were dropped since they did not follow the protocol correctly.

2.4.2.3 Procedure

Each participant received a 15-minute tutorial after completing the consent form and demographic questionnaires. Then a 10-minute identification test was conducted in order to identify the parameters of the human and robot performance dynamics for the specific participant. After the identification test, each participant completed 6-minute tracking tasks via test conditions **C1**-**C5** and completed the task load, satisfaction and trust post-test questionnaires. The entire study, including two trials for each test condition, took around two and half hours for each participant.

2.4.2.4 Results

A one-way repeated measures ANOVA was carried out on the seven dependent variables explained in Section 2.4.2.1 in order to test the hypothesis and to determine if there were statistically significant differences in these measures among the five control schemes. The results are shown in Figures 2.11-2.17 and detailed as follows. In these figures, the average values and the upper and lower bounds of the 95% confidence interval are shown for each measure and test condition.
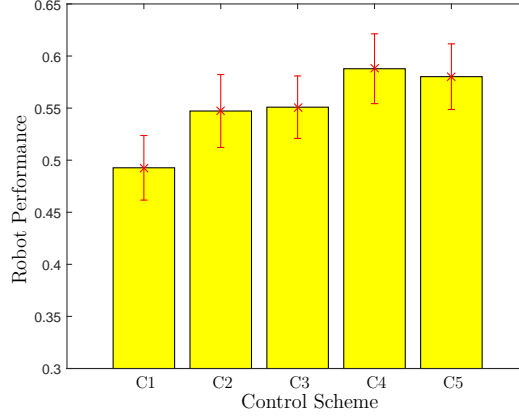
Figure 2.11: Comparison of the different control allocation conditions C1-C5 via robot performance.

Robot Performance For the average value of robot performance during each experiment, Mauchly's test of sphericity indicates that the assumption of sphericity was met, $\chi^2(9) = 10.695$, $p = 0.298$. The results elicited a statistically significant change in average robot performance over the control schemes, $F(4, 140) = 18.714$, $p < 0.0005$, and $\eta^2 = 0.348$. The average robot performance significantly increased from **C1** ($M = 0.493, SD = 0.092$) to **C2** ($M = 0.547, SD = 0.103$ $p = 0.016$, **C3** ($M = 0.551, SD = 0.088$) $p < 0.0005$, **C4** ($M = 0.588, SD = 0.099$) $p < 0.0005$, and **C5** ($M = 0.58, SD = 0.094$) $p < 0.0005$. Moreover, significant differences were observed between **C2** and **C4**, $p = 0.045$, as well as between **C3** and **C4**, $p = 0.016$. In other cases, the mean values were not significantly different. As shown in Figure 2.11, the TSC-based decision aids **C2** and **C3** can respectively improve the tracking accuracy by 10.95% and 11.76% compared to the manual mode **C1**. However, the most improvement is achieved as a result of using the robot performance maximization schemes **C4** and **C5** (i.e. 19.27% and 17.85% respectively).

Human Utilization Level For this measure, the assumption of sphericity was met as tested by Mauchly's, $\chi^2(9) = 15.030$, $p = 0.09$. A significant difference between the human utilization level among the five control schemes was observed, $F(4, 140) = 17.239$, $p < 0.0005$ and $\eta^2 = 0.33$. As shown in the Figure 2.12, the human utilization level in **C4** ($M = 0.928, SD = 0.059$) is significantly higher than **C1** ($M = 0.855, SD = 0.075$), $p < 0.0005$, **C2** ($M = 0.855, SD = 0.105$), $p = 0.004$ and **C3** ($M = 0.851, SD = 0.072$), $p < 0.0005$ (7.3%, 7.3% and 7.7% respectively). Similarly, the human utilization level in **C5** ($M = 0.95, SD = 0.057$) is significantly higher than the conditions **C1**, **C2** and **C3** (9.5%, 9.5% and 9.9% respectively). No significant difference was seen between the
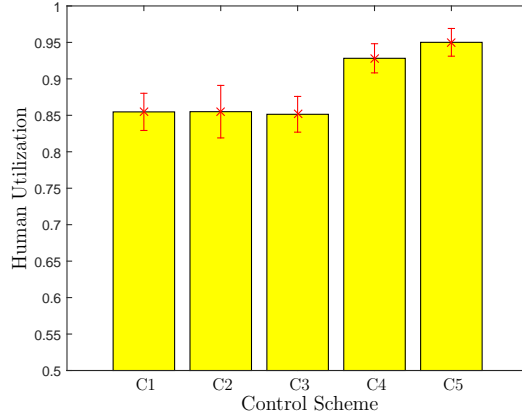
Figure 2.12: Comparison of the different control allocation conditions C1-C5 via human utilization in Eqn (2.5).

conditions **C1**, **C2** and **C3**. The difference between **C4** and **C5** was not significant either. These results indicated that the robot performance maximization scheme keeps the human in the control loop more that the manual allocation and the TSC-based schemes.
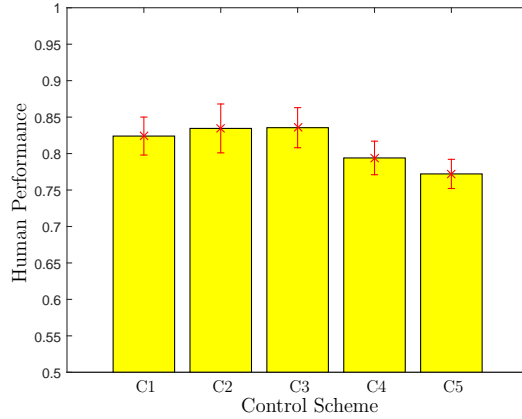
Figure 2.13: Comparison of the different control allocation conditions C1-C5 via human performance.

Human Performance The assumption of sphericity was met as indicated by the results of the Mauchly's test of sphericity $\chi^2(9) = 12.085$, $p = 0.209$ and the human performance significantly differed among the control schemes, $F(4, 140) = 8.038$, $p < 0.0005$ and $\eta^2 = 0.187$. Figure 2.13 shows the average values over all conditions and participants. Due to the higher level of human utilization in C5, human performance is significantly lower in this case ($M = 0.772 SD = 0.059$) compared to

C1 ($M = 0.824, SD = 0.078$), $p = 0.001$, and the TSC-based schemes **C2** ($M = 0.835, SD = 0.098$), $p = 0.004$ and **C3** ($M = 0.836, SD = 0.082$), $p < 0.0005$. Another significant decrease is observed from **C3** to ($M = 0.794, SD = 0.068$), $p = 0.014$ in **C4**. No significant difference between the manual mode and the TSC-based schemes **C2**-**C3** was seen. This human performance decrease in conditions **C4** and **C5** is consistent with the inverted U shape model of human performance which indicates that over-utilization of human leads to decreased performance.
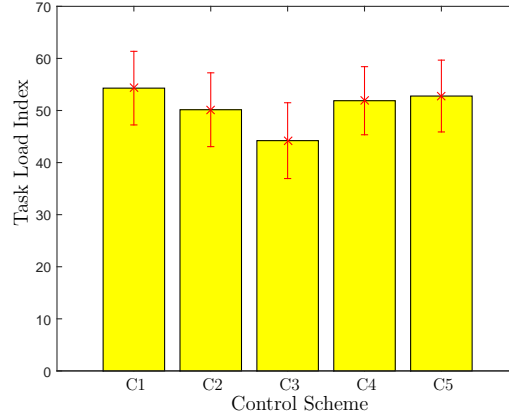
Figure 2.14: Comparison of the different control allocation conditions C1-C5 via task load index.

Perceived Task load (TLX)   The assumption of sphericity was not met as assessed by the Mauchly's test of sphericity and hence a Greenhouse-Geisser correction was applied ($\epsilon = 0.819$). A significant difference was seen between the control schemes, $F(3.275, 114.63) = 5.891$, $p = 0.001$ and $\eta^2 = 0.144$. From the pairwise comparisons, it was observed that **C3** ($M = 44.213, SD = 21.507$) entails significantly lower workload compared to all other conditions **C1** ($M = 54.296, SD = 20.884$), $p = 0.003$, **C2** ($M = 50.148, SD = 20.945$), $p = 0.04$, **C4** ($M = 51.880, SD = 19.325$), $p = 0.021$, **C5** ($M = 52.778, SD = 20.373$), $p = 0.016$ (see Figure 2.14). The reason behind this higher workload in **C1** may be the divided attention of operators between the tracking task as well as the autonomy allocation task. The higher perceived workload in conditions **C4** and **C5** could be related to the higher level of human utilization that tires the operator.

Subjective Satisfaction   The assumption of sphericity was violated as evaluated by Mauchly's test of sphericity $\chi^2(9) = 28.304$, $p = 0.001$. A Greenhouse-Geisser correction was applied ($\epsilon = 0.693$) accordingly. The subjective satisfaction scores, using the questionnaire in [65], were different
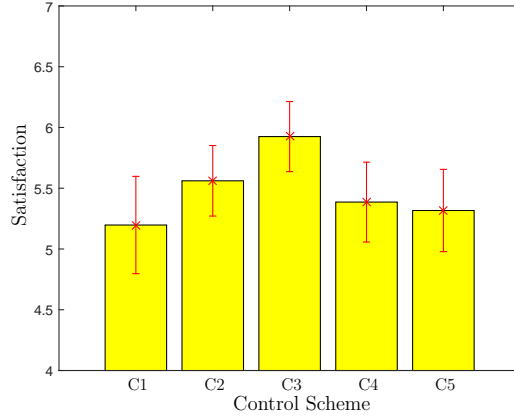
Figure 2.15: Comparison of the different control allocation conditions C1-C5 via satisfaction.

among the control schemes, $F(2.773, 97.06) = 6.734$, $p = 0.001$ and $\eta^2 = 0.161$. The control scheme **C3** ($M = 5.925, SD = 0.852$) was significantly preferred compared to the schemes **C1** ($M = 5.197, SD = 1.183$), $p = 0.016$, **C4** ($M = 5.386, SD = 0.971$), $p = 0.025$ and **C5** ($M = 5.317, SD = 1.0$) $p = 0.002$ (see Figure 2.15).
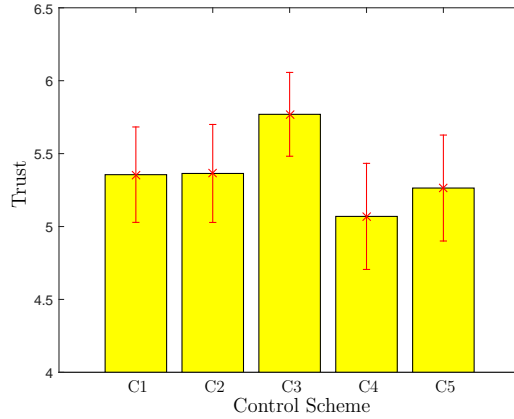
Figure 2.16: Comparison of the different control allocation conditions C1-C5 via trust.

Subjective Trust   For this subjective measure, the assumption of sphericity was not met as evaluated by Mauchly's test of sphericity $\chi^2(9) = 22.655$, $p = 0.007$. Therefore, a Greenhouse-Geisser correction was applied ($\epsilon = 0.741$). The subjective trust scores (shown in Figure 2.16) differed significantly among the control schemes, $F(2.966, 103.8) = 6.13$, $p = 0.001$ and $\eta^2 = 0.149$. The trust score of participants is significantly higher in C3 ($M = 5.769, SD = 0.849$) compared to the

conditions C2 ($M = 5.364, SD = 0.993$), $p = 0.016$, C4 ($M = 5.069, SD = 1.075$), $p = 0.005$, and C5 ($M = 5.264, SD = 1.074$), $p = 0.004$.
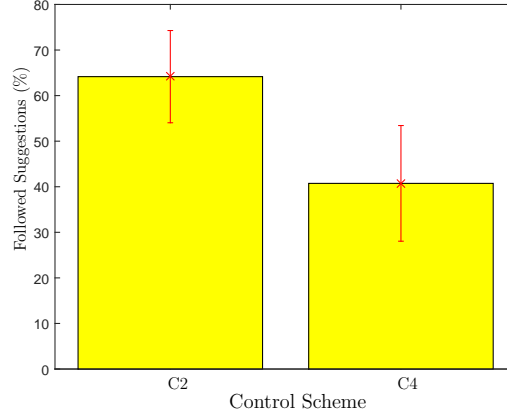
Figure 2.17: Comparison of the different control allocation conditions C1-C5 via percentage of the followed suggestions.

Percentage of the Followed Suggestions In order to compare the percentage of the suggestions that were followed in **C2** and **C4**, a dependent t-test was carried out for these two conditions. The mean values and the upper/lower bounds of the 95% confidence intervals of these two conditions are shown in the Figure 2.17. The results of the dependent t-test indicates a significant difference between **C2** ($M = 64.16, SD = 29.91$) and **C4** ($M = 40.74, SD = 37.51$); $t = 3.648$, $p = 0.001$. This implies that the suggestions of the TSC-based scheme are 23.42% more likely to be followed by the operators.

2.4.2.5 Discussions

As it was observed in the results, the TSC-based schemes **C2** and **C3** can provide a more effective switching pattern compared to the manual allocation scheme such that for the same level of human utilization, the robot performance significantly increases (i.e. Hypothesis (a)). This performance improvement happens while the decision-making is still human-like such that it entails higher satisfaction by the operators as well as the same or even slightly higher trust of operators compared to the manual mode. From the results, we also realize that the operators prefer to receive good suggestions and follow them in order to avoid higher cognitive load for making decisions about accepting or rejecting the suggestions (i.e. Hypothesis (b)). Among the automated decision aids,

the TSC-based schemes are more preferred and trusted compared to the performance maximization schemes because they strike to the operator as a human-like decision aid system (i.e. Hypothesis (c)). The robot performance maximization schemes generally give shorter and less frequent breaks to the operator in order to keep the robot performance high.

2.5   Nonlinear Model Predictive Control (NMPC) for Correcting the Decision Thresholds

In Section 2.4, we showed how the human autonomy allocation pattern can be captured via the TSC-based scheme (2.8) and how the automated decision aids can increase the overall robot performance and decrease operator's workload. Despite higher preference of participants towards the TSC-based decision aid schemes (**C2**-**C3**), participants did not follow 100% of the suggestions when they were free not to do so (i.e. in test condition **C2**). The decision aid schemes in general cause a drastic change in the decision thresholds which can prevent operators from following the decision support suggestions [13]. This is because human's adaption to a new pattern is a gradual dynamic process [57]. Therefore, in this section, we present a control framework to gradually correct the decision thresholds of the operator (i.e. TSC_l and TSC_u) towards some desired decision thresholds (denoted as TSC_{ld} and TSC_{ud}) for better robot and human performance. This is solution step 2 to overcome the misuse/disuse issues explained in Section 2.2.1. Such a decision pattern correction process should consider two subcomponents: pattern correction law and constraints on the correction laws based on the human behavioral sciences. We first define the following dynamic law in order to correct the suggested decision thresholds

$$
\begin{aligned}
TSC_u(k+1) &= TSC_u(k) + c_u(k), \\
TSC_l(k+1) &= TSC_l(k) + c_l(k),
\end{aligned}
\tag{2.40}
$$

where $c_u(k)$ and $c_l(k)$ are the corrective inputs for $TSC_u(k)$ and $TSC_l(k)$, respectively. To help the operator adapt to these changes, we propose a nonlinear model predictive control (NMPC) algorithm to gradually correct the decision thresholds (2.40). Similar concept based on a simple adaptive adjustment have been used in [13] and [99] but without consideration of state-dependent correction constraints and application in (semi)autonomous mobile robot control. Assume that $c_l(k)$

and $c_u(k)$ are constrained by

$$\underline{c}(k) \leq \{c_l(k), c_u(k)\} \leq \overline{c}(k) \tag{2.41}$$

where $\underline{c}(k)$ and $\overline{c}(k)$ are some lower and upper bounds reflecting human adaptation capabilities. Here, we propose a gradual correction algorithm for TSC_l and TSC_u based on the prediction of human utilization and robot performance. Behavioural science indicates that individuals are biased towards avoiding cognitive demand according to the "law of least mental effort" [53]. In robot control or supervisory tasks, the cognitive demand is dominant compared to the physical demands. Therefore, we expect some resistance to the change of decision thresholds from the operator as the operator's workload increases. Another finding from behavioral science worth considering is that human's subjective evaluation of a task reward gets smaller compared to the actual value of reward as the reward increases [8]. This results in gradual reduction of human's incentives at higher levels of rewards. Here we consider the robot performance as the reward. Moreover, when TSC_l and TSC_u are higher (lower), the robot performance is generally higher (lower) according to the bounds (2.15). Therefore, we expect lower willingness from the operator towards an increase in the decision thresholds when the robot performance is higher. Based on these facts, we propose the following state-dependent constraints

$$\overline{c}(k) = \frac{1 - r(k) + \frac{\overline{P}_r - P_r(k)}{\overline{P}_r - \underline{P}_r}}{2} c_b,$$
$$\underline{c}(k) = -\frac{r(k) + \frac{P_r(k) - \underline{P}_r}{\overline{P}_r - \underline{P}_r}}{2} c_b, \tag{2.42}$$

where $c_b > 0$ is a tunable constant. According to (2.42), $\underline{c}(k) \in [-c_b, 0]$ and $\overline{c}(k) \in [0, c_b]$. Therefore, based on the constraint (2.41), the choice of c_b determines the maximum corrective actions on the decision thresholds in the law (2.40). Furthermore, according to these constraints, for a fixed level of $r(k)$, as $P_r(k)$ increases (decreases), $\overline{c}(k)$ and $\underline{c}(k)$ decrease (increase). Similarly, for a fixed level of $P_r(k)$, as $r(k)$ increases (decreases), $\overline{c}(k)$ and $\underline{c}(k)$ decrease (increase). This means that human's tendency to adapt to higher (lower) TSC_u and TSC_l decreases as the human utilization (effort) and robot performance (reward) increase (decrease).

We now utilize the NMPC approach [1] to find the control input $\mathbf{u}(k) = [c_u(k)\ c_l(k)]$ such

that the following cost function is minimized

$$\min_{\mathbf{u}(0),\ldots,\mathbf{u}(N-1)} J(\mathbf{x})$$

$$= \min_{\mathbf{u}(0),\ldots,\mathbf{u}(N-1)} \sum_{i=1}^{N} \left((x_3(i) - TSC_{ud})^2 + (x_4(i) - TSC_{ld})^2 \right)$$

$$(2.43)$$

subject to the constraints (2.42) and the following dynamics

$$x_1(k+1) = a_r x_1(k) + b_r M(k),$$

$$x_2(k+1) = a_{pr} x_2(k) + (1 - a_{pr})\underline{P}_r + M(k)b_{pr}P_h(x_1(k)),$$

$$x_3(k+1) = x_3(k) + c_u(k),$$

$$x_4(k+1) = x_4(k) + c_l(k), \tag{2.44}$$

where $\mathbf{x}(k) = [r(k)\ P_r(k)\ TSC_u(k)\ TSC_l(k)]^{\mathrm{T}}$. Here $P_h(x_1(k))$ is obtained by substituting $x_1(k)$ for $r(k)$ in (2.6). Minimizing the cost function (2.43) results in the convergence of the decision thresholds to the desired levels TSC_{ld} and TSC_{ud}. To determine $M(k)$ by the switching law (2.8), $x_3(k)$ and $x_4(k)$ are substituted for TSC_u and TSC_l respectively. In (2.43), N represents the prediction horizon. The process of decision threshold correction is summarized in Algorithm 3.

Algorithm 3 Implementation of the TSC-based pattern correction using the correction law (2.40) and switching law (2.8)

1: **while** Experiment is running **do**
2:    Determine the current decision thresholds $TSC_l(k)$ and $TSC_u(k)$ by solving the NMPC problem (2.43) for the states given by (2.44) under the constraint (2.41).
3:    Calculate $TSC(k)$ using real-time values of $P_r(k)$ and $P_h(k)$ in Equation (2.1)
4:    **if** $TSC(k) \geq TSC_u(k)$ **then**
5:        Suggest the autonomous control mode
6:    **else if** $TSC(k) \leq TSC_l(k)$ **then**
7:        Suggest the manual control mode
8:    **else**
9:        Do not suggest any control mode changes
10:    **end if**
11: **end while**

The NMPC solver codes [1] were implemented on the trajectory tracking example for a pilot operator. The initial values of the operator's decision thresholds were $TSC_l(0) = 0.02$ and

$TSC_u(0) = 0.45$. The desired values were chosen as $TSC_{ld} = 0.15$ and $TSC_{ud} = 0.56$ for better robot and human performance. We used a prediction horizon $N = 200$, and $c_b = 0.36$ per hour in the algorithm. The switching pattern correction results are shown in Fig. 2.18. The decision thresholds were gradually corrected during 4 tests. It can be seen in this figure that TSC levels gradually shift towards the desired. No feeling about drastic changes was reported.
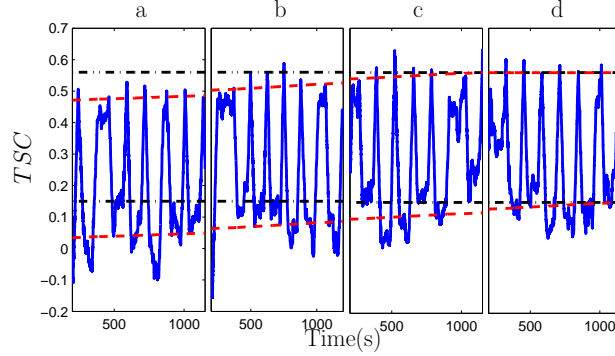
Figure 2.18: TSC-based pattern correction during 4 tests (a-d): the desired decision thresholds $TSC_{ld} = 0.1$ and $TSC_{ud} = 0.55$ (dotted-dashed lines), the decision thresholds $TSC_l(k)$ and $TSC_u(k)$ (red dashed lines), and $TSC(k)$ (blue solid line).

2.6 Conclusion

We proposed a computational trust and self-confidence based autonomy allocation scheme for the control of (semi)autonomous mobile robots. We demonstrated how this scheme can capture human autonomy allocation pattern while eliminating the effects of subjective bias and uncertainty in decision-making. We analyzed its effect on the robot performance and human workload under the steady state using rigorous mathematical derivations and also examined the theoretical results experimentally. The results showed that the proposed scheme can reduce operator workload and increase robot performance compared to the manual allocation scheme. Our human subject studies also indicated higher trust and satisfaction of participants towards this TSC-based scheme compared to manual and performance maximization schemes. Last but not the least, we designed and implemented a automated decision pattern correction algorithm to gradually adjust human autonomy allocation pattern to improve the overall robot and human performance. The solution of NMPC algorithm depends on the sampling time of the system dynamics as well as the choice of prediction horizon N. Larger values of N in general provide a more optimal solution [1] at the cost of larger

computational delay which can prevent real-time implementation. Future work will seek efficient solutions with proper choices of N and sampling time. The following chapter will investigate sliding autonomy where smooth transitions between various levels of manual and autonomous controls are utilized.

Chapter 3

Trust-Based Mixed-Initiative Bilateral Control of Mobile Robot Systems

3.1 Introduction

In a mixed-initiative control scheme, a human and an in-situ autonomous controller share the robot control task, i.e. the manual and autonomous control inputs are dynamically blended [18]. Such scheme helps to incorporate autonomous control with human capabilities in order to improve performance and reduce human workload. Some examples of this scheme include model predictive control methods [18], intelligent situation based control allocation [111], optimal blending control [97, 98], reactive shared control for obstacle avoidance and navigation [101], and Input-to-State-Stability based safe navigation method [68]. In a bilateral haptic teleoperation scheme, a human operator controls a robot remotely via a master control device while experiencing haptic force feedback cues (such as the methods proposed in [58]) in order to help the operator to control the robot more effectively [2, 69, 72, 73]. In this work, we combine the strengths of both schemes via a trust-based mixed-initiative bilateral teleoperation scheme. The proposed scheme provides shared manual and autonomous control with haptic feedback in mobile robot applications. Human-to-robot trust is utilized as a metric to dynamically blend manual and autonomous control and the intensity of the

haptic force feedback cue are adjusted according to robot-to-human trust.

Human performance in controlling the robot can degrade sporadically due to factors such as communication delay and limited feedback of environment [111]. On the other hand, in complex and uncertain environments, the performance of autonomous controller of robot will degrade due to the limitations in sensing and processing capabilities but improve under proper human guidance [18]. Human factors research shows that human's trust in a robot is dynamic and major factor that influences the use of autonomous controllers of the robot [41] and is highly dependent on robot performance [41,62]. Therefore, built on the literature, we utilize computational models of two-way trust, i.e. human-to-robot trust and robot-to-human trust, as criteria to dynamically allocate the manual and autonomous control authorities as well as the level of haptic feedback provided to the operator for improved joint performance. More specifically, we mix the manual and autonomous control with variable scales $\alpha(t)$ and $1 - \alpha(t)$, respectively. The scale $\alpha(t)$ is defined as a function of human-to-robot trust. This is the first contribution of this chapter. Objective measures are made to compute the human-to-robot trust[1] and provide human-like, however unbiased control allocation method to improve the overall task performance. We also examine whether this human-like objective autonomy allocation corresponds to higher subjective preference and trust of the human operators in an experimental study. The haptic force feedback is also scaled with a variable scale as a function of robot-to-human trust such that the operator's perception about the environment and the shared control scheme is enhanced [7,20]. The force feedback is scaled down when the robot-to-human trust is higher so that the operator perceives smaller forces and hence reduces physical workload [20].

The proposed scheme entails major changes in two key components compared to the conventional bilateral teleoperation: the communication channel and the slave side. These changes are due to the introduction of variable scales for both control inputs and haptic cues. Improper implementation of these changes can lead to passivity issues and hence may destabilize the overall control scheme. The passivity theory is a common tool in teleoperation systems which provides an energy-based perspective to analyze system property and under mild assumptions implies system stability [95]. Therefore, based on our results in [85], in this chapter we develop the framework and perform a passivity analysis for the overall proposed trust-based mixed-initiative bilateral teleop-

---

[1]Similar self-confidence measures as in Chapter 2 can be utilized here. For example, instead of just human-to-robot trust, the difference between human-to-robot trust and human self-confidence can be used. Such a replacement can be implemented within the same structure without any further consideration or issues. Here, for simplicity we just use the trust as a measure.

eration scheme in order to guarantee the stability. More specifically, as the second contribution of this chapter, we propose a wave/scattering transformation to establish a passive, and hence stable, communication channel between the master device and the teleoperated slave robot in the presence of time-varying delays and variable power scaling. We also guarantee the passivity of the slave robot in the presence of artificial force feedback algorithms as well as the scaled local autonomous control and via passivity observers (PO) and passivity controllers (PC). Then, as the third contribution of this chapter, we provide guidelines for improved transparency of the force feedback and velocity signals while still maintaining the overall passivity and stability of the system. Finally, we conduct a through human subject study via actual Unmanned Aerial Vehicle (UAV) and ground robots and perform a statistical analysis of the test results via various objective and subjective measures. The tests show that our proposed scheme improves task performance by 12.76% and reduces operator workload by 10.71% and is more preferred compared to a mixed-initiative with manual autonomy allocation. The proposed scheme is also more trusted by the participants compared to its optimal autonomy allocation counterpart.

The organization of the rest of the chapter is as follows. The proposed trust-based mixed-initiative teleoperation scheme is presented in Section 3.2. A brief introduction of passivity theory and M-port is provided in Section 3.3. Passivity analysis for the master haptic device, communication channel in the presence of time-varying delays and power scaling variables, as well as the slave robot with variable scaled output are presented in Sections 3.4, 3.5, and 3.6, respectively. A preliminary case study on teleoperated UAV tracking a UGV is presented in Section 3.8. The experiment results of a thorough case study with multiple human subject tests are presented and analyzed in Section 3.9. Section 3.10 concludes the chapter.

3.2   Trust-Based Mixed-Initiative Teleoperation

In this section, we present our proposed trust-based mixed-initiative teleoperation scheme for applications in mobile robotic systems as shown in Fig. 3.1. The mixed-initiative control scheme integrates human's commands received through the communication channel with autonomous control commands via variable allocation scales $\alpha(t) \in (0, 1]$ and $1 - \alpha(t)$, respectively. A variable scale $\beta(t)$ also scales the force feedback cues to provide various levels of assistance to the operator. Such scheme is enabled via major subsystems consisting of a master device (i.e. block B2 detailed in
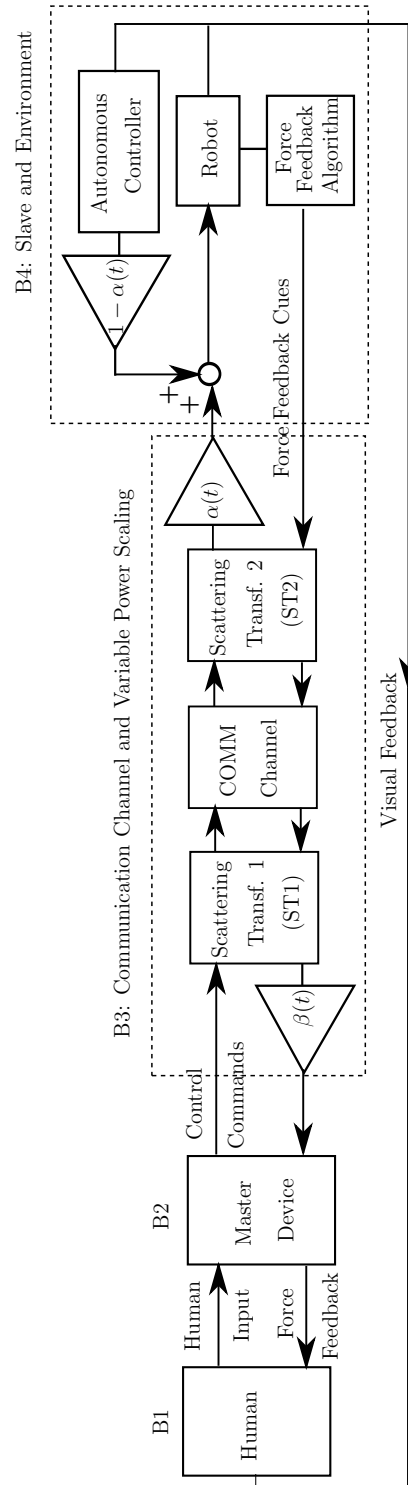
Figure 3.1: Block diagram for the trust-based mixed-initiative bilateral teleoperation.

Section 3.4) for sending control commands of human human (B1) as well as applying force feedback cues, a passive communication channel including time varying delays and the variable scales α, β (B3 detailed in Section 3.5), and a slave system including the robot, autonomous controller and force feedback algorithms (B4 detailed in Section 3.6). Next, we define the range of the trust-based variable scaling parameters α and β according to the following:

$$0 < \underline{\alpha} \le \alpha(t) \le \overline{\alpha} \le 1, \quad 0 < \underline{\beta} \le \beta(t) \le \overline{\beta}, \tag{3.1}$$

where the positive constants $\underline{\alpha}, \overline{\alpha}, \underline{\beta}, \overline{\beta}$ are choices that determine the lower and upper bounds on $\alpha(t)$ and $\beta(t)$ for a specific task requirement[2]. Here, we define the control allocation scale $\alpha(t)$ as a function of human-to-robot trust, denoted as $T_{hr}(t)$. Moreover, we defined the variable scale $\beta(t)$ as a function of robot-to-human trust, denoted as $T_{rh}(t)$. Next, we present the computational models for $T_{hr}(t)$ and $T_{rh}(t)$ and the corresponding functions for the variable scales $\alpha(t)$ and $\beta(t)$.

Human factors research indicates that trust is dynamic and highly dependent on robot performance [41, 62]. Based on these performance-centric criteria, we propose the computational models of human-to-robot trust $T_{hr}(t)$ and robot-to-human trust $T_{rh}(t)$ according to the following in order to capture the dynamic trust evolution:

$$\dot{T}_{hr}(t) = -a_{hr}\frac{T_{hr}(t) - \underline{T}_{hr}}{\overline{T}_{hr} - \underline{T}_{hr}} + b_{hr}\frac{P_r(t) - \underline{P}_r}{\overline{P}_r - \underline{P}_r} \tag{3.2}$$

$$\dot{T}_{rh}(t) = -a_{rh}\frac{T_{rh}(t) - \underline{T}_{rh}}{\overline{T}_{rh} - \underline{T}_{rh}} + b_{rh}\frac{P_h(t) - \underline{P}_h}{\overline{P}_h - \underline{P}_h} \tag{3.3}$$

where the constants $0 < a_{hr} \le 1$ and $0 < b_{hr} \le 1$ define the sensitivity of the dynamics of human trust to the current level of human-to-robot trust $T_{hr}(t)$ and robot performance $P_r(t)$. Similarly, the constants $0 < a_{rh} \le 1$ and $0 < b_{rh} \le 1$ define the sensitivity of the dynamics of robot trust to $T_{rh}(t)$ and $P_h(t)$. For these trust models, when both $P_r(t)$ and $P_h(t)$ are bounded in $P_r(t) \in [\underline{P}_r, \overline{P}_r]$ and $P_h(t) \in [\underline{P}_h, \overline{P}_h]$, the trust levels $T_{hr}(t)$ and $T_{rh(t)}$ are bounded as well, i.e.

$$T_{hr}(t) \in [\underline{T}_{hr}, \overline{T}_{hr}], \quad T_{rh}(t) \in [\underline{T}_{rh}, \overline{T}_{rh}]. \tag{3.4}$$

The bounds in (3.4) represent the acceptable ranges of trust to avoid either human-robot over-

---

[2]Since choices $\underline{\alpha} = 0$ and $\underline{\beta} = 0$ can result in a unilateral teleoperation instead of bilateral, we eliminate these values from the bound choices.

reliance or under-reliance. The level $\overline{T}_{hr}$ ($\overline{T}_{rh}$) is achievable with $P_r(t) = \overline{P}_r$ ($P_h(t) = \overline{P}_h$) when the sensitivity constants are chosen as $a_{hr} = b_{hr}$ ($a_{rh} = b_{rh}$).

Remark 8 *Note that trust model $T_{hr}(t)$ in (3.2) is a computational that provides a performance-centric evaluation of human trust in robot, which has been shown as the major factor impacting trust [41]. Although this is not a model for the actual human-to-robot trust, which is latent and usually difficult to measure and model precisely, we utilize such a model as a human-like but objective measure to provide automated autonomy allocation in the proposed scheme for improved task performance. In the experiments carried out in Section 3.9, we examine the effectiveness of such a human-like model and allocation scheme and how the participants trust and prefer it. Similarly, the computational robot-to-human trust model in (3.3) mimics the human trust model (3.2) as a function of prior trust and human performance. This does not mean that the robot will have actual trust or feeling towards the human. The proposed computational trust models improve the transparency of human and robot capabilities during the operation.* •

We now explain the functions chosen for $\alpha(t)$ and $\beta(t)$ (See Fig. 3.2) based on the bounds in (3.4). Define $\alpha(t)$ and $\beta(t)$ using the smooth logistic functions given by

$$\alpha(t) = \overline{\alpha} - \frac{\overline{\alpha} - \underline{\alpha}}{1 + e^{-s_\alpha \frac{T_{hr}(t) - b_\alpha}{\overline{T}_{hr} - \underline{T}_{hr}}}} \tag{3.5a}$$

$$\beta(t) = \overline{\beta} - \frac{\overline{\beta} - \underline{\beta}}{1 + e^{-s_\beta \frac{T_{rh}(t) - b_\beta}{\overline{T}_{rh} - \underline{T}_{rh}}}}. \tag{3.5b}$$

The positive constants b_α and b_β determine the midpoint (bias) of the curve:

$$\alpha(t)\big|_{T_{hr}(t) = b_\alpha} = \frac{\overline{\alpha} + \underline{\alpha}}{2}, \quad \beta(t)\big|_{T_{rh}(t) = b_\beta} = \frac{\overline{\beta} + \underline{\beta}}{2}.$$

For symmetric scaling, we define $b_\alpha \triangleq \frac{\overline{T}_{hr} + \underline{T}_{hr}}{2}$ and $b_\beta \triangleq \frac{\overline{T}_{rh} + \underline{T}_{rh}}{2}$. The positive constants s_α and s_β determine the steepness of the curves. The larger s_α and s_β, the steeper the curves. When $s_\alpha \to \infty$ or $s_\beta \to \infty$, the scaling functions (3.5) will converge to a hard step function. We choose $s_\alpha \geq 10$ and $s_\beta \geq 10$ to guarantee that

$$\alpha(t)\big|_{T_{hr}(t) = \underline{T}_{hr}} \to \overline{\alpha}, \quad \alpha(t)\big|_{T_{hr}(t) = \overline{T}_{hr}} \to \underline{\alpha}$$

$$\beta(t)\big|_{T_{rh}(t) = \underline{T}_{rh}} \to \overline{\beta}, \quad \beta(t)\big|_{T_{rh}(t) = \overline{T}_{rh}} \to \underline{\beta}.$$
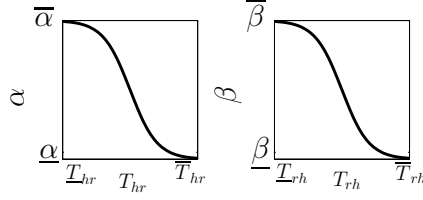
Figure 3.2: Trust-based scaling variables according to Eqn. (3.5).

Remark 9 *According to the functions (3.5) shown in Figure 3.2, when the human trust in robot is lower, the value of $\alpha(t)$ is higher such that the autonomous controller contribution less in the mixed-initiative control of robot and vice versa. Similarly, for lower values of the robot-to-human trust, the value of $\beta(t)$ is higher which makes the human operator receive larger force feedback cues for performance improvement and vice versa. Such computational models for two-way trust and the scaling variables are built according to the nonlinear model obtained experimentally in [38] which indicates lower (higher) reliance on automation when the human trust in automation is lower (higher).*

•

For the sake of comparison, we also propose a nonsmooth model for the scaling variables $\alpha'(t)$ and $\beta'(t)$ using step-like functions in the following

$$\alpha'(t) = \overline{\alpha} + (\underline{\alpha} - \overline{\alpha})H(T_{hr}(t) - b_{\alpha'})$$
$$\beta'(t) = \overline{\beta} + (\underline{\beta} - \overline{\beta})H(T_{rh}(t) - b_{\beta'}) \tag{3.6}$$

where $H(\cdot)$ is the Heaviside function and $b_{\alpha'} \in (\underline{T}_{hr}, \overline{T}_{hr})$ and $b_{\beta'} \in (\underline{T}_{rh}, \overline{T}_{rh})$ are two decision thresholds for switching the levels of $\alpha'(t)$ and $\beta'(t)$. The hard step changes are assumed to be more noticeable to the operator compared to the smooth gradual changes of $\alpha(t)$ and $\beta(t)$ according to Eqn. (3.5). We will compare the effect of using the smooth logistic functions and the nonsmooth functions and obtain operators' evaluation in Section 3.8.

3.3   Passivity Definition

In this section, we summarize the passivity definitions and the corresponding notation that will be used in Sections 3.4, 3.5, and 3.6 to guarantee the passivity of the overall mixed-initiative
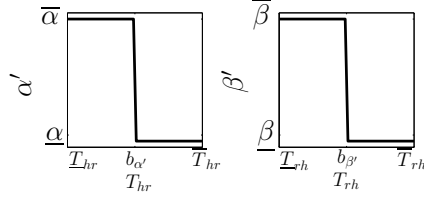
Figure 3.3: Hard step functions for trust-based scaling variables.

teleoperation scheme. Guaranteeing passivity implies the components in the overall control scheme are interacting in a proper way which results in the stability of the overall control scheme.

Definition 1 *[95] Define a scalar power supply into a system Z as $P(t) = \mathbf{y}^{\mathrm{T}}(t)\mathbf{u}(t)$ where $\mathbf{u}(t), \mathbf{y}(t) \in \mathbb{R}^p$ are the power conjugate inputs and outputs, respectively. System Z with a lower bounded storage function $V(t)$ is passive if the following holds*

$$\int_0^t \mathbf{y}^{\mathrm{T}}(\tau)\mathbf{u}(\tau)d\tau + V(0) \geq V(t) \geq 0. \tag{3.7}$$

Or, when $V(t)$ is differentiable we have $\dot{V}(t) \leq \mathbf{y}^{\mathrm{T}}(t)\mathbf{u}(t)$. Condition (3.7) means that the total energy extracted from the system is bounded by the initial energy $V(0)$ of the system and the energy supplied to it via $\mathbf{y}^{\mathrm{T}}(t)\mathbf{u}(t)$.

Teleoperation systems include multiple components interacting with each other through force $\mathbf{f}(t)$ and velocity $\mathbf{v}(t)$ power variables [42]. Utilizing a mechanical/electrical analogy, these components are usually modeled as M-port networks as shown in Fig. 3.4. For such a model to be passive, the passivity condition (3.7) must hold for $\mathbf{y}^{\mathrm{T}}(t)\mathbf{u}(t) \triangleq \mathbf{v}_1^{\mathrm{T}}(t)\mathbf{f}_1(t) + \cdots + \mathbf{v}_{\mathrm{M}}^{\mathrm{T}}(t)\mathbf{f}_{\mathrm{M}}(t)$. In this chapter, as illustrated in Fig. 3.5, we are particularly interested in the passivity of one-port and two-port models which form the components of the control scheme proposed. It is widely known that cascade interconnection of passive one-port and/or two-port system is still passive [73]. Therefore, we need to guarantee the passivity of each block such that the cascaded system shown in Fig. 3.5 is passive and hence stable. Here we assume that the human behaves as a passive system, which is common in the literature[3]. The details of components B2-B4 will be presented in the following sections.

---

[3]Human actions might not be passive in general but they can become passive with proper passivation methods such as high-pass filtering of human commands [43]. Analysis of passivity of human actions deserve a separate study and is out of the scope of this dissertation.
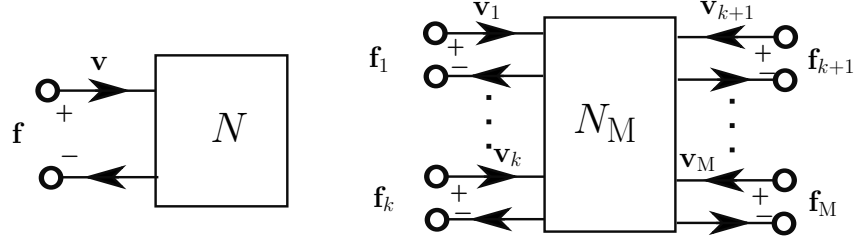
Figure 3.4: One-port and M-port components.
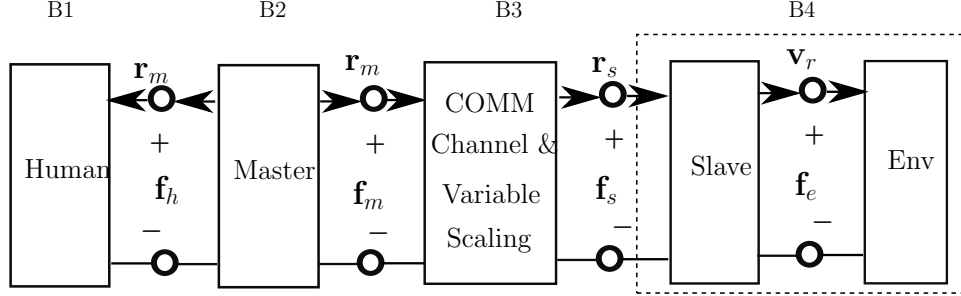
Figure 3.5: Port-based model of mixed-initiative teleoperation.

3.4 The Haptic Feedback Controller Device
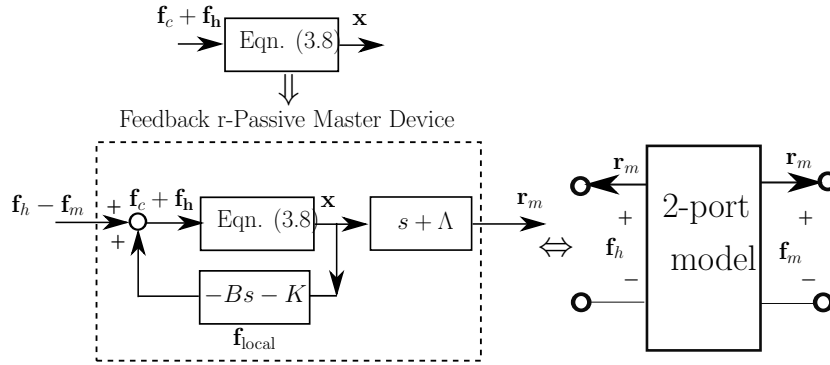
Figure 3.6: Feedback r-passivity of the master-device.

Reminding that we consider the control of a mobile robot in this work, the haptic device is used to send rate control commands (such as velocity) to the robot. In such cases, we need to overcome kinematic dissimilarities between the master and slave due to the mapping of limited workspace of the master control device to an unlimited workspace of robot in the environment [60]. A solution is to couple the position readings of haptic device to the velocity commands of robot and utilize the feedback r-passivity method [60] to addresses guarantee the passivity of haptic device as illustrated in Fig. 3.6. As shown below, this method utilizes a local feedback control loop to

guarantee a passive master haptic device with respect to the force input and an output called $\mathbf{r}_m$ which contains position information of the haptic device and is suitable for sending rate velocity commands to the robot. Consider the following generic model of a non-redundant haptic device

$$M(\mathbf{x})\ddot{\mathbf{x}} + C(\mathbf{x}, \dot{\mathbf{x}})\dot{\mathbf{x}} = \mathbf{f}_c + \mathbf{f}_h, \tag{3.8}$$

where $\mathbf{x} \in \mathbb{R}^n$ is the position of the end effector of the haptic device, n is the DoF of device, $\mathbf{f}_c \in \mathbb{R}^n$ is the control force, and $\mathbf{f}_h \in \mathbb{R}^n$ is the external force applied by the human operator, $M(\mathbf{x}) \in \mathbb{R}^{n \times n}$ is the inertia matrix, and $C(\mathbf{x}, \dot{\mathbf{x}}) \in \mathbb{R}^{n \times n}$ is the Coriolis matrix. We assume that a local controller has compensated the gravity effects. Let $\mathbf{f}_c = \mathbf{f}_{\text{local}} - \mathbf{f}_m$, where $\mathbf{f}_{\text{local}}$ is a local passivation force, and $\mathbf{f}_m$ is the force feedback cue received through the bilateral teleoperation scheme. According to [60], applying a local Proportional Derivative (PD) controller

$$\mathbf{f}_{\text{local}} = -B\dot{\mathbf{x}} - K\mathbf{x},$$

$$B = \text{diag}[b_1, ..., b_n] \in \mathbb{R}^{n \times n}, b_j > 0, j = 1, ..., n,$$

$$K = \text{diag}[k_1, ..., k_p, 0, ..., 0] \in \mathbb{R}^{n \times n}, k_i > 0, i = 1, ..., p \leq n$$

with large enough proportional and derivative gains guarantees the passivity of the master device with respect to the input force $\mathbf{f}_h - \mathbf{f}_m$ and a new output $\mathbf{r}_m = \dot{\mathbf{x}} + \Lambda\mathbf{x}$ where $\Lambda = \text{diag}[\lambda_1, \lambda_2, ..., \lambda_p, 0, ..., 0] \in \mathbb{R}^{n \times n}$ with $\lambda_i > 0$ is a weight matrix such that for the storage function

$$V_{hd}(t) := \frac{1}{2}\left[\mathbf{r}_m^{\text{T}} M \mathbf{r}_m + \mathbf{x}_m^{\text{T}}(K + \Lambda B - \Lambda M \Lambda)\mathbf{x}_m\right] \geq 0. \tag{3.9}$$

and the following positive semi-definite function

$$S_{hd}(t) := \dot{\mathbf{x}}_m^{\text{T}}\left[B - \frac{1}{2}(M\Lambda + \Lambda M)\right]\dot{\mathbf{x}}_m + \mathbf{x}_m^{\text{T}}\Lambda K \mathbf{x}_m - \mathbf{x}_m^{\text{T}}\Lambda C\dot{\mathbf{x}}_m \geq 0. \tag{3.10}$$

we have $\mathbf{r}_m^{\text{T}}(t)(\mathbf{f}_h(t) - \mathbf{f}_m(t)) = \dot{V}_{hd}(t) + S_{hd}(t)$ and

$$\int_0^t \mathbf{r}_m^{\text{T}}(\tau)(\mathbf{f}_h(\tau) - \mathbf{f}_m(\tau))d\tau = V_{hd}(t) - V_{hd}(0) + \int_0^t S_{hd}(\tau)d\tau \geq -V_{hd}(0). \tag{3.11}$$

For the proof see [60]. The passivity condition (3.7) is also satisfied following the 2-port equivalent

63

shown in Fig. 3.6. Proper choice of Λ (i.e. large enough λ_i[4]) results in a position-like output $\mathbf{r}_m$ because $\Lambda\mathbf{x}$ becomes dominant in the output $\mathbf{r}_m$ compared to the velocity $\dot{\mathbf{x}}$.

3.5   Variable Power Scaling

In this section, we develop a wave/scattering transformation for the communication channel B3 shown in Fig. 3.7. The proposed transformation guarantees that the communication channel remains passive in the presence of time-varying power scaling (i.e. $\alpha(t)$ and $\beta(t)$) and time-varying communication delays (i.e. $T_1(t)$ and $T_2(t)$). It has been shown that delay has an adverse effect on the stability of the communication channel in bilateral teleoperation [2, 73]. In the passivity theory framework, wave/scattering transformation as well as time-varying communication gains have been utilized to passivate communication channels with constant and time-varying delays [2,69,73]. Passivity-based methods have also been used to stabilize the interconnection between the master and slave sides in the presence of constant and variable power scaling [7,89,90]. However, the problem of variable power scaling in the presence of time-varying delays in a communication channel, required for the proposed scheme in Fig. 3.1, has not been addressed in previous works. Time-varying delays can occur in teleoperation due to various factors such as congestion and distance [69].

B3: Communication Channel and Variable Scaling Parameters
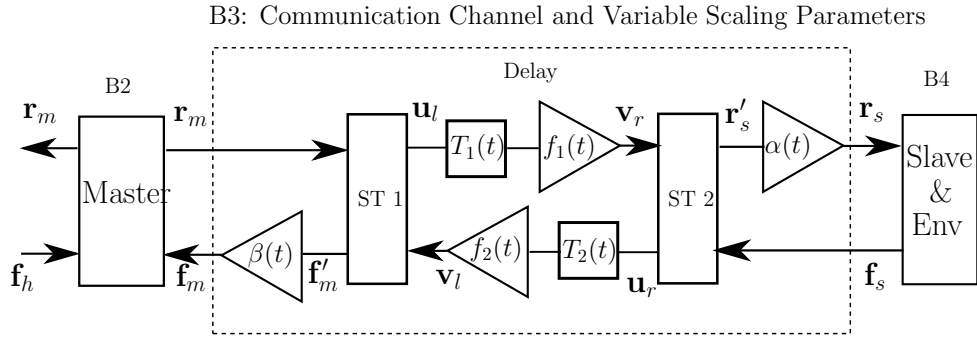
Figure 3.7: Block diagram for the communication channel with time-varying delays and variable power scaling.

Definition 2 *Let $E(t)$ represent the energy stored in a communication channel with a scheme shown in Fig. 3.7. Consider the two-port network equivalent of this channel in Fig. 3.8. According to this figure, the power flow into this block is determined by $\mathbf{y}^{\mathrm{T}}(t)\mathbf{u}(t) \triangleq \mathbf{r}_m^{\mathrm{T}}(t)\mathbf{f}_m(t) - \mathbf{r}_s^{\mathrm{T}}(t)\mathbf{f}_s(t)$ [73].*

---

[4]The weight Λ can be chosen arbitrary large by the proper choice of B and K as explained in [60].
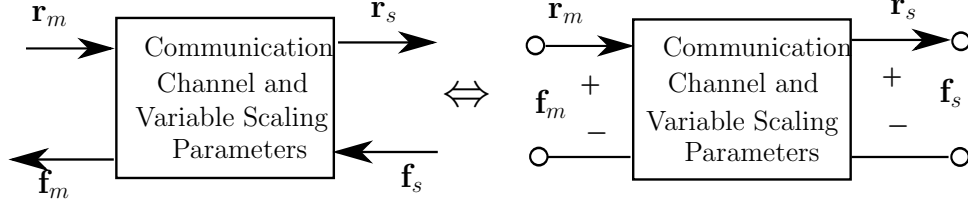
Figure 3.8: Two-port equivalent of the communication channel.

Therefore, assuming that no energy is initially stored, i.e. $E(0) = 0$, the communication channel is passive if Equation (3.7) holds, i.e. $\int_0^t \mathbf{r}_m^{\mathrm{T}}(\tau)\mathbf{f}_m(\tau) - \mathbf{r}_s^{\mathrm{T}}(\tau)\mathbf{f}_s(\tau)d\tau \geq 0$.

Theorem 3 *For the communication channel shown in Fig. 3.7, assume that the following power scaling is used*

$$\mathbf{r}_s = \alpha(t)\mathbf{r}'_s, \quad \mathbf{f}_m = \beta(t)\mathbf{f}'_m, \tag{3.12}$$

where $\mathbf{r}'_s \in \mathbb{R}^p$ is the operator control command received through the communication channel with its scaled form being $\mathbf{r}_s$, and $\mathbf{f}'_m \in \mathbb{R}^p$ is the force feedback command received through the communication channel with its scaled form being $\mathbf{f}_m$. It is further assumed that $\frac{dT_i}{dt} \leq \dot{T}_{i\,\mathrm{max}} \leq 1, i = 1,2$ where $\dot{T}_{i\,\mathrm{max}}$ is the maximum rate of increase of time-varying delay $T_i(t)$ [69]. The communication channel is passive in the sense of Definition 2, if the wave variables $\mathbf{u}_l$, $\mathbf{v}_l$, $\mathbf{u}_r$, $\mathbf{v}_r$ (in ST1 and ST2) and passivation gains $f_1(t)$ and $f_2(t)$ are chosen as

$$\mathbf{u}_l = \sqrt{\frac{\overline{\beta}}{2b}}(\mathbf{f}'_m + b\mathbf{r}_m), \quad \mathbf{v}_l = \sqrt{\frac{\overline{\beta}}{2b}}(\mathbf{f}'_m - b\mathbf{r}_m),$$

$$\mathbf{u}_r = \sqrt{\frac{\overline{\alpha}}{2b}}(\mathbf{f}_s - b\mathbf{r}'_s), \quad \mathbf{v}_r = \sqrt{\frac{\overline{\alpha}}{2b}}(\mathbf{f}_s + b\mathbf{r}'_s)$$

$$f_i(t) = \sqrt{1 - \dot{T}_{i\,\mathrm{max}}}, \quad i = 1,2, \tag{3.13}$$

with $\underline{\alpha}$, $\overline{\alpha}$, $\underline{\beta}$ and $\overline{\beta}$ being defined as in (3.1), and $b > 0$ is a constant determining the characteristic impedance.

Proof. From the transformations (3.13), we have

$$\mathbf{f}'_m = \sqrt{\frac{b}{2}}(\frac{\mathbf{u}_l}{\sqrt{\underline{\beta}}} + \frac{\mathbf{v}_l}{\sqrt{\overline{\beta}}}), \quad \mathbf{f}_s = \sqrt{\frac{b}{2}}(\frac{\mathbf{v}_r}{\sqrt{\overline{\alpha}}} + \frac{\mathbf{u}_r}{\sqrt{\underline{\alpha}}})$$

$$\mathbf{r}_m = \frac{1}{\sqrt{2b}}(\frac{\mathbf{u}_l}{\sqrt{\underline{\beta}}} - \frac{\mathbf{v}_l}{\sqrt{\overline{\beta}}}), \quad \mathbf{r}'_s = \frac{1}{\sqrt{2b}}(\frac{\mathbf{v}_r}{\sqrt{\overline{\alpha}}} - \frac{\mathbf{u}_r}{\sqrt{\underline{\alpha}}}). \tag{3.14}$$

Combining the variable power scaling (3.12) with Equation (3.14), we obtain the energy stored in the communication channel

$$\int_0^t \mathbf{r}_m^T(\tau)\mathbf{f}_m(\tau) - \mathbf{r}_s^T(\tau)\mathbf{f}_s(\tau)d\tau = \int_0^t \frac{\beta(\tau)}{2}\left(\frac{\mathbf{u}_l^T(\tau)\mathbf{u}_l(\tau)}{\underline{\beta}} - \frac{\mathbf{v}_l^T(\tau)\mathbf{v}_l(\tau)}{\overline{\beta}}\right)$$
$$- \frac{\alpha(\tau)}{2}\left(\frac{\mathbf{v}_r^T(\tau)\mathbf{v}_r(\tau)}{\overline{\alpha}} - \frac{\mathbf{u}_r^T(\tau)\mathbf{u}_r(\tau)}{\underline{\alpha}}\right)d\tau. \tag{3.15}$$

From the bounds on $\alpha(t)$ and $\beta(t)$ in (3.1), Equation (3.15) is lower bounded by $\frac{1}{2}\int_0^t \mathbf{u}_l^T(\tau)\mathbf{u}_l(\tau) - \mathbf{v}_l^T(\tau)\mathbf{v}_l(\tau) + \mathbf{u}_r^T(\tau)\mathbf{u}_r(\tau) - \mathbf{v}_r^T(\tau)\mathbf{v}_r(\tau)d\tau$. If this lower bound is non-negative, (3.15) will be non-negative and hence the communication channel will be passive. From Fig. 3.7 we know that

$$\mathbf{v}_r(t) = f_1(t)\mathbf{u}_l(t - T_1(t)), \quad \mathbf{v}_l(t) = f_2(t)\mathbf{u}_r(t - T_2(t)). \tag{3.16}$$

Thus, utilizing Equation (3.16), the lower bound becomes

$$\frac{1}{2}\int_0^t \mathbf{u}_l^T(\tau)\mathbf{u}_l(\tau) - f_1^2(\tau)\mathbf{u}_l^T(\tau - T_1(\tau))\mathbf{u}_l(\tau - T_1(\tau))$$
$$+ \mathbf{u}_r^T(\tau)\mathbf{u}_r(\tau) - f_2^2(\tau)\mathbf{u}_r^T(\tau - T_2(\tau))\mathbf{u}_r(\tau - T_2(\tau))d\tau \tag{3.17}$$

Utilizing the change of variables (i.e. $\sigma_i = \tau - T_i(\tau) \triangleq g_i(\tau), i = 1, 2$) and Equation (9) in [69], we rewrite (3.17) as

$$\frac{1}{2}\left[\int_{t-T_1(t)}^t \mathbf{u}_l^T(\tau)\mathbf{u}_l(\tau)d\tau + \int_{t-T_2(t)}^t \mathbf{u}_r^T(\tau)\mathbf{u}_r(\tau)d\tau + \int_0^{t-T_1(t)} \frac{1 - T_1'(\sigma) - f_1^2(\sigma)}{1 - T_1'(\sigma)}\mathbf{u}_l^T(\sigma)\mathbf{u}_l(\sigma)d\sigma\right.$$
$$\left.+ \int_0^{t-T_2(t)} \frac{1 - T_2'(\sigma) - f_2^2(\sigma)}{1 - T_2'(\sigma)}\mathbf{u}_r^T(\sigma)\mathbf{u}_r(\sigma)d\sigma\right] \tag{3.18}$$

where $T_i' := \frac{dT_i}{d\tau}\big|_{\tau=g_i^{-1}(\sigma)}$ is the rate of change of $T_i(t)$. The first two integrals in (3.18) are positive semi-definite. Choosing $f_i(t)$ such that $f_i^2 \le 1 - \frac{dT_i}{dt}, i = 1, 2$ guarantees that the other two integrals

66

are positive semi-definite too. From the assumptions in Theorem 3 we know that $\frac{dT_i}{dt} \leq \dot{T}_{i\,\max} \leq 1$. So, we can choose constant values $f_i = \sqrt{1 - \dot{T}_{i\,\max}}$ such that (3.18) is positive semi-definite which means $\int_0^t \mathbf{r}_m^{\mathrm{T}}(\tau)\mathbf{f}_m(\tau) - \mathbf{r}_s^{\mathrm{T}}(\tau)\mathbf{f}_s(\tau)d\tau \geq 0$, i.e. the communication channel is passive according to Definition 2. This completes the proof. ∎

Remark 10 *For constant delays (i.e. $T_1(t) = T_2(t) = T$), choosing $f_i = 1, i = 1, 2$ results in a passive communication channel in the presence of variable power scaling $\alpha(t)$ and $\beta(t)$. Moreover, when no variable power scaling is applied (i.e. $\overline{\alpha} = \underline{\alpha} = 1$ and $\overline{\beta} = \underline{\beta} = 1$), the wave/scattering transformation recovers the standard form in [2, 73].* •

Remark 11 *The results obtained in this section are not restricted to trust-based schemes. Any other mixed-initiative teleoperation scheme that follows the scheme shown in Fig. 3.7 will be applicable.* •

3.6 Slave Side

A more detailed block diagram of the slave side is illustrated in Fig. 3.9. An autonomous controller A_c scaled with $1 - \alpha(t)$, together with the scaled human commands received through communication channel (i.e. $\mathbf{r}_s = \alpha(t)\mathbf{r}_s'$) are mixed to form the total velocity control command of the robot $\mathbf{v}_{ref}$. Here we need to clarify the difference between the high-level autonomous controller A_c and the low-level velocity tracking controller (i.e. the LLC block in Fig. 3.9) of a robot (the R block). Many commercial robots receive forward linear and rotational velocity control commands as the high-level control while an inner control loop that deals with low-level control (e.g. under actuation and disturbance) guarantees a good velocity tracking via applying $\mathbf{f}_{rc}$. Here, we assume such low-level control (LLC) is already applied [48] and A_c forms a higher-level task-based control that contributes to the $\mathbf{v}_{ref}$ command when controlling the robot. The block FFA represents some force feedback algorithm that produces force feedback cues for the operator (see [58] for example algorithms)[5].

Variable power scaling $1 - \alpha(t)$ and the FFA block can be possible sources of losing the passivity. We utilize passivity observer (PO) and passivity controller (PC) components (shown in Fig. 3.9) to guarantee the passivity of slave side. As it can be seen in Fig. 3.9, slave is in interaction with environment via the power port $(\mathbf{v}_r, \mathbf{f}_e)$ and with the communication channel via the power

---

[5]Note that the study of different types of force feedback is not the focus of this chapter. Here we use a simple spring-like force to be explained in Section 3.8.
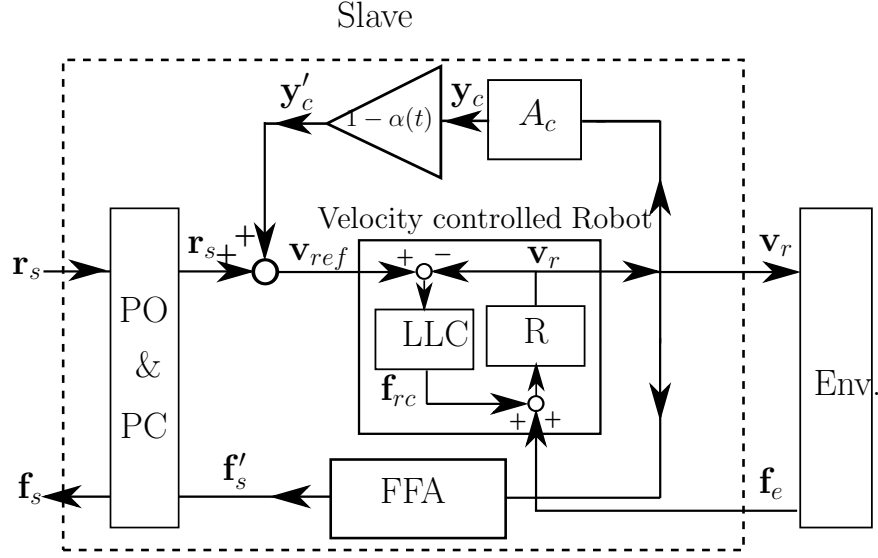
Figure 3.9: Block diagram of the slave side.

port $(\mathbf{r}_s, \mathbf{f}_s)$. The passivity of slave in interaction with environment can be examined and guaranteed via the port $(\mathbf{r}_s, \mathbf{f}_s)$ (see Section II in [42] for the proof of connected "networks with one open end").

Consider a system N with impedance causality [42], i.e. a system with velocity input and force output. Figure 3.10 illustrates the system with a passivity observer (PO) and a passivity controller (PC) as well as its one-port equivalent. This system can exchange energy with other systems via the power supply $\mathbf{v}^{\mathrm{T}}(t)\mathbf{f}(t)$. Assume that no initial energy is stored in this system (i.e. $E(0) = 0$), we design the PO and PC blocks to guarantee system passivity in the sense of Equation (3.7) with $\mathbf{y}^{\mathrm{T}}(t)\mathbf{u}(t) \triangleq \mathbf{v}^{\mathrm{T}}(t)\mathbf{f}(t)$. The basic idea is as follows. The PO tracks the energy of the system N and detects when it is about to become active (i.e. the system is about to exhibit $\int_0^t \mathbf{v}^{\mathrm{T}}(\tau)\mathbf{f}(\tau)d\tau < 0$). A scalar time-varying dissipation element $z(t)$ is then activated, via which the PC modifies the output $\mathbf{f}(t)$ such that extra energy produced by N is dissipated via proper dissipation action. The PO and PC concepts were first introduced in [42]. Here, we develop their continuous-time counterparts in the following theorem.

Theorem 4 *Consider a system N with impedance causality. Define a passivity observer PO with an energy observer function $E_{obs}(t) = \int_0^{t^-} \mathbf{v}^{\mathrm{T}}(\tau)\mathbf{f}(\tau)d\tau$, and a time-varying dissipation activation*
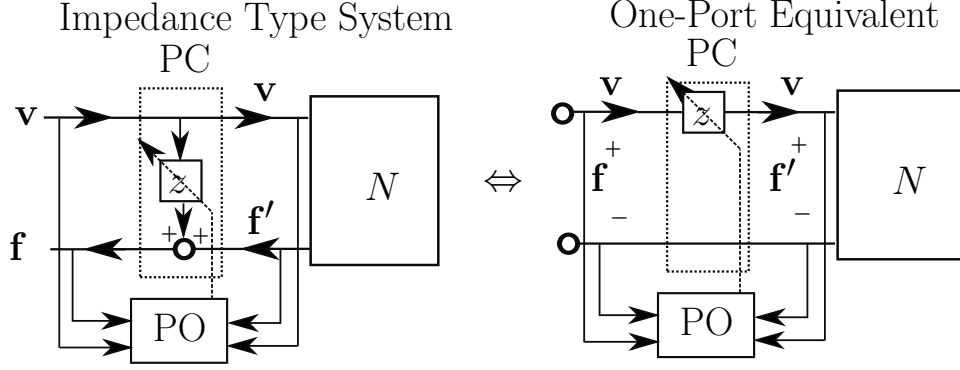
Figure 3.10: Passivation of impedance type system using passivity observer (PO) in (3.19) and passivity controller (PC) in (3.20).

function

$$z(t) = \begin{cases} -\dfrac{\mathbf{v}^{\mathrm{T}}(t)\mathbf{f}'(t)}{||\mathbf{v}(t)||_2^2} & \textit{if } E_{obs}(t) = 0 \ \& \ \mathbf{v}^{\mathrm{T}}(t)\mathbf{f}'(t) < 0 \\ 0 & \textit{otherwise} \end{cases} \tag{3.19}$$

where t^- is an infinitesimal time instant before t and $|| \cdot ||_2$ is the 2-norm. By implementing a PC $z(t)\mathbf{v}(t)$, the force output $\mathbf{f}(t)$ is given by (see Fig. 3.10)

$$\mathbf{f}(t) = \mathbf{f}'(t) + z(t)\mathbf{v}(t). \tag{3.20}$$

Then, $\int_0^t \mathbf{v}^{\mathrm{T}}(\tau)\mathbf{f}(\tau)d\tau \geq 0$ is satisfied $\forall t \geq 0$. i.e. the system N is passive according to Equation (3.7) with $E(0) = 0$.

Proof. First, we consider the case when $E_{obs}(t) = 0$ (i.e. $\int_0^t \mathbf{v}^{\mathrm{T}}(\tau)\mathbf{f}(\tau)d\tau < 0$ is about to happen which violates passivity) and $\mathbf{v}^{\mathrm{T}}(t)\mathbf{f}'(t) \geq 0$. In this case we have

$$\int_0^t \mathbf{v}^{\mathrm{T}}(\tau)\mathbf{f}(\tau)d\tau = \int_0^{t^-} \mathbf{v}^{\mathrm{T}}(\tau)\mathbf{f}(\tau)d\tau + \int_{t^-}^t \mathbf{v}^{\mathrm{T}}(\tau)\mathbf{f}(\tau)d\tau$$

$$= E_{obs}(t) + \int_{t^-}^t \mathbf{v}^{\mathrm{T}}(\tau)\mathbf{f}(\tau)d\tau. \tag{3.21}$$

Since $E_{obs}(t) = 0$ and $\mathbf{v}^{\mathrm{T}}(t)\mathbf{f}'(t) \geq 0$, from (3.19) we know that $z(t) = 0$. Therefore, using (3.20), we obtain $\mathbf{v}^{\mathrm{T}}(t)\mathbf{f}(t) = \mathbf{v}^{\mathrm{T}}(t)\mathbf{f}'(t)$ which results in $\int_{t^-}^t \mathbf{v}^{\mathrm{T}}(\tau)\mathbf{f}(\tau)d\tau \geq 0$.

We now consider the case when $E_{obs}(t) = 0$ and $\mathbf{v}^{\mathrm{T}}(t)\mathbf{f}'(t) < 0$. Similarly, using the results in (3.21), we obtain $\int_0^t \mathbf{v}^{\mathrm{T}}(\tau)\mathbf{f}(\tau)d\tau = \int_{t^-}^t \mathbf{v}^{\mathrm{T}}(\tau)\mathbf{f}(\tau)d\tau$. Thus, using (3.19) and (3.20), when we

69

substitute $-\frac{\mathbf{v}^{\mathrm{T}}(t)\mathbf{f}'(t)}{||\mathbf{v}(t)||_2^2}$ for $z(t)$, we obtain

$$
\begin{aligned}
\int_{t^-}^t \mathbf{v}^{\mathrm{T}}(\tau)\mathbf{f}(\tau)d\tau &= \int_{t^-}^t \mathbf{v}^{\mathrm{T}}(\tau)\left(\mathbf{f}'(\tau) + z(\tau)\mathbf{v}(\tau)\right)d\tau \\
&= \int_{t^-}^t \mathbf{v}^{\mathrm{T}}(\tau)\left(\mathbf{f}'(\tau) - \frac{\mathbf{v}^{\mathrm{T}}(\tau)\mathbf{f}'(\tau)}{||\mathbf{v}(\tau)||_2^2}\mathbf{v}(\tau)\right)d\tau = 0,
\end{aligned}
$$

which again yields $\int_0^t \mathbf{v}^{\mathrm{T}}(\tau)\mathbf{f}(\tau)d\tau \geq 0$. Because of the continuous-time evolution of $\int_0^t \mathbf{v}^{\mathrm{T}}(\tau)\mathbf{f}(\tau)d\tau$, sudden jumps of $\int_0^t \mathbf{v}^{\mathrm{T}}(\tau)\mathbf{f}(\tau)d\tau$ from positive to negative values are not possible within (t^-, t). Thus, when $E_{obs}(t) > 0$, $\int_0^t \mathbf{v}^{\mathrm{T}}(\tau)\mathbf{f}(\tau)d\tau = E_{obs}(t) + \int_{t^-}^t \mathbf{v}^{\mathrm{T}}(\tau)\mathbf{f}(\tau)d\tau \geq 0$ without any dissipation action (i.e. $z(t) = 0$) and hence N remains passive. Notice that $z(t)$ in (3.19) is always defined since $\mathbf{v}^{\mathrm{T}}(t)\mathbf{f}'(t) < 0$ implies $\mathbf{f}'(t) \neq 0$ and $\mathbf{v}(t) \neq 0$. ■ Here we utilize the results of Theorem 4 for the port $(\mathbf{r}_s, \mathbf{f}_s)$ (as shown in Fig. 3.9) connected to B3 in Fig. 3.5.

3.7 Parameter Tuning for Transparency

By far we have guaranteed a stable trust-based mixed-initative teleoperation scheme via different passivity-based methods. However, these methods, specially the scattering transformation, require modification of velocity commands and force feedback signals in order to guarantee the stability of the overall scheme. This makes having both a stable teleoperation scheme and a transparent force feedbacks and velocity commands a challenge [46]. In the remainder of this section, we propose three different methods to improve the transparency while maintaining the stability.

3.7.1 Fine Adjustment of Scattering Transformations

Here we propose some general guidelines for utilization of passivity-based methods in the proposed scheme for a better fulfillment of transparency as well as stability. To better explain the situation, consider the scattering transformations in (3.13). Using this transformation and after some simple calculations we can obtain the following relationships between the wave variables, velocity commands and force feedback

$$
\begin{aligned}
\mathbf{u}_l &= \sqrt{2b\underline{\beta}}\,\mathbf{r}_m + \sqrt{\frac{\beta}{\underline{\beta}}}\,\mathbf{v}_l, \quad \mathbf{u}_r = \sqrt{\frac{2\alpha}{b}}\,\mathbf{f}_s - \sqrt{\frac{\alpha}{\underline{\alpha}}}\,\mathbf{v}_r, \\
\mathbf{f}_m' &= b\mathbf{r}_m + \sqrt{\frac{2b}{\underline{\beta}}}\,\mathbf{v}_l, \quad \mathbf{r}_s' = \frac{1}{b}\left(\sqrt{\frac{2b}{\underline{\alpha}}}\,\mathbf{v}_r - \mathbf{f}_s\right)
\end{aligned}
\tag{3.22}
$$

In an ideal situation, considering the inherent delay in the communication channel, we desire to achieve

$$\mathbf{f}'_m = \mathbf{v}_l, \quad \mathbf{u}_r = \mathbf{f}_s, \quad \mathbf{r}'_s = \mathbf{v}_r, \quad \mathbf{u}_l = \mathbf{r}_m, \tag{3.23}$$

such that no force feedback or velocity information is manipulated. Meanwhile, although the ideal cases in (3.23) are not achievable when using the scattering transformation to guarantee the passivity of the communication, careful choices of parameters b, $\overline{\alpha}$, $\underline{\alpha}$, $\overline{\beta}$, $\underline{\beta}$, can improve the transparency of velocity commands and force feedback values in the communication channel and hence we can obtain values for $\mathbf{f}'_m$, $\mathbf{u}_r$, $\mathbf{r}'_s$ and $\mathbf{u}_l$ that are closer to $\mathbf{v}_l$, $\mathbf{f}_s$, $\mathbf{v}_r$ and $\mathbf{r}_m$. General guidelines for achieving this goal are according to the following:

- Decreasing b and $\overline{\beta}$ and increasing $\overline{\alpha}$ makes $\mathbf{f}_s$ and $\mathbf{v}_l$ more dominant in $\mathbf{u}_r$ and $\mathbf{f}'_m$ respectively and improves the transparency of force feedback cues.

- Decreasing $\underline{\beta}$ and $\overline{\alpha}$ and increasing b makes $\mathbf{r}_m$ and $\mathbf{v}_r$ more dominant in $\mathbf{u}_l$ and $\mathbf{r}'_s$ respectively and improves the transparency of velocity commands.

Notice that achievement of both of these goals at the same time is not feasible as the adjustment of parameters towards one of the goals can have a reverse effect on the other goal. Despite this fact, applying small adjustments on several parameter can generally have a considerable total effect on the improvement of velocity command or force feedback signals.

3.7.2 Adjustment of the Feedback r-passivity Control Gains

Another fine note to have in mind is that the local passivation feedback applied to the haptic device, shown as $\mathbf{f}_{\mathrm{local}}$ in Figure 3.6, can interfere with the feeling of operator of the force feedback cue $\mathbf{f}_m$ received from the slave. This happens because the operator feels the superposition of the $\mathbf{f}_m$ and the $\mathbf{f}_{\mathrm{local}}$. Therefore, depending on the magnitudes of the force feedback cues and velocity commands in each specific mobile robot application, the passivation gain in the matrices K and B in the $\mathbf{f}_{\mathrm{local}} = -B\dot{\mathbf{x}} - K\mathbf{x}$ should not be chosen unnecessarily high. Also notice that since $\mathbf{f}'_m = b\mathbf{r}_m + \sqrt{\frac{2b}{\overline{\beta}}}\mathbf{v}_l$ contains some information about $\mathbf{r}_m = \dot{\mathbf{x}} + \Lambda\mathbf{x}$ in addition to the delayed form of the force feedback signal $\mathbf{v}_l$. Therefore, the force feedback $\mathbf{f}_m = \beta(t)\mathbf{f}'_m$ applied to the haptic device

71

contains a PD control action according to the following

$$
\begin{aligned}
\mathbf{f}_m &= \beta(t)\mathbf{f}'_m \\
&= \beta(t)\left(b\dot{\mathbf{x}} + b\Lambda\mathbf{x} + \sqrt{\frac{2b}{\overline{\beta}}}\mathbf{v}_l\right) \\
&= \beta(t)bI_p\dot{\mathbf{x}} + \beta(t)bI_p\Lambda\mathbf{x} + \beta(t)\sqrt{\frac{2b}{\overline{\beta}}}\mathbf{v}_l \\
&= B'\dot{\mathbf{x}} + K'\mathbf{x} + \beta(t)\sqrt{\frac{2b}{\overline{\beta}}}\mathbf{v}_l
\end{aligned}
\tag{3.24}
$$

where I_p is a $p \times p$ identity matrix, $B' = \beta(t)bI_p$ and $K' = \beta(t)bI_p\Lambda$. According to the Section 3.4 this extra PD control improves the passivity of the haptic device. This also has a centring effect for the haptic device because when $\dot{\mathbf{x}} = 0$ and $\mathbf{x} = 0$, we have $B'\dot{\mathbf{x}} + K'\mathbf{x} = 0$. Thus, another way to improve the effect of force feedback cue $\mathbf{f}_m$ and make it more noticeable is to decrease the feedback passivation gains b_j and k_i while still the haptic device is kept passive via the additional PD control $B'\dot{\mathbf{x}} + K'\mathbf{x}$. It is easy to show that B' causes at least $\underline{\beta}bI_p$ additional derivative control, since $\underline{\beta} \le \beta(t) \le \overline{\beta}$, and K' causes at least $\underline{\beta}bI_p\Lambda$ proportional control. Thus we can decrease the gains in the F_{local} such that the excessive local PD control is reduced and operator feels more force corresponding to $\mathbf{v}_l$ which contains force feedback cue information. However, it should be noted that $B > 0$ and $K > 0$ still should be satisfied after decreasing the control gains in these matrices such that a stable local control action is obtained.

3.7.3 Static Internal Scaling of the Force Feedback in the Master Device

Another method for improving the transparency of the force feedback is to apply a static internal scaling in the haptic device as shown in Figure 3.11. In this figure, $\mathbf{f}''_m(t) = \beta(t)\mathbf{f}'_m(t)$ is the trust-based scaled force feedback received from the communication channel and $\mathbf{f}_m(t) = \gamma\mathbf{f}''_m(t)$, where $\gamma > 0$, is the applied force to the haptic device after a static scaling with γ. This static scaling is different than $\beta(t)$ which is a dynamic scaling related to robot-to-human trust. Therefore, if we can guarantee the passivity of the haptic device for a new input vector $[\mathbf{f}_h^{\mathrm{T}} \ \mathbf{f}''^{\mathrm{T}}_m]^{\mathrm{T}}$ and position-like outputs $[\mathbf{r}''^{\mathrm{T}}_m \ \mathbf{r}_m^{\mathrm{T}}]^{\mathrm{T}}$, we can obtain a more effective haptic force feedback implementation method while still using position-like outputs for sending velocity commands to the mobile robot. This passivity property is proven in the following Proposition.
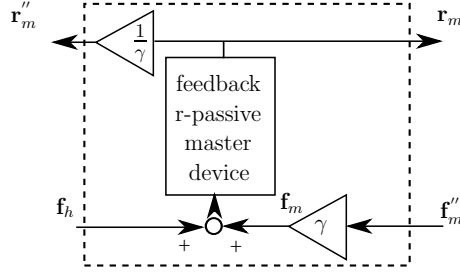
Figure 3.11: Feedback r-passivity of the master-device with static internal force scaling.

Proposition 2 *The scheme shown in Figure 3.11, is passive with the storage function $\frac{1}{\gamma}V_{hd}(t)$ defined in Equation (3.9) such that*

$$\int_0^t \mathbf{r}_m^{\mathrm{T}}(\tau)\mathbf{f}_h(\tau) + \mathbf{r}_m''^{\,\mathrm{T}}(t)\mathbf{f}_m''(\tau)d\tau = \frac{1}{\gamma}\left\{V_{hd}(t) - V_{hd}(0) + \int_0^t S_{hd}(\tau)d\tau\right\} \geq -\frac{1}{\gamma}V_{hd}(0). \qquad (3.25)$$

Proof. From the input-output ports of Figure 3.11 we obtain the following power supply

$$
\begin{aligned}
\mathbf{r}_m''^{\,\mathrm{T}}(t)\mathbf{f}_h(t) + \mathbf{r}_m^{\mathrm{T}}(t)\mathbf{f}_m''(t) &= \frac{\mathbf{r}_m^{\mathrm{T}}(t)}{\gamma}\mathbf{f}_h(t) + \mathbf{r}_m^{\mathrm{T}}(t)\frac{\mathbf{f}_m(t)}{\gamma} \\
&= \frac{1}{\gamma}\mathbf{r}_m^{\mathrm{T}}(t)(\mathbf{f}_h(t) + \mathbf{f}_m(t))
\end{aligned}
$$

which according to the Equation (3.11) indicates (3.25) and hence passivity of the master device with static internal scaling of the force feedback cues. ∎

3.8 Preliminary Case Study

In this section, we conduct a preliminary case study to examine the performance of the proposed trust-based mixed initiative teleoperation scheme. This experiment focuses on the proof of concept and a series of human subject test on a small sample size. The results of the this case study are utilized to design a more advanced experimental setup (that will follow in Section 3.9) via which we conducted a thorough study with a larger group of participants.

3.8.1 Methods

The experiment/simulation testbed is shown in Fig. 3.12. The task goal is to control the UAV to track the target UGV while maintaining a desired altitude from the target. The human operator
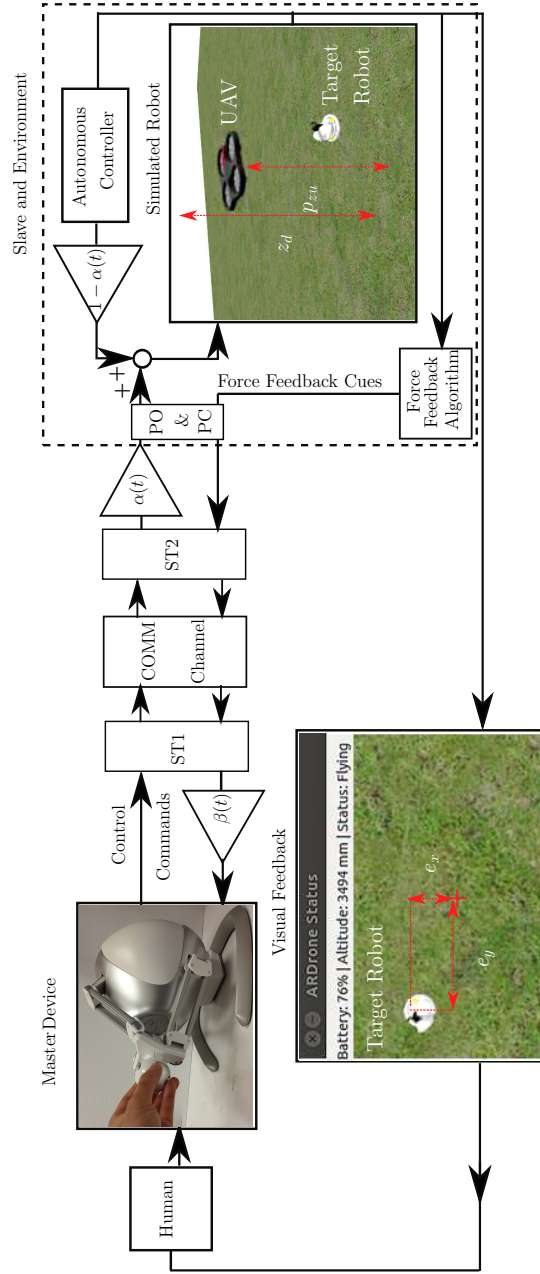
Figure 3.12: Experiment/simulation testbed: a Falcon$^{\circledR}$ (Novint) master haptic device, a A.R. Drone$^{\circledR}$ (Parrot) UAV and a Robotino$^{\circledR}$ (Festo) UGV in the Gazebo simulator [102] integrated via Robot Operating System (ROS) [105].

can control the robot manually using the master device and the visual feedback from the bottom facing camera of the UAV. The robot can also be controlled with an autonomous PID controller to hover over the target (i.e. block A_c in Fig. 3.9). Random time-varying communication delays are

implemented virtually in the simulator and will degrade the human performance in teleoperating the robot. The performance of the autonomous controller of the robot may degrade due to random sensor failures in detecting the exact position of the ground robot. Therefore, we utilize mixed-initiative teleoperation schemes to achieve a more effective control. We evaluate the human performance P_h and robot performance P_r in real-time according to the following metrics

$$P_r(t) = \frac{1}{W} \int_{t-W}^{t} p_r'(\tau)d\tau, \ P_h(t) = \frac{1}{W} \int_{t-W}^{t} p_h'(\tau)d\tau, \tag{3.26}$$

where W is the length of a moving observation window and

$$p_r'(t) = N(||\mathbf{u}_a(t) - \mathbf{u}_i(t)||_1)N((1 - \alpha(t))||\mathbf{e}(t)||_1)$$

$$p_h'(t) = N(||\mathbf{u}_h(t) - \mathbf{u}_i(t)||_1)N(\alpha(t)||\mathbf{e}(t)||_1). \tag{3.27}$$

In (3.27), $||\cdot||_1$ is the 1-norm , $N(y) = \frac{y_{\max}-y}{y_{\max}} \in [0,1]$ is a normalizing function such that $N(y_{max}) = 0$ and $N(0) = 1$, and $\mathbf{e}$ is the instantaneous position tracking error defined as

$$\mathbf{e} = [e_x \ e_y \ e_z] = [p_{xt} - p_{xu} \quad p_{yt} - p_{yu} \quad z_d - p_{zu}],$$

where $\mathbf{p}_u = [p_{xu} \ p_{yu} \ p_{zu}]$ and $\mathbf{p}_t = [p_{xt} \ p_{yt} \ p_{zt}]$ is the position of the UAV and target robot, respectively, and z_d is the desired flight altitude (see Fig. 3.15). The variables $\mathbf{u}_a$ and $\mathbf{u}_h$ are the UAV control inputs coming from the autonomous controller and the human teleoperator, respectively. Here, $\mathbf{u}_i$ is an ideal control assuming full access to the exact location and velocities of the target robot such that a good tracking performance is obtained. When evaluating $P_r(t)$ and $P_h(t)$, the weighted tracking error (weighted by the contribution of each controller, i.e. $\alpha(t)$ and $1 - \alpha(t)$) and the effectiveness of control commands compared to the ideal control commands are considered.

The parameters chosen for the experiments are according to what follows. For the passivation scheme in Fig. 3.6, $\Lambda = \text{diag}[60, 60, 60]$, $B = \text{diag}[0.55, 0.55, 0.55]$, and $K = \text{diag}[100, 100, 100]$ are chosen. In Theorem 3, we have $b = 1$ and $T_{i\,\text{max}} = 0.5$ second increase per second for $i = 1, 2$ which results in the choice of $f_i = 0.7$. The scaling parameter bounds are chosen as $\overline{\alpha} = 1$, $\underline{\alpha} = 0.05$, $\overline{\beta} = 1$ and $\underline{\beta} = 0.2$. The performance evaluation window in (3.26) is chosen to be $W = 10$ seconds. In this work, FFA in Fig. 3.9 generates a virtual spring-like feedback to guide the operator towards the target robot (i.e. $\mathbf{f}_s' = k_{ffa}\mathbf{e}$ with $k_{ffa} = 3$). We set $z_d = 4$. A fast sample time $T = 0.01s$ is

chosen such that the system dynamics remain close to continuous-time.

3.8.2   Independent and Dependent Variables

The independent variable considered in this case study is the control scheme used for controlling the UAV which includes the following five levels which are briefly denoted by the acronyms at the beginning of the decriptions

- M: Exclusively manual teleoperation with haptic force feedback cues.

- MI: mixed-initiative control without haptic feedback (MI)

- MMI: manual adjustment mixed-initiative bilateral teleoperation with haptic feedback

- TMIG: Trust-based mixed-initiative bilateral teleoperation with haptic feedback using the logistic allocation function (3.5)

- TMIS: trust-based mixed-initiative bilateral teleoperation with haptic feedback using the step allocation function in Fig. 3.3.

In the TMIG and TMIS schemes, $\alpha(t)$ and $\beta(t)$ are automatically adjusted in real-time based on the performance measures in (3.26), trust models (3.2) and (3.3), and the allocation functions in (3.5) and Fig. 3.3, respectively. In the MMI scheme, the operator is free to change $\alpha(t)$ manually according the their preference while $\beta(t) = 1 \ \forall t$. This scheme is tested to determine whether the operators prefer to do the control allocations manually or not. In the MI scheme, $\alpha(t)$ is adjusted in real-time based on the performance measures in (3.26) and Equations (3.2) and (3.5) while no force feedback is provided to the operator.

Four dependent variables (one objective and three subjective) were considered in this test. The average tracking error was used as the objective criteria determining the accuracy of accomplishing task under each level of the independent variable. This can be easily calculated from the differences in the position data of UAV and the UGV collected during the test. The subjective operator's workload was evaluated by NASA TLX [103] after each experiment. We also assessed the satisfaction of operators towards each control scheme via a post-test questionnaire with a 1-5 scale and 5 representing the highest satisfaction. The third subjective metric used in this study was the operator's trust.

Table 3.1: Comparison of the mixed-initiative teleoperation schemes over the entire set of participants.

| Control | Err(m) | | Pref | | TLX | | Trust | |
Scheme	μ	σ	μ	σ	μ	σ	μ	σ
M	3.79	2.2	3.07	0.83	54.12	17.05	4.76	1.51
MI	16.76	20.9	2.91	0.69	52.42	29.87	4.47	1.89
MMI	2.73	1.76	3.63	0.48	40.46	16.8	4.9	1.37
TMIG	2.63	1.59	3.82	0.45	30.21	16.15	5.64	1.23
TMIS	3.3	2.01	3.32	0.68	52.88	13.43	4.78	1.71

3.8.2.1 Participants

For this experiment, 8 participants (including 1 female and 7 males) between the ages of 24 and 32 took part in the study.

3.8.3 Results

The results of experiments with four criteria including the tracking error (i.e. "Err" in meters), operator satisfaction (i.e. "Sat"), task load index (i.e. "TLX"), and trust are shown in Table 3.1. This table shows the mean values (μ) and standard deviations (σ) of the mentioned criteria over the entire set of participants for each control scheme explained in Section 3.8.2. The results indicate that on average the proposed TMIG scheme leads to the smallest tracking error, lowest workload, and highest trust and satisfaction of the participants. This scheme is closely followed by the MMI scheme in which the operators were allowed to allocate control authority based on their preference. The TMIS scheme is the third best scheme in terms of tracking error and user satisfaction. However, as a result of using the step-like allocation functions in Fig. 3.3, there were sudden changes of authority and/or force feedback cues, which might have caused confusion to the participants and hence increased the perceived workload. The MI scheme exhibited the worst performance in terms of tracking error and workload because some of the participants lost the target robot and did not succeed in relocating it due to lack of force feedback cues. Compared to the M, TMIG improves the performance by 31% and reduces the workload by 23.9%. An example 3D trajectories of the UAV and the target UGV are shown in Fig. 3.13. As seen in the figure, the UAV follows a closer trajectory to the target in the TMIG scheme compared to that in the MMI scheme. The evolution of the performances $P_h(t)$ and $P_r(t)$, trust functions $T_{hr}(t)$ and $T_{rh}(t)$, as well as the allocation functions $\alpha(t)$ and $\beta(t)$ for participant 2 in TMIG are shown in Fig. 3.14. From the figure,

we can see that when $P_h(t)$ maintains a relatively high level (for example within the time frame 100-120 seconds), $T_{rh}(t)$ increases correspondingly which results in a lower level of $\beta(t)$ and hence smaller force feedback cues. Similarly, when $P_r(t)$ drops to a low level (for example within the time frame 40-60 seconds), $T_{hr}(t)$ decreases correspondingly which results in a higher level of $\alpha(t)$ and hence smaller contribution of autonomous controller.
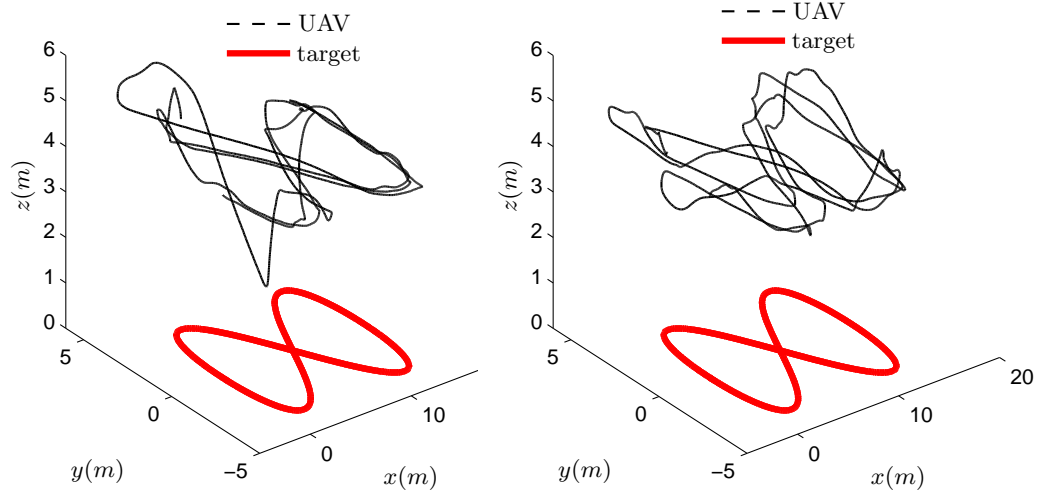

Figure 3.13: Trajectories of the target UGV and the controlled UAV in a) TMIG, and b) MMI schemes for participant 2.
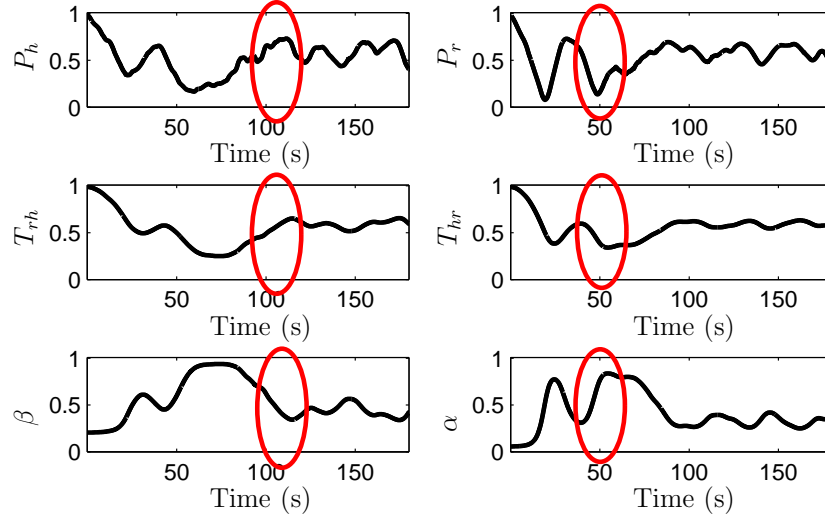
Figure 3.14: Evolution of performance, trust, and scaling parameters of participant 2 in the TMIG scheme.

78

From these preliminary results, we realized that both MI and TMIS cause noticeable confusion to the operators and hence these test conditions were dropped in the comprehensive tests included in the following section.

3.9 Main Case Study

In order to test the validity of the trust-based mixed-initiative bilateral teleoperation scheme in a more realistic way, an experimental setup was developed in the I^2R lab using real model of Parrot AR. Drone. 2.0 UAV and a Khepera III ground robot as shown in Figure 3.15. The layout of this experimental setup is shown in Figure 3.16. As it can be seen in this figure, the positions of the UAV and ground robot are tracked via a PhaseSpace tracking system camera and active markers. A server machine collets this information and communicates with a client machine which provides the operator with a user interface and also applies the control loop in Figure 3.15 in real time via ROS. In the new setup, compared to the Figure 3.12, factors such as more limited workspace of the robots, realistic disturbance applied to the UAV as well as the effect of several measurement noises on the performance of the teleoprated systems will affect the behaviour and evaluations of the operators in the proposed scheme. Thus, the results and evaluations will reveal more insight to the implementation of such schemes in the real-world applications.

The task goal and the definitions and assumptions of the performances and trust models follow the same details as in the preliminary case study in Section 3.8. Some minor changes are applied in the new experiment to match the dimensions of the UAV and the lab as well as to improve the transparency of the velocity and force singnals. For example $z_d = 1.5$ meters is chosen for this experiment. Some other fine adjustment on the experiment parameters resulted in $\Lambda = \text{diag}[10, 10, 10]$, $B = \text{diag}[5.5, 5.5, 5.5]$, $K = \text{diag}[20, 20, 20]$, $b = 2$, $\overline{\alpha} = 1$, $\underline{\alpha} = 0.2$, $\overline{\beta} = 0.5$, $\underline{\beta} = 0.05$, and $k_{ffa} = 6$. In the new set of experiments, we also included an optimal blending control for the allocation function $\alpha(t)$ according to the methods proposed in [98] in order to provide a better comparison between the control schemes. The implementation of this method is elaborated in the Appendix A. A brief description is also included in the following Section 3.9.1. Based on the initial results obtained in the previous section, we hypothesize that

a) The trust-based mixed initiative scheme will reduce the operator workload and improve the task performance compared to a manual teleoperation as well as a mixed-initiative scheme with
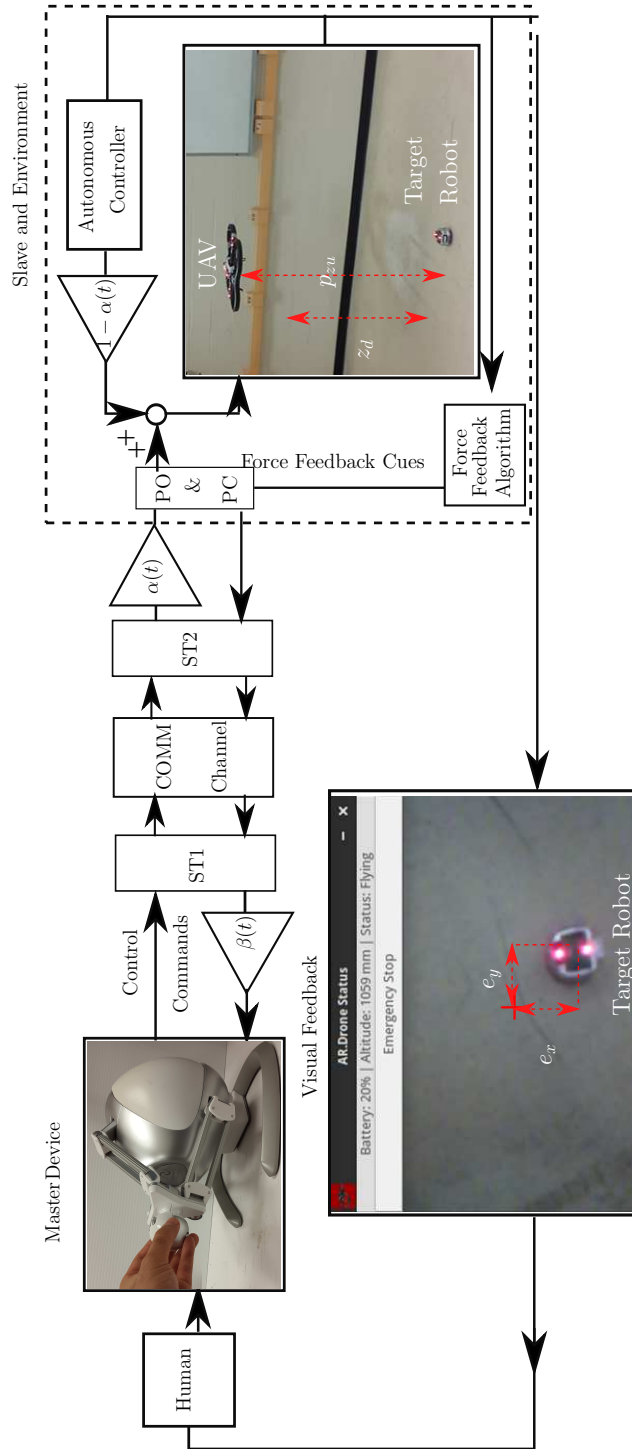
Figure 3.15: Experiment testbed: a Falcon[®] (Novint) master haptic device, a A.R. Drone[®] (Parrot) UAV and a Khepera III[®] (K-TEAM) UGV integrated via Robot Operating System (ROS).
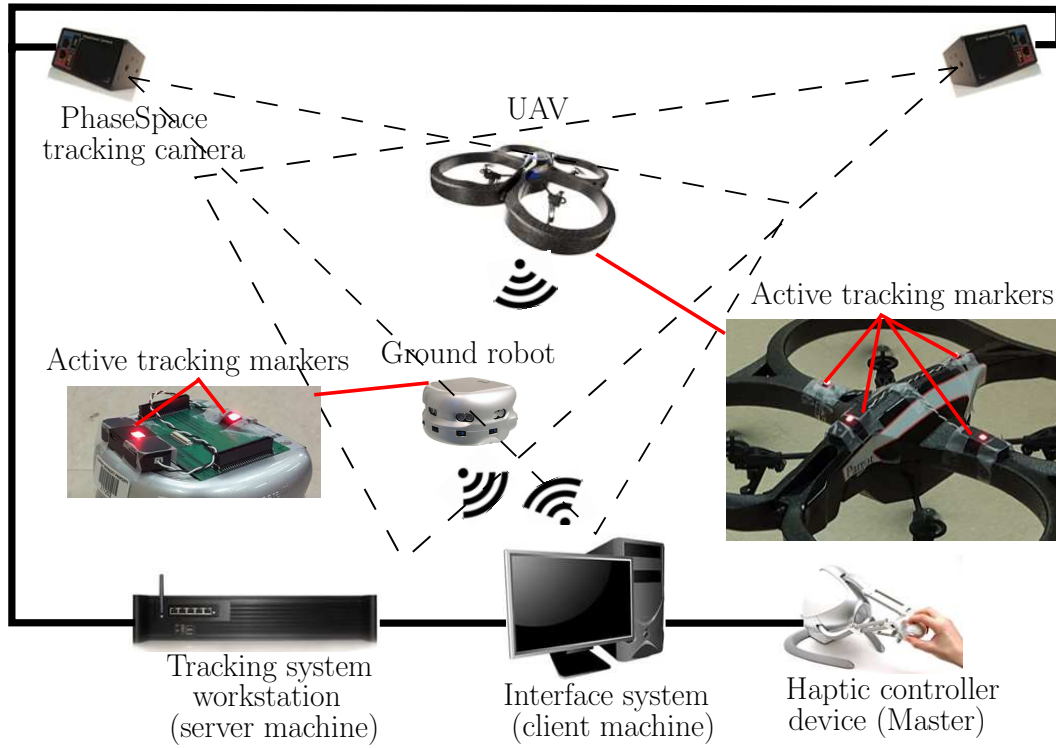
Figure 3.16: Lab layout of the testbed in Figure 3.15.

manual autonomy allocation.

b) Since the trust-based scheme is inspired by human behaviour, it will be more trusted by the operators compared to an optimal allocation method that does not follow human decision-making pattern but still can improve the task perfromance.

c) The automated trust-based decision aid scheme will be preferred to the mixed-initiative scheme with manual allocation since it performs an autonomy allocation similar to the human but with a higher efficiency.

3.9.1 Independent and Dependant Variables

Based on the pilot study, only one independent variable (IV) is considered here, i.e. the control scheme, but this time with four levels:

- M: Exclusively manual bilateral teleoperation

- OMI: Mixed-initiative bilateral teleoperation via optimal allocation method explained in Ap-

81

pendix A

- MMI: Manual adjustment mixed-initiative bilateral teleoperation with haptic feedback

- TMIG: Trust-based mixed-initiative bilateral teleoperation with haptic feedback using the logistic allocation function (3.5)

From the mentioned four levels, only OMI is new compared to the pilot study in Section 3.8. This method tries to find an optimal $\alpha(t)$ at each moment in order to minimize a cost function. This cost function considers both the tracking error and the deviations of the total control command applied to the UAV from the manual commands $\mathbf{u}_h$ [98]. We test whether this scheme is preferred by the operators in comparison to the other three methods M, MMI, and TMIG. See Appendix A for complete details. For these experiments, we utilize the same DVs from the previous case study.

3.9.2 Participants

Thirty two participants (9 female and 23 male) took part in this case study. The participants were between 22-34 years old with different occupations including student, post-doctoral fellow, medical doctor, and software engineer. The experimental data from the tests of participants 4 and 11 were dropped since they did not follow the protocol correctly.

3.9.3 Procedure

After completing the consent form and the demographic questionnaire, each participant received a 20-minute tutorial including some instructions about the task goal and controls as well as 5 minutes of practice flight with the UAV in order to learn how to control the UAV via the testbed in Figure 3.15 and the GUI in Figure 3.17. After these steps, each participant completed four tests via all of the control schemes and answered the post-test questionnaires via NASA TLX, the trust measure in [50], and the satisfaction measure in [65]. The test orders were determined via a complete balanced Latin Square design.

3.9.4 Results

A one-way repeated measures ANOVA was conducted on the four dependent variables explained in Section 3.9.1. The results are depicted in Figures 3.18-3.21 and discussed in details as

Figure 3.17: The control panel used to provide the operator with feedback about: manual control level $\alpha(t)$, UAV altitude, tracking error, and the status of the autonomous controller.

follows. In these figures, the average values and the upper and lower bounds of the 95% confidence interval are shown for each measure and test condition.

3.9.4.1 Tracking Error
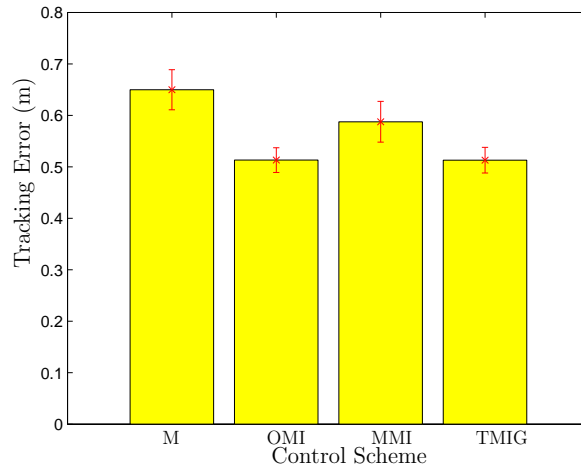
Figure 3.18: Comparison of the control schemes via average tracking error.

For the average tracking error during the task, the assumption of sphericity was violated as assessed by the Mauchly's test of sphericity and hence a Greenhouse-Geisser correction was applied

($\epsilon = 0.812$). Moreover, a winsorizing was applied to the TMIG data to reduce the effect of two outliers. A significant difference was observed between the control schemes, $F(2.425, 70.628) = 33.235$, $p < 0.0005$ and $\eta^2 = 0.534$. The pairwise comparison indicates that the tracking error significantly decreases from condition M ($M = 0.649, SD = 0.104$) meters to the conditions OMI ($M = 0.513, SD = 0.064$), $p < 0.0005$, MMI ($M = 0.588, SD = 0.107$), $p = 0.018$, and TMIG ($M = 0.51, SD = 0.058$), $p < 0.0005$ (see Figure 3.18). Moreover, the MMI condition results in a significantly higher error than the conditions OMI, $p = 0.002$ and TMIG, $p = 0.002$. These results indicate that the automated shared control schemes OMI and TMIG can improve the tracking accuracy compared to an exclusively manual scheme (M) and the mixed-initiative scheme with manual allocation (MMI).

3.9.4.2 Task Load Index (TLX)
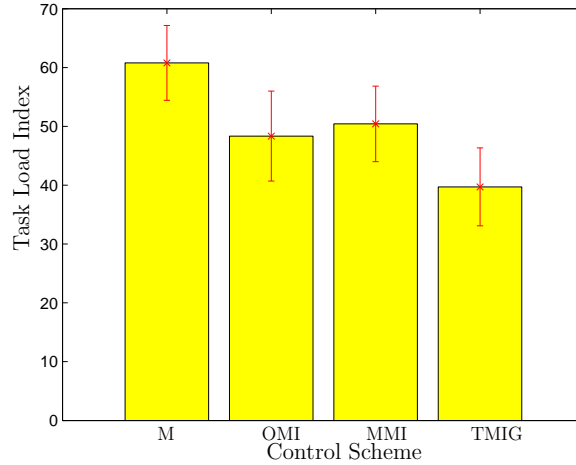
Figure 3.19: Comparison of the control schemes via task load index.

As assessed by the Mauchly's test, the assumption of sphericity was met $\chi^2(5) = 5.14$, $p = 0.399$ and the task load significantly differed among the control schemes, $F(3, 87) = 9.465$, $p < 0.0005$ and $\eta^2 = 0.246$. The results indicate that the workload in the TMIG ($M = 39.71, SD = 17.76$) is significantly lower than the conditions M ($M = 60.78, SD = 17.03$), $p < 0.0005$, and MMI ($M = 50.42, SD = 17.20$), $p = 0.012$. Also, the scheme OMI ($M = 48.34, SD = 20.45$) significantly decreases the workload of the operator compared to the M, $p = 0.027$. In other cases, no significant differences were observed (see Figure 3.19). This proves that the human-like TMIG scheme can

reduce the decision-making workload of the operator compared to a manual autonomy allocation scheme in MMI.

3.9.4.3 Satisfaction
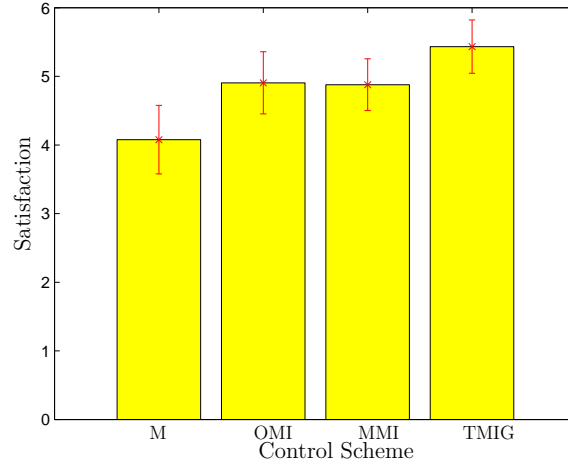
Figure 3.20: Comparison of the control schemes via satisfaction.

For this measure, the assumption of sphericity was met as evaluated by Mauchly's test, $\chi^2(5) = 5.14$, $p = 0.399$. A significant difference between the satisfaction of operators among the four control schemes was observed, $F(3, 87) = 11.82$, $p < 0.0005$ and $\eta^2 = 0.29$. The pairwise comparisons show that the condition M ($M = 4.08, SD = 1.34$) is the least preferred control scheme compared to the OMI ($M = 4.91, SD = 1.22$), $p = 0.014$, MMI ($M = 4.88, SD = 1.01$), $p = 0.022$, and TMIG ($M = 5.43, SD = 1.01$), $p < 0.005$. Furthermore, the results indicated that the TMIG is preferred to the MMI, $p = 0.041$ (see Figure 3.20).

3.9.4.4 Trust

For the score of trust, Mauchly's test of sphericity indicates that the assumption of sphericity was met, $\chi^2(5) = 7.785$, $p = 0.169$. The trust scores were significantly different among the test conditions $F(3, 87) = 9.581$, $p < 0.0005$, and $\eta^2 = 0.248$. The control scheme TMIG($M = 5.675, SD = 0.779$) was significantly more trusted than the schemes M ($M = 4.550, SD = 1.171$), $p = 0.001$, and OMI($M = 4.969, SD = 1.153$), $p = 0.036$. Moreover, the MMI($M = 5.261, SD = 0.974$) scheme is more trusted than M, $p = 0.027$ (see Figure 3.21). This indicates that the TMIG is trusted as much
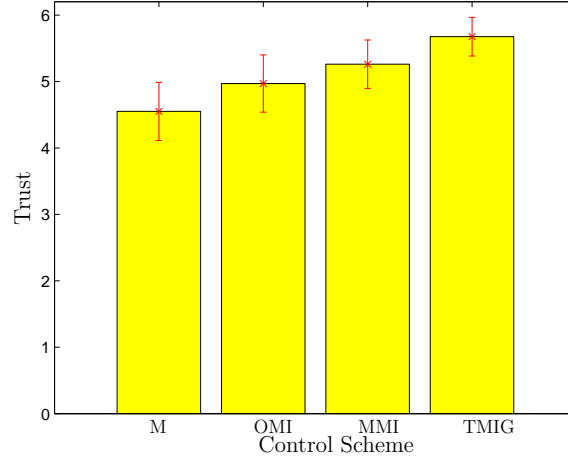
Figure 3.21: Comparison of the control schemes via trust.

as the manual autonomy allocation scheme MMI.

3.9.5 Discussion
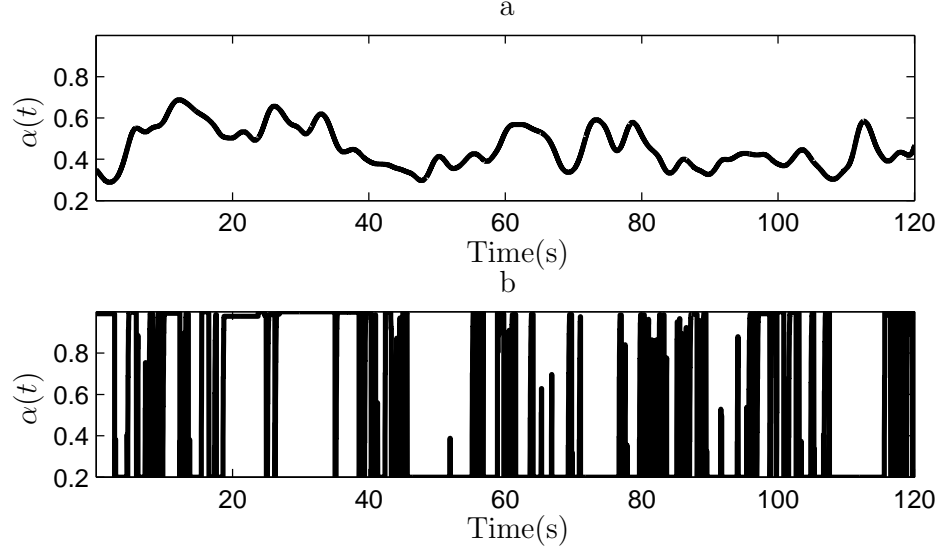
Figure 3.22: Comparison of the allocation function $\alpha(t)$ in: a) TMIG, and b) OMI control schemes for participant no. 20.

From the results, we observed a 12.76% reduction of tracking error in the TMIG and OMI compared to the MMI. The higher tracking error in the MMI condition may be the result of multi-

tasking of operator which needs to keep track of several real-time measures as well as the control of UAV. Moreover, TMIG scheme reduced the task load index by 10.71% compared to MMI which again may be related to the multi-tasking of the operator in the latter method (hypothesis (a)). This reduced workload as well as the better tracking performance of TMIG results in higher satisfaction of operators towards this scheme compared to the MMI (hypothesis (c)). Finally, we observed that even when the tracking performances of the TMIG and OMI schemes are close to each other, TMIG is more trusted by the operators (hypothesis (b)). The reason behind higher trust of operators to TMIG compared to the OMI is that in the OMI method, the allocation function $\alpha(t)$ changes rapidly in order to minimize the tracking error. However, in the TMIG method, according to several comments from the operators, the pattern of change of $\alpha(t)$ is much closer to the human. Figure 3.22 shows an example of the comparison between the control allocation methods in TMIG and OMI.

3.10   Conclusion

In this chapter, we developed a trust-based mixed-initiative teleoperation scheme for mobile robotic systems. We utilized computational two-way models of trust in the proposed scheme to mediate the human and autonomous control initiatives as well the force feedback cues with variable scales. We utilized passivity techniques to guarantee the overall passivity of the proposed scheme in the presence of variable power scaling and time-varying delays. We also experimentally tested the effectiveness of the trust-based mixed-initiative teleoperation scheme. The proposed scheme resulted in a higher task performance and operator satisfaction, as well as lower workload compared to exclusively manual teleoperation, and mixed-initiative control with manual allocation of autonomy. The proposed method was also more trusted compared to the optimal control method with same performance because the former follows a human-like decision-making pattern.

Chapter 4

Trust-Based Bilateral Teleoperation of Multi-Robot Systems

4.1 Introduction

In the previous chapters, we utilized computational models to obtain an objective, performance-centric evaluation of human trust in robot in order to provide decision aids for control allocation of robots [85, 86]. The results indicated improved task performance while the automated decision-making method remains close to human decision-making pattern and hence yielded higher acceptance. In this chapter, we extend the results of Chapter 3 to the single-operator-multiple-robot systems. In such systems, by having a human controlling a team of robots, the manpower required for accomplishing tasks can be reduced [27]. These systems also benefit from robustness and flexibility as a result of having several team members. Examples of multiple-robot systems include coordination and cooperation between robots and humans in applications such as domain search [109], manipulation of objects [59], and surveillance [27].

As the first contribution of this chapter, in Section 4.3, we extend our previous work to the multi-robot case with applications in collective position tracking and synchronization under a novel trust-based leader switching bilateral teleoperation scheme. It has been shown that in such

applications, proper choice of leader as well as online leader selection can improve the manipulability and the overall tracking performance of the robot team [33] [92]. In this chapter, human-to-robot trust will be used in order to select a new leader to be controlled by human within a specific time period. The force feedback cues, applied in the bilateral teleoperation schemes for improved performance, will be scaled with a variable scale as a function of robot-to-human trust to assist the operator with various levels of feedback and reduce the physical workload.

The proposed scheme introduces trust-based switches, when choosing a new leader, as well as variable scaling to the conventional bilateral teleoperation system. These can cause instabilities in the overall system. Therefore, as the second contribution of this chapter, we perform passivity analysis for the proposed scheme and guarantee the stability of the entire system under the effects of delay as well as trust-based switching and variable scaling. We also provide passive smooth filtering of the discontinuities in the velocity and force feedback signals while maintaining the passivity and stability of the entire system (See Section 4.7). These discontinuities arise due to switching between different leaders. As our third contribution, in Section 4.8, we prove a good collective position tracking and synchronization performance of the multi-robot system under the guidance of a leader robot teleoperated by human within the developed scheme with the aid of vision feedback.

4.2 Notation

Consider a team of N robots connected with an undirected graph $G_s = (\mathcal{V}, \mathcal{E})$, $\mathcal{E} \subseteq \mathcal{V} \times \mathcal{V}$ where $\mathcal{V}$ and $\mathcal{E}$ are the set of vertices and edges, respectively. For this graph, the adjacency matrix $A_{N \times N}$ defines the set of neighbors of the robot i (denoted as $\mathcal{N}_i = \{v_j \in \mathcal{V} | (v_i, v_j) \in \mathcal{E}\}$ such that we have,

$$a_{ij} = \begin{cases} 1 & \text{if } (v_i, v_j) \in \mathcal{E} \\ 0 & \text{if } (v_i, v_j) \notin \mathcal{E} \end{cases}.$$

The graph Laplacian matrix $L_{N \times N}$ is given by $L = D - A$ where $D_{N \times N}$ is the degree matrix of G_s.

Assume that for this team, the leader robot is switched according to the following pattern. Denote a robot $i_k \in \{1, 2, \cdots, N\}$ in the multi-robot team, with the subscript $k \in \{0, 1, \cdots, S\}$ where S is the total number of leader switches in $[0, t]$. The index i_k refers to the leader robot controlled after the kth switch occurs. That is, robot i_k is manually controlled within the time
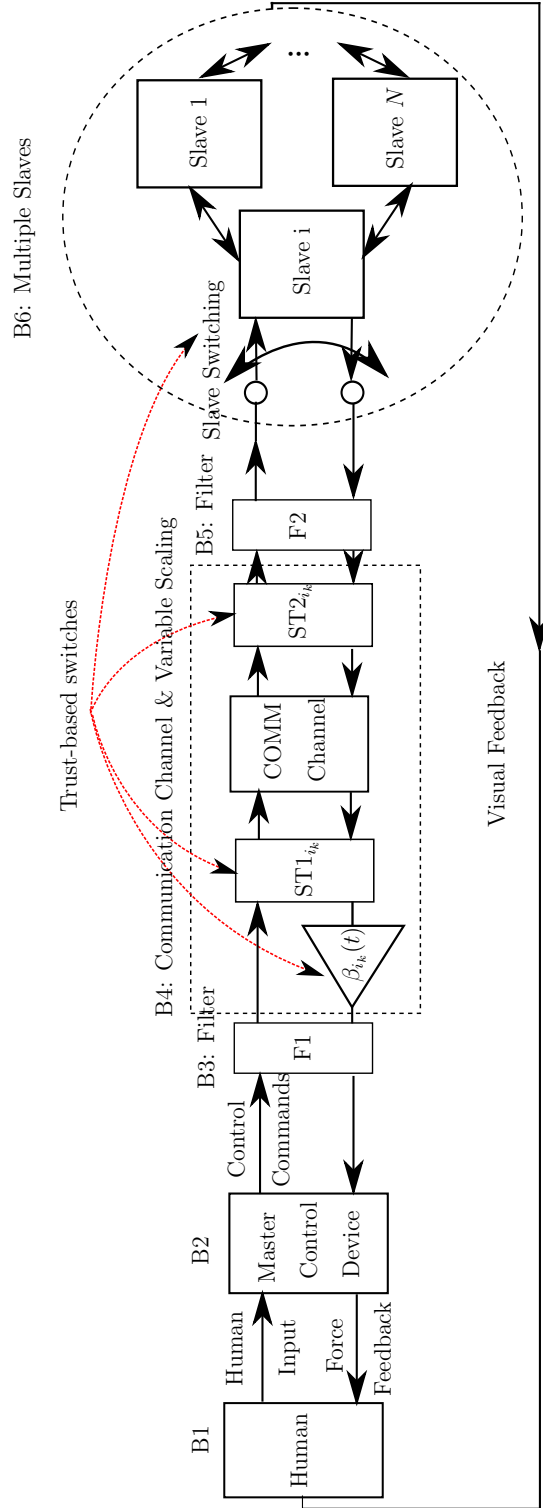
Figure 4.1: Block diagram for the trust-based bilateral teleoperation of multi-robot team.

period $t \in (t_k, t_{k+1}]$. For example, i_k with $i = 5$ and $k = 3$ means that the robot/slave 5 is chosen as the leader at the 3rd leader switch. Notice that $i_k \in \{1, 2, \cdots, N\} \setminus i_{k-1}$ must always be satisfied. This guarantees that a new robot will be controlled after each switch. Without loss of generality we can consider $t_0 = 0$ and the operator is initially controlling robot i_0. Notice that generally $t_k - t_{k-1} \neq t_{k+1} - t_k$, which means the switchings are not periodic and do not follow any regular time-based pattern. We further assume that for the communication delay T between a human operator and a leader robot, we have $t_{k+1} - t_k \geq \tau_{min} \gg T$ with τ_{min} the minimum time that the operator needs to spend controlling a robot. Notice that τ_{min} is considerably larger than the communication delay T ($T \leq 1.5$ seconds for robotic applications on earth). The assumption is made since we do not want too frequent switches between robots due to human reaction limits.

4.3 Trust-Based Bilateral Teleoperation of Multi-Robot Systems

In this section, we present a trust-based bilateral teleoperation scheme for mobile multi-robot systems as shown in Figure 4.1. The major subsystems of this scheme include a master control device (block B2 detailed in Section 4.5) for sending the control commands of human (block B1) and applying force feedback cues, a communication channel including the variable scale $\beta_{i_k}(t)$ (B4 detailed in Section 4.6), two smoothing low-pass filters $F1$ and $F2$ (B3 and B5 detailed in Section 4.7), and a slave system including a leader robot and some follower robots (B6 detailed in Section 4.8). The scheme in Figure 4.1 is developed in a way to make it suitable for multiple robot applications such as platooning or shared formation control [34] according to what follows.

Human factors research shows that trust is dynamic and highly dependent on performance [62]. Based on these performance-centric measures, the models of human-to-robot trust $T_{hr_i}(t)$ and robot-to-human trust $T_{rh_i}(t)$ evolve according to the following

$$\dot{T}_{hr_i}(t) = f_{hr_i}(T_{hr_i}(t), P_{r_i}(t)) \tag{4.1}$$

$$\dot{T}_{rh_i}(t) = f_{rh_i}(T_{rh_i}(t), P_h(t)) \tag{4.2}$$

where $i \in \{1, 2, \cdots, N\}$ determines a specific robot in the team consisting of N robots regardless of which leader is currently selected, $P_h(t)$ is the human performance, and $P_{r_i}(t)$ is the perfor-

mance of robot i. Notice that $T_{hr_i}(t)$ are latent and usually difficult to model and measure precisely. In Chapters 2 and 3, we utilized computational variations of (4.1) to obtain an objective, performance-centric evaluation of human trust in robot in order to provide decision aids for robot control allocation. Similarly, in this chapter, we build a theoretical framework to enable a trust-based leader switched multi-robot teleoperation scheme as shown in Figure 4.1 and guarantee its stability as well as good performance[1]. The computational robot-to-human trust model (4.2) provides an opportunity to apply a variable trust-based scaling of the force feedback cues applied to the operator. The trust models (4.1) and (4.2) can be adjusted such that, when both $P_{r_i}(t)$ and $P_h(t)$ are bounded, i.e. $P_{r_i}(t) \in [\underline{P}_{r_i}, \overline{P}_{r_i}]$ and $P_h(t) \in [\underline{P}_h, \overline{P}_h]$, $T_{hr_i}(t)$ and $T_{rh_i(t)}$ are bounded as well, i.e. $\underline{T}_{hr_i} \le T_{hr_i}(t) \le \overline{T}_{hr_i}$ and $\underline{T}_{rh_i} \le T_{rh_i}(t) \le \overline{T}_{rh_i}$ which represent acceptable trust ranges in order to avoid either over-reliance or under-reliance of human on the robot and vice versa.

It has been shown that online leader selection can improve the task performance of team of robots [33]. In the proposed trust-based bilateral teleoperation control scheme for multiple robots shown in Figure 4.1, human-to-robot trust $T_{hr_i}(t)$ will be used to determine which specific leader robot should be controlled by human within a specific time period while other robots are controlled purely by local in-situ autonomous controllers. That is, each follower robot is controlled via a local autonomous controller while the leader receives human control commands in addition to the local autonomous control commands (See Equation (4.19) introduced later in Section 4.8 as an example). This entailment of a novel trust-based switched bilateral scheme for the interaction of operator with a team of robots is the main difference between this chapter and Chapter 3. This requires nontrivial extensions for guaranteed passivity and hence stability of the operation. One example of trust-based leader switching policies can be always collaborating with the most trusted robot in order to improve the overall task performance, i.e.

$$
i := \begin{cases} \text{leader} & \text{if } T_{hr_i}(t) = \max_i(T_{hr_i}(t)) \\ \text{follower} & \text{otherwise} \end{cases} .
$$

We utilize robot-to-human trust $T_{rh_i}(t)$ as a metric to scale the force feedback cues such that whenever robot i is the leader and hence teleoperated by the operator, the force feedback cues will be scaled with a variable scale $\beta_{i_k}(t)$, depending on the trust of the current leader to human,

---

[1]Future study can consider developing robot experiments with human-in-the-loop similar to [85] and [86] as well as investigating different models for $T_{hr_i}(t)$.

to assist the operator with various levels of force feedback. Here, we define the trust-based variable scaling parameter $\beta_{i_k}(t)$ (i.e. variable trust-based scale of robot i chosen as the teleoperated leader in the time period $(t_k, t_{k+1}]$) in the following range:

$$0 < \underline{\beta}_{i_k} \leq \beta_{i_k}(t) \leq \overline{\beta}_{i_k}, \tag{4.3}$$

where the positive constants $\underline{\beta}_{i_k}, \overline{\beta}_{i_k}$ are choices that determine the lower and upper bounds on $\beta_{i_k}(t)$ for a specific task requirement. See [85] for examples of smooth and non-smooth trust-based scaling functions for $\beta_{i_k}(t) = g_{rh_i}(T_{rh_i}(t))$. These functions provide a mapping such that, at lower values of robot-to-human trust, $\beta_{i_k}(t)$ takes higher values which applies larger force feedback cues to the human for performance improvement and vice versa with extreme cases being $g_{rh_i}(\overline{T}_{rh_i}) \to \underline{\beta}_{i_k}$ and $g_{rh_i}(\underline{T}_{rh_i}) \to \overline{\beta}_{i_k}$. These computational models for trust and the scaling variables are based on the nonlinear model obtained experimentally in [38].

However, utilization of such a scheme requires switches between different configurations of scattering transformations $ST1_{i_k}$ and $ST2_{i_k}$, variable scaling $\beta_{i_k}(t)$, and slave robots when a new leader is chosen (Figure 4.1). As a result of the switching, passivity of the trust-based teleoperation scheme may be violated [118]. If left untreated, this can lead to instability issues which are undesirable effects of switching. Thus, in the remaining parts of this chapter we develop theoretical methods in order to guarantee a passive and hence stable trust-based switched bilateral teleoperation.

4.4 Passivity Definition

In the following, we summarize different passivity definitions utilized in the next sections to guarantee the passivity of the overall switched bilateral teleoperation scheme in Figure 4.1.

Definition 3 *[118] For systems with discontinuous supply rate (as shown in Figure 4.2), and/or switched inputs/outputs with a common storage function, the following variation of (3.7) must hold*

$$\sum_{k=0}^{S-1} \left\{ \int_{t_k^+}^{t_{k+1}} \mathbf{y}_k^{\mathrm{T}}(\tau)\mathbf{u}_k(\tau)d\tau \right\} + \int_{t_S^+}^{t} \mathbf{y}_S^{\mathrm{T}}(\tau)\mathbf{u}_S(\tau)d\tau + V(0) \geq 0, \tag{4.4}$$

where t_ks are the time instants that discontinuities in the inputs and outputs or a switching of the system input and output occur according to the notation in Section 4.2, $\mathbf{u}_k$ and $\mathbf{y}_k$ are piecewise

93

continuous input and outputs between the discontinuities or switches (i.e. in $(t_k, t_{k+1}]$ as shown in Figure 4.2), and $V(t) \geq 0$ is a common storage function between the modes. We assume that the states of that the system do not jump at the switching events and remain continuous. This is reasonable because the systems do not undergo any impulsive effects. Without loss of generality we consider $t_0 = 0$.
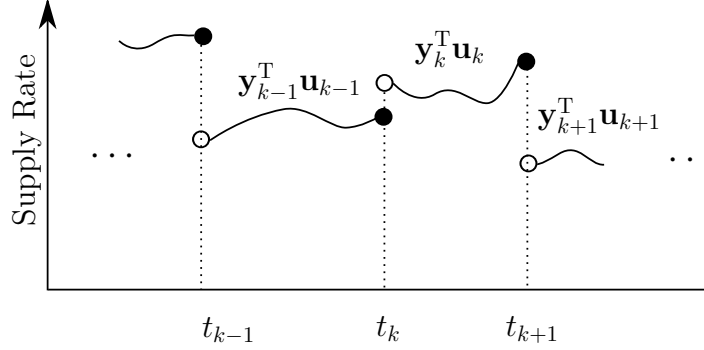
Figure 4.2: Discontinuous/switched supply rate.

The bilateral teleoperation scheme shown in Figure 4.1 includes several components interacting thorough force and velocity power variables [73]. Utilizing a mechanical/electrical analogy, these components can be modeled as one-port and two-port components networks shown in Figure 4.3. Under this port-based representation, the passivity inequalities (3.7) and (4.4) must hold for the summation of power supplied by each port. It is widely known that cascade interconnection of passive one-port and/or two-port system is still passive [73]. If each individual block in Figure 4.1 is passive (to be shown in the subsequent sections), the entire scheme is passive and hence stable.

Definition 4 *Let $V(t)$ represent the energy stored in the communication channel with a scheme shown in Figure 4.4. Also consider $\hat{\mathbf{r}}_m, \hat{\mathbf{f}}_m, \hat{\mathbf{r}}_s, \hat{\mathbf{f}}_s$ as the power variables of this channel with their piecewise continuous form denoted as $\hat{\mathbf{r}}_{m_{i_k}}, \hat{\mathbf{f}}_{m_{i_k}}, \hat{\mathbf{r}}_{s_{i_k}}, \hat{\mathbf{f}}_{s_{i_k}}$ in any $t \in (t_k, t_{k+1}]$ when robot i is the leader. Utilizing the two-port network equivalent of this channel shown as B4 in Figure 4.3, the passivity inequality (4.4) in Definition 3, and assuming that no energy is initially stored, i.e. $V(0) = 0$, the communication channel is passive if*

$$\sum_{k=0}^{S-1} \left\{ \int_{t_k^+}^{t_{k+1}} (\hat{\mathbf{r}}_{m_{i_k}}^{\mathrm{T}}(\tau)\hat{\mathbf{f}}_{m_{i_k}}(\tau) - \hat{\mathbf{r}}_{s_{i_k}}^{\mathrm{T}}(\tau)\hat{\mathbf{f}}_{s_{i_k}}(\tau))d\tau \right\} + \int_{t_S^+}^{t} (\hat{\mathbf{r}}_{m_{i_S}}^{\mathrm{T}}(\tau)\hat{\mathbf{f}}_{m_{i_S}}(\tau) - \hat{\mathbf{r}}_{s_{i_S}}^{\mathrm{T}}(\tau)\hat{\mathbf{f}}_{s_{i_S}}(\tau))d\tau \geq 0. (4.5)$$
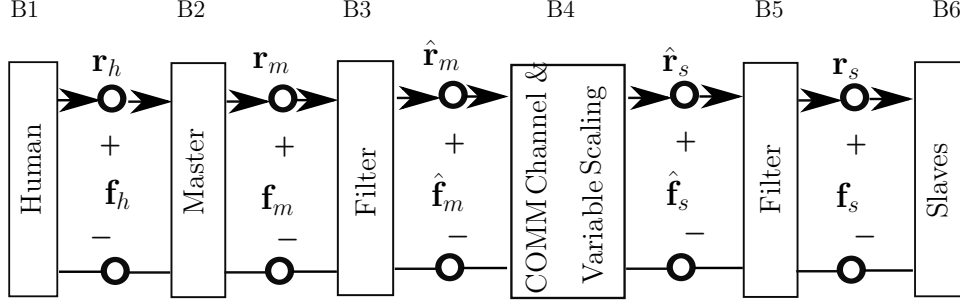
Figure 4.3: Port-based model the Figure 4.1.

4.5 The Haptic Feedback Controller Device

The passivation technique for the haptic device used in Section 3.4 holds for the applications in this chapter as well. Therefore, we use $\mathbf{r}_m$ as the output of the haptic device for sending velocity commands to the leader robot. This results in a passive two-port model shown as B2 in Figure 4.3 with the following closed loop dynamics

$$M(\mathbf{x}_m)\ddot{\mathbf{x}}_m + C(\mathbf{x}_m, \dot{\mathbf{x}}_m)\dot{\mathbf{x}}_m + B\dot{\mathbf{x}}_m + K\mathbf{x}_m = \mathbf{f}_h - \mathbf{f}_m, \tag{4.6}$$

with the same descriptions about the parameters as in Section 3.4. For dynamics (4.6), $\mathbf{f}_h - \mathbf{f}_m$ is the passive input force, $\mathbf{r}_m = \dot{\mathbf{x}}_m + \Lambda\mathbf{x}_m$ is the passive position-like output, and the $V_{hd}(t)$ in (3.9) is storage function and hence the passivity condition holds for the B2 block such that $\int_0^t \mathbf{r}_m^{\mathrm{T}}(\tau)(\mathbf{f}_h(\tau) - \mathbf{f}_m(\tau))d\tau \geq -V_{hd}(0)$. For the proof see [60]. Notice that since the operator is holding the end effector of the haptic device in hand, it follows that $\mathbf{r}_h = \mathbf{r}_m$.

4.6 Communication Channel with Variable Power Scaling

In this section, we develop a method using switched wave/scattering transformations in order to guarantee the passivity of the communication channel (block B4 in Figure 4.3) in the presence of communication delay T, variable robot-to-human trust-based scaling $\beta_{i_k}(t)$, and human-to-robot trust-based leader switches (detailed in Section 4.3) as shown in Figure 4.4. In this figure, $\hat{\mathbf{f}}_s$ is the force feedback cue sent from the current leader, $\hat{\mathbf{f}}'_m$ is the force feedback received from the communication channel with its scaled forms being $\hat{\mathbf{f}}_m$, $\hat{\mathbf{r}}_m$ is the velocity command sent by human via haptic device, $\hat{\mathbf{r}}_s$ is the velocity command received from the communication channel, and $\mathbf{u}_r$, $\mathbf{u}_l$, $\mathbf{v}_r$, $\mathbf{v}_l$ are some wave variables (to be defined in Theorem 5). As mentioned in Definition 4,

95

$\hat{\mathbf{r}}_{m_{i_k}}, \hat{\mathbf{f}}_{m_{i_k}}, \hat{\mathbf{r}}_{s_{i_k}}, \hat{\mathbf{f}}_{s_{i_k}}$ denoted the piecewise continuous form of $\hat{\mathbf{r}}_m, \hat{\mathbf{f}}_m, \hat{\mathbf{r}}_s, \hat{\mathbf{f}}_s$ in any $t \in (t_k, t_{k+1}]$ when robot i is leader.
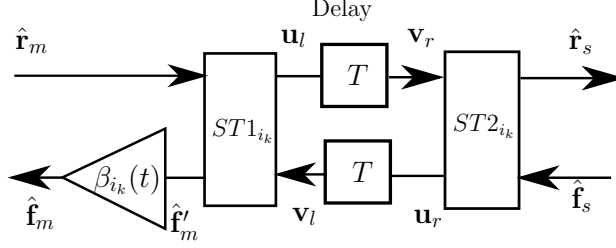
Figure 4.4: The internal block diagram of block B4 in Figure 4.3.

Theorem 5 *Choose the scattering transformation $ST1_{i_k}$ and $ST2_{i_k}$ according to the following*

$$\mathbf{u}_l = \sqrt{\frac{\underline{\beta}_{i_k}}{2b_{i_k}}}(\hat{\mathbf{f}}'_{m_{i_k}} + b_{i_k}\hat{\mathbf{r}}_{m_{i_k}}), \quad \mathbf{v}_l = \sqrt{\frac{\overline{\beta}_{i_k}}{2b_{i_k}}}(\hat{\mathbf{f}}'_{m_{i_k}} - b_{i_k}\hat{\mathbf{r}}_{m_{i_k}}),$$

$$\mathbf{u}_r = \sqrt{\frac{1}{2b_{i_k}}}(\hat{\mathbf{f}}_{s_{i_k}} - b_{i_k}\hat{\mathbf{r}}_{s_{i_k}}), \quad \mathbf{v}_r = \sqrt{\frac{1}{2b_{i_k}}}(\hat{\mathbf{f}}_{s_{i_k}} + b_{i_k}\hat{\mathbf{r}}_{s_{i_k}}) \tag{4.7}$$

with $\underline{\beta}_{i_k}$ and $\overline{\beta}_{i_k}$ defined as in (4.3) and $b_{i_k} > 0$ is the channel impedence. The communication channel is passive in the sense of Definition 4. That is, the passivity inequality (4.5) holds.

Proof. For any time period $(t_k, t_{k+1}]$, using the scattering transformations in (4.7) we obtain

$$\hat{\mathbf{r}}^{\mathrm{T}}_{m_{i_k}}(t)\beta_{i_k}(t)\hat{\mathbf{f}}'_{m_{i_k}}(t) = \frac{\beta_{i_k}(t)}{2}\left[\frac{\mathbf{u}_l^{\mathrm{T}}(t)\mathbf{u}_l(t)}{\underline{\beta}_{i_k}} - \frac{\mathbf{v}_l^{\mathrm{T}}(t)\mathbf{v}_l(t)}{\overline{\beta}_{i_k}}\right]$$

$$\hat{\mathbf{r}}^{\mathrm{T}}_{s_{i_k}}(t)\hat{\mathbf{f}}_{s_{i_k}}(t) = \frac{1}{2}[\mathbf{v}_r^{\mathrm{T}}(t)\mathbf{v}_r(t) - \mathbf{u}_r^{\mathrm{T}}(t)\mathbf{u}_r(t)]. \tag{4.8}$$

Therefore, using (4.8), for any $k \in \{0, \cdots, S-1\}$, the integral inside the summation term in (4.5) can be written as follows

$$\int_{t_k^+}^{t_{k+1}}(\hat{\mathbf{r}}^{\mathrm{T}}_{m_{i_k}}(\tau)\hat{\mathbf{f}}_{m_{i_k}}(\tau) - \hat{\mathbf{r}}^{\mathrm{T}}_{s_{i_k}}(\tau)\hat{\mathbf{f}}_{s_{i_k}}(\tau))d\tau = \int_{t_k^+}^{t_{k+1}}\frac{\beta_{i_k}(\tau)}{2}\left[\frac{\mathbf{u}_l^{\mathrm{T}}(\tau)\mathbf{u}_l(\tau)}{\underline{\beta}_{i_k}} - \frac{\mathbf{v}_l^{\mathrm{T}}(\tau)\mathbf{v}_l(\tau)}{\overline{\beta}_{i_k}}\right]$$

$$-\frac{1}{2}[\mathbf{v}_r^{\mathrm{T}}(\tau)\mathbf{v}_r(\tau) - \mathbf{u}_r^{\mathrm{T}}(\tau)\mathbf{u}_r(\tau)]d\tau. \tag{4.9}$$

Since we have $\mathbf{v}_r(t) = \mathbf{u}_l(t - T)$, $\mathbf{v}_l(t) = \mathbf{u}_r(t - T)$, and $0 < \underline{\beta}_{i_k} \leq \beta_{i_k}(t) \leq \overline{\beta}_{i_k}$, we can show that the integral in (4.9) is lower bounded by

$$\text{Eqn. (4.9)} \geq \frac{1}{2} \int_{t_k^+}^{t_{k+1}} [\mathbf{u}_l^{\mathrm{T}}(\tau)\mathbf{u}_l(\tau) - \mathbf{u}_l^{\mathrm{T}}(\tau - T)\mathbf{u}_l(\tau - T)$$
$$+ \mathbf{u}_r^{\mathrm{T}}(\tau)\mathbf{u}_r(\tau) - \mathbf{u}_r^{\mathrm{T}}(\tau - T)\mathbf{u}_r(\tau - T)]d\tau. \tag{4.10}$$

Using a simple change of variables and given that $t_{k+1} - t_k \gg T$, we can break the integral $\int_{t_k^+}^{t_{k+1}} \mathbf{u}_l^{\mathrm{T}}(\tau - T)\mathbf{u}_l(\tau - T)d\tau$ as

$$\int_{t_k^+}^{t_{k+1}} \mathbf{u}_l^{\mathrm{T}}(\tau - T)\mathbf{u}_l(\tau - T)d\tau = \int_{t_k^+ - T}^{t_k} \mathbf{u}_l^{\mathrm{T}}(\tau)\mathbf{u}_l(\tau)d\tau + \int_{t_k^+}^{t_{k+1} - T} \mathbf{u}_l^{\mathrm{T}}(\tau)\mathbf{u}_l(\tau)d\tau. \tag{4.11}$$

Moreover, since switches are apart from each other such that $t_{k+1} - t_k \gg T$, no discontinuity is observed at $t_k^+ - T$ and hence $\int_{t_k - T}^{t_k^+ - T} \mathbf{u}_l^{\mathrm{T}}(\tau)\mathbf{u}_l(\tau)d\tau \to 0$. Therefore (4.11) is equal to

$$\int_{t_k - T}^{t_k} \mathbf{u}_l^{\mathrm{T}}(\tau)\mathbf{u}_l(\tau)d\tau + \int_{t_k^+}^{t_{k+1} - T} \mathbf{u}_l^{\mathrm{T}}(\tau)\mathbf{u}_l(\tau)d\tau. \tag{4.12}$$

Using the results in (4.11) and (4.12), we obtain

$$\int_{t_k^+}^{t_{k+1}} [\mathbf{u}_l^{\mathrm{T}}(\tau)\mathbf{u}_l(\tau) - \mathbf{u}_l^{\mathrm{T}}(\tau - T)\mathbf{u}_l(\tau - T)]d\tau = \int_{t_{k+1} - T}^{t_{k+1}} \mathbf{u}_l^{\mathrm{T}}(\tau)\mathbf{u}_l(\tau)d\tau - \int_{t_k - T}^{t_k} \mathbf{u}_l^{\mathrm{T}}(\tau)\mathbf{u}_l(\tau)d\tau.$$

Similar discussion applies to $\int_{t_k^+}^{t_{k+1}} \mathbf{u}_r^{\mathrm{T}}(\tau - T)\mathbf{u}_r(\tau - T)d\tau$. Therefore, by substituting these results in the lower bound in (4.10) and summing over $k \in \{0, \cdots, S - 1\}$ we obtain

$$\sum_{k=0}^{S-1} \left[\frac{1}{2} \int_{t_k^+}^{t_{k+1}} \mathbf{u}_l^{\mathrm{T}}(\tau)\mathbf{u}_l(\tau) - \mathbf{u}_l^{\mathrm{T}}(\tau - T)\mathbf{u}_l(\tau - T) \right.$$
$$\left. + \mathbf{u}_r^{\mathrm{T}}(\tau)\mathbf{u}_r(\tau) - \mathbf{u}_r^{\mathrm{T}}(\tau - T)\mathbf{u}_r(\tau - T)d\tau \right]$$
$$= \frac{1}{2} \sum_{k=0}^{S-1} \left[\int_{t_{k+1} - T}^{t_{k+1}} \mathbf{u}_l^{\mathrm{T}}(\tau)\mathbf{u}_l(\tau)d\tau - \int_{t_k - T}^{t_k} \mathbf{u}_l^{\mathrm{T}}(\tau)\mathbf{u}_l(\tau)d\tau \right.$$
$$\left. + \int_{t_{k+1} - T}^{t_{k+1}} \mathbf{u}_r^{\mathrm{T}}(\tau)\mathbf{u}_r(\tau)d\tau - \int_{t_k - T}^{t_k} \mathbf{u}_r^{\mathrm{T}}(\tau)\mathbf{u}_r(\tau)d\tau \right]$$
$$= \frac{1}{2} \left[\int_{t_S - T}^{t_S} \mathbf{u}_l^{\mathrm{T}}(\tau)\mathbf{u}_l(\tau)d\tau + \int_{t_S - T}^{t_S} \mathbf{u}_r^{\mathrm{T}}(\tau)\mathbf{u}_r(\tau)d\tau \right] \tag{4.13}$$

since $t_0 = 0$ and both $\mathbf{u}_l(t) = 0$ and $\mathbf{u}_r(t) = 0$ for $t < 0$. With a similar process for the last term in (4.5), we can obtain the following lower bound

$$\int_{t_S^+}^{t} (\hat{\mathbf{r}}_{m_{i_S}}^{\mathrm{T}}(\tau)\hat{\mathbf{f}}_{m_{i_S}}(\tau) - \hat{\mathbf{r}}_{s_{i_S}}^{\mathrm{T}}(\tau)\hat{\mathbf{f}}_{s_{i_S}}(\tau))d\tau \geq \frac{1}{2}\Big[\int_{t-T}^{t} \mathbf{u}_l^{\mathrm{T}}(\tau)\mathbf{u}_l(\tau)d\tau - \int_{t_S-T}^{t_S} \mathbf{u}_l^{\mathrm{T}}(\tau)\mathbf{u}_l(\tau)d\tau$$
$$\int_{t-T}^{t} \mathbf{u}_r^{\mathrm{T}}(\tau)\mathbf{u}_r(\tau)d\tau - \int_{t_S-T}^{t_S} \mathbf{u}_r^{\mathrm{T}}(\tau)\mathbf{u}_r(\tau)d\tau\Big]. \qquad (4.14)$$

Summing the lower bounds in (4.13) and (4.14) gives the following lower bound for (4.5)

$$\frac{1}{2}\left[\int_{t-T}^{t} \mathbf{u}_l^{\mathrm{T}}(\tau)\mathbf{u}_l(\tau)d\tau + \int_{t-T}^{t} \mathbf{u}_r^{\mathrm{T}}(\tau)\mathbf{u}_r(\tau)d\tau\right] \geq 0.$$

which means that Equation (4.5) is non-negative and hence passivity of the communication channel under switching, delay and variable scaling is guaranteed. ∎

Thus, utilizing this passivity result, we can define the following storage function, later used in Section 4.8 for the proof of convergence, for communication channel

$$V_{ch}(t) = \text{L.H.S of Eqn.}(4.5) \geq 0. \qquad (4.15)$$

4.7 Passive Filtering

As mentioned earlier in Section 4.3, switches to different leader robots cause discontinuity of the force feedback as well as velocity commands. These discontinuities can cause sudden force feedback changes on the haptic device and consequently inconvenience and confusion of the human operator. Thus, it is better to smoothen these signals before applying them to the robots as well as on the haptic device. This can be achieved via low-pass filtering methods (i.e. Blocks B3 and B5 in Figures 4.1 and 4.3). However, it should be noted that improper filtering can cause loss of passivity [73]. Thus, we apply a passive two-port filtering method shown in Figure 4.5 and detailed in the following Proposition.

Proposition 3 *Consider a two-port filter as shown in Figure 4.5 with inputs $[\mathbf{u}_{1f}^{\mathrm{T}}\ \mathbf{u}_{2f}^{\mathrm{T}}] \in \mathbb{R}^{2m}$ and outputs $[\mathbf{y}_{1f}^{\mathrm{T}}\ \mathbf{y}_{2f}^{\mathrm{T}}] \in \mathbb{R}^{2m}$ and their piecewise continuous form in any $t \in (t_k, t_{k+1}]$ being denoted as $[\mathbf{u}_{1f_k}^{\mathrm{T}}\ \mathbf{u}_{2f_k}^{\mathrm{T}}]$ and $[\mathbf{y}_{1f_k}^{\mathrm{T}}\ \mathbf{y}_{2f_k}^{\mathrm{T}}]$, respectively. Assume that $\mathbf{u}_{2f}$ is to be filtered via $\frac{\omega_c}{s+\omega_c}$ with cutoff frequency ω_c and the filter holds no initial energy $V(0) = 0$. This two-port filter is passive according*
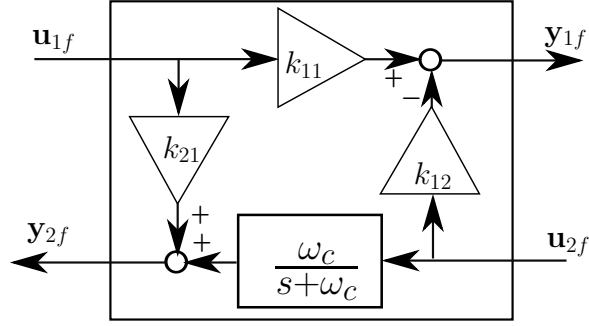
Figure 4.5: Two-port filter.

to Definition 3 with

$$\mathbf{y}_k^{\mathrm{T}}(t)\mathbf{u}_k(t) \triangleq \mathbf{u}_{1f_k}^{\mathrm{T}}(t)\mathbf{y}_{2f_k}(t) - \mathbf{u}_{2f_k}^{\mathrm{T}}(t)\mathbf{y}_{1f_k}(t) \tag{4.16}$$

if the filter gains are chosen as $k_{11} = \frac{\omega_c}{s+\omega_c}$, $\{k_{21}, k_{12}\} \geq 0$.

Proof. For any interval $t \in (t_k, t_{k+1}]$, with $k \in \{1, \cdots, S-1\}$ we have

$$\mathbf{u}_{1f_k}^{\mathrm{T}}(t)\mathbf{y}_{2f_k}(t) - \mathbf{u}_{2f_k}^{\mathrm{T}}(t)\mathbf{y}_{1f_k}(t) = \mathbf{u}_{1f_k}^{\mathrm{T}}(t)\big(k_{21}\mathbf{u}_{1f_k}(t) + \frac{\omega_c}{s+\omega_c}\mathbf{u}_{2f_k}(t)\big)$$
$$-\mathbf{u}_{2f_k}^{\mathrm{T}}(t)\big(k_{11}\mathbf{u}_{1f_k}(t) - k_{12}\mathbf{u}_{2f_k}(t)\big). \tag{4.17}$$

Choose $k_{11} = \frac{\omega_c}{s+\omega_c}$, $k_{21} \geq 0$ and $k_{12} \geq 0$ and (4.17) becomes

$$k_{21}\mathbf{u}_{1f_k}^{\mathrm{T}}(t)\mathbf{u}_{1f_k}^{\mathrm{T}}(t) + k_{12}\mathbf{u}_{2f_k}^{\mathrm{T}}(t)\mathbf{u}_{2f_k}(t) \geq 0.$$

Similar discussion applies to the interval $(t_S, t]$ and hence by summing the integral of supply rates over all intervals, the passivity condition (4.4) holds according to Definition 3. ∎

We can add two filters like this in cascade to each port of the passive communication channel as shown in Figure 4.3 for passive filtering. In the remaining parts of the chapter we choose $k_{21} = 0$ and $k_{12} = 0$ in each filter to obtain a lossless filter such that (4.16) is zero $\forall t$ and filters blocks do not apply unnecessary modification to the signals which results in

$$\mathbf{r}_{m_{i_k}}^{\mathrm{T}}\mathbf{f}_{m_{i_k}} - \hat{\mathbf{r}}_{m_{i_k}}^{\mathrm{T}}\hat{\mathbf{f}}_{m_{i_k}} = 0, \quad \hat{\mathbf{r}}_{s_{i_k}}^{\mathrm{T}}\hat{\mathbf{f}}_{s_{i_k}} - \mathbf{r}_{s_{i_k}}^{\mathrm{T}}\mathbf{f}_{s_{i_k}} = 0. \tag{4.18}$$

99

4.8 Slaves

In this section, we explain the dynamics, autonomous local control, and the haptic force feedback cues of the slaves shown in block B6 of Figure 4.1. We also discuss the passivity of this block in interaction with other parts of the scheme in Figure 4.1 (i.e. with the communication channel via force feedback and velocity commands). Based on the passivity of slave side, we prove the convergence of the team of robots in a position tracking and synchronization task under human teleoperation according to the scheme shown in Figure 4.1. Assume that the dynamics of motion of each slave are according to the following

$$\dot{\mathbf{q}}(t) = \mathbf{v}_i(t) \in \mathbb{R}^3, \text{for } i = 1, 2, ..., N$$

with N being the total number of robots in a 3D task space. For each robot we have

$$\mathbf{v}_i(t) = \mathbf{v}_{ai}(t) + \delta_{i_k}(t)\mathbf{r}_{s_{i_k}}(t) \tag{4.19}$$

where $\mathbf{v}_{ai}(t)$ is a local autonomous controller, $\mathbf{r}_{s_{i_k}}(t)$ is the manual control commands received through the communication channel in $(t_k, t_{k+1}]$ as shown in Figure 4.4 and $\delta_{i_k}(t)$ is defined as

$$\delta_{i_k}(t) = \begin{cases} 1 & \text{if slave } i \text{ is the leader in } t \in (t_k, t_{k+1}] \\ 0 & \text{otherwise} \end{cases}$$

with $\sum_i \delta_{i_k}(t) = 1$, i.e. only one leader robot is controlled manually in each $t \in (t_k, t_{k+1}]$. We assume that the robot graph G_s is connected at all time. That is, for the Laplacian matrix we have $L\mathbf{1}_N = 0$ [43]. Define $\mathbf{r}_q \in \mathbb{R}^3$ as a desired location of robots only known to the human through visual feedback and the control goal as

$$\lim_{t \to \infty} ||\mathbf{q}_i(t) - \mathbf{r}_q|| = 0, \tag{4.20}$$

which indicates position synchronization of the robots at a desired location under the control scheme shown in Figure 4.1. In order to fulfill this goal, we utilize the control law proposed in [43] according

to the following

$$\dot{\zeta}_i \;=\; \sum_{j \in \mathcal{N}_i} a_{ij}(\mathbf{q}_j - \mathbf{q}_i),$$

$$\mathbf{v}_{ai} \;=\; \sum_{j \in \mathcal{N}_i} a_{ij}(\mathbf{q}_j - \mathbf{q}_i) + \sum_{j \in \mathcal{N}_i} a_{ij}(\zeta_i - \zeta_j). \tag{4.21}$$

Using (4.21), the dynamics for the entire team of robots can be written as

$$\begin{bmatrix} \dot{\zeta} \\ \dot{\mathbf{q}} \end{bmatrix} = \begin{bmatrix} 0 & -L \otimes I_3 \\ L \otimes I_3 & -L \otimes I_3 \end{bmatrix} \begin{bmatrix} \zeta \\ \mathbf{q} \end{bmatrix} + \begin{bmatrix} 0 \\ D_{i_k} \otimes I_3 \end{bmatrix} \mathbf{r}_{s_{i_k}} \tag{4.22}$$

where $\otimes$ is the Kronecker product, $\zeta = [\zeta_1^{\mathrm{T}} \cdots \zeta_N^{\mathrm{T}}]^{\mathrm{T}} \in R^{3N \times 1}$, $\mathbf{q} = [\mathbf{q}_1^{\mathrm{T}} \cdots \mathbf{q}_N^{\mathrm{T}}]^{\mathrm{T}} \in R^{3N \times 1}$, $D_{i_k}(t) = [\delta_{1_k}(t) \cdots \delta_{N_k}(t)]^{\mathrm{T}} \in R^{N \times 1}$, and I_3 is an identity matrix. We next provide some lemmas and make some necessary assumptions required for the proof of achieving the goal (4.20) under manual control.

Lemma 6 *The multi-robot system with dynamics (4.22) is passive with respect to the following common storage function in different leader configurations*

$$V_{f_s}(t) = \frac{1}{2}\mathbf{q}^{\mathrm{T}}(t)(L \otimes I_3)\mathbf{q}(t) + \frac{1}{2}\zeta^{\mathrm{T}}(t)(L \otimes I_3)\zeta(t) \geq 0 \tag{4.23}$$

where $\mathbf{r}_{s_{i_k}}(t)$ is the input and $(D_{i_k}(t) \otimes I_3)^{\mathrm{T}}(L \otimes I_3)\mathbf{q}(t)$ is chosen as the output, which is the relative position of the leader robot with its neighbors. This will provide useful force feedback information to help the operator keep the formation of the robot team. Hence, the output is chosen as the force feedback cue, i.e.

$$\mathbf{f}_{s_{i_k}} = (D_{i_k}(t) \otimes I_3)^{\mathrm{T}}(L \otimes I_3)\mathbf{q}(t). \tag{4.24}$$

Proof. Under the dynamics (4.22), for each period $(t_k, t_{k+1}]$ we have

$$\dot{V}_{f_s}(t) = -\mathbf{q}^{\mathrm{T}}(t)(L \otimes I_3)(L \otimes I_3)\mathbf{q}(t) + \mathbf{q}^{\mathrm{T}}(t)(L \otimes I_3)(D_{i_k}(t) \otimes I_3)\mathbf{r}_{s_{i_k}}(t) \tag{4.25}$$

Thus, using the inequality (4.4) in Definition 3, by integrating the supply rate (4.25) over for $[0, t]$ we have

$$
\begin{aligned}
V_{f_s}(t) \quad \leq \quad & \left\{ \sum_{k=0}^{S-1} \int_{t_k^+}^{t_{k+1}} \mathbf{q}^{\mathrm{T}}(\tau)(L \otimes I_3)(D_{i_k} \otimes I_3)\mathbf{r}_{s_{i_k}}(\tau)d\tau \right\} \\
& + \int_{t_S^+}^{t} \mathbf{q}^{\mathrm{T}}(\tau)(L \otimes I_3)(D_{i_S} \otimes I_3)\mathbf{r}_{s_{i_S}}(\tau)d\tau + V_{f_s}(0),
\end{aligned}
$$

∎

Define $y_{h_k}(t - T)$ as the delayed position of the leader robot seen by human through visual feedback according to

$$
\mathbf{y}_{h_k}(t - T) = (D_{i_k}(t - T) \otimes I_3)^{\mathrm{T}}\mathbf{q}(t - T) \tag{4.26}
$$

Also, define $\overline{\mathbf{q}}(t) = \mathbf{q} - (\mathbf{1}_N \otimes I_3)\mathbf{r}_q(t)$ as the team's position tracking error. Combining (4.26), we can formulate the position tracking error seen by human according to the following

$$
\mathbf{r}_q - \mathbf{y}_{h_k}(t - T) = -(D_{i_k}(t - T) \otimes I_3)\overline{\mathbf{q}}(t - T). \tag{4.27}
$$

Also, utilizing dynamics (4.22) and the fact that $L\mathbf{1}_N = 0$, we obtain the following

$$
\begin{bmatrix} \dot{\zeta} \\ \dot{\overline{\mathbf{q}}} \end{bmatrix} = \begin{bmatrix} 0 & -L \otimes I_3 \\ L \otimes I_3 & -L \otimes I_3 \end{bmatrix} \begin{bmatrix} \zeta \\ \overline{\mathbf{q}} \end{bmatrix} + \begin{bmatrix} 0 \\ D_{i_k} \otimes I_3 \end{bmatrix} \mathbf{r}_{s_{i_k}}. \tag{4.28}
$$

Lemma 7 *Using the dynamics in (4.28), we can show that the multi-robot system is passive with respect to the following common storage function, related to the position tracking error for the team of robots, in different leader configurations*

$$
V_e(t) = \frac{1}{2}\overline{\mathbf{q}}^{\mathrm{T}}(t)\overline{\mathbf{q}}(t) + \frac{1}{2}\zeta^{\mathrm{T}}(t)\zeta(t) \tag{4.29}
$$

where $\mathbf{r}_{s_{i_k}}(t)$ is the input and $(D_{i_k}(t - T) \otimes I_3)^{\mathrm{T}}\overline{\mathbf{q}}(t)$ is chosen as the output.

Proof. The proof is similar to that of Lemma 6 and hence omitted due to space limit. ∎

Next, we make some assumptions under which the robot team satisfies the convergence goal in (4.20) under the scheme in Figure 4.1.

Assumption 4 *Assume that the following holds for the slave multi-robot system:*

a) $\mathbf{r}_q$ *is a constant.*

b) Human sends $\mathbf{r}_{s_{i_k}}(t) = 0$ *if an only if* $\mathbf{y}_h(t) = \mathbf{r}_q$ *identically holds.*

c) Considering that the intervals between the leader switches satisfy $t_{k+1} - t_k \geq \tau_{min} \gg T$, *human control actions are passive according to the following*

$$
\begin{aligned}
V_h(t) \;=\; & \left\{ \sum_{k=0}^{S-1} \int_{t_k^+}^{t_{k+1}} \mathbf{r}_{s_{i_k}}^{\mathrm{T}}(\tau - T)(\mathbf{r}_q - \mathbf{y}_{h_k}(\tau - T)) - \mathbf{r}_{h_{i_k}}^{\mathrm{T}}(\tau)\mathbf{f}_{h_{i_k}}(\tau)d\tau \right\} \\
& + \int_{t_S^+}^{t} \mathbf{r}_{s_{i_S}}^{\mathrm{T}}(\tau - T)(\mathbf{r}_q - \mathbf{y}_{h_S}(\tau - T)) - \mathbf{r}_{h_{i_S}}^{\mathrm{T}}(\tau)\mathbf{f}_{h_{i_S}}(\tau)d\tau \geq -\beta_h, \qquad (4.30)
\end{aligned}
$$

where $\beta_h > 0$ *is a constant and* $\mathbf{r}_{h_{i_k}}(t)$ *and* $\mathbf{f}_{h_{i_k}}$ *denote* $\mathbf{r}_h(t)$ *and* $\mathbf{f}_h$ *when robot i is controlled in* $(t_k, t_{k+1}]$.

Remark 12 Assumption 4.c *considers that human exhibits a combined passive action from both cognitive perspective (i.e. by seeing the velocity command of the leader* $\mathbf{r}_{s_{i_k}}(t - T)$ *available through an Human Computer Interface as well as the position tracking error* $\mathbf{r}_q - \mathbf{y}_{h_k}(t - T)$, *both of which are subjected to delay from communication channel) and physical perspective (i.e. by applying force* $\mathbf{f}_{h_{i_k}}$ *to the haptic device). The passivity of the physical part is a common reasonable assumption made in the literature which is equivalent to*

$$
\sum_{k=0}^{S-1} \left\{ \int_{t_k^+}^{t_{k+1}} -\mathbf{r}_{h_{i_k}}^{\mathrm{T}}(\tau)\mathbf{f}_{h_{i_k}}(\tau)d\tau \right\} + \int_{t_S^+}^{t} -\mathbf{r}_{h_{i_S}}^{\mathrm{T}}(\tau)\mathbf{f}_{h_{i_S}}(\tau)d\tau \geq -\beta_{hp}, \qquad (4.31)
$$

where $\beta_{hp} > 0$ *is a constant and (4.31) means that physical control actions of human are bounded [60]. Here we made a cognitive assumption and augmented it to the previous physical assumption. It can be shown experimentally that via enough repetition and learning, human cognitive control actions can be passive for a reasonable range of tracking task frequencies (i.e. below 10 rad/seconds) [43]. However, proof of such a fact generally deserves a separate study which is beyond the scope of this chapter.* •

Next we prove that the goal (4.20) is satisfied under purely manual control.

Lemma 8 *The control scheme shown in Figure 4.1 is stable.*

Proof. Consider the equivalent port-based model shown in Figure 4.3. Since each block B1-B6 is passive and the blocks are interconnected in cascade, the entire scheme is passive and hence stable [73]. ∎

Theorem 6 *Consider the control scheme shown in Figure 4.1 for which* Assumption 4 *holds, with the slave dynamics (4.22), scattering transformations defined in (4.7) of Theorem 5 and filters defined in Proposition 3, the control goal (4.20) is achieved under any arbitrary trust-based switching scheme with purely manual control.*

Proof. Using the storage functions V_{hd} in (3.9) for haptic device, V_{ch} in (4.15) for the communication channel and variable scaling, V_{f_s} in (4.23) for position synchronization, V_e in (4.29) for tracking error, and V_h in (4.30) for human passivity, we define the following total storage function

$$V_T(t) = V_h(t) + \beta_h + V_{hd}(t) + V_{hd}(0) + V_{ch}(t) + V_{f_s}(t) + V_e(t-T) \geq 0, \tag{4.32}$$

where $V_e(t-T)$ is the delayed $V_e(t)$ defined in (4.29) which is a function of position tracking error and $V_{f_s}(t)$ represents inter-robot position synchronization. For any t in period $(t_k, t_{k+1}]$, $\dot{V}_{f_s}(t)$ is obtained by (4.25) and we also have

$$\dot{V}_h(t) = \mathbf{r}_{s_{i_k}}^{\mathrm{T}}(t-T)(\mathbf{r}_q - \mathbf{y}_{h_k}(t-T)) - \mathbf{r}_{h_{i_k}}^{\mathrm{T}}(t)\mathbf{f}_{h_{i_k}}(t)$$

$$\dot{V}_{hd}(t) = \mathbf{r}_{m_{i_k}}^{\mathrm{T}}(t)\mathbf{f}_{h_{i_k}}(t) - \mathbf{r}_{m_{i_k}}^{\mathrm{T}}(t)\mathbf{f}_{m_{i_k}}(t)$$

$$\dot{V}_{ch}(t) = \hat{\mathbf{r}}_{m_{i_k}}^{\mathrm{T}}(t)\hat{\mathbf{f}}_{m_{i_k}}(t) - \hat{\mathbf{r}}_{s_{i_k}}^{\mathrm{T}}(t)\hat{\mathbf{f}}_{s_{i_k}}(t)$$

$$\dot{V}_e(t) = -\overline{\mathbf{q}}^{\mathrm{T}}(t)(L \otimes I_3)\overline{\mathbf{q}}(t) + \overline{\mathbf{q}}^{\mathrm{T}}(t)(D_{i_k} \otimes I_3)\mathbf{r}_{s_{i_k}}(t). \tag{4.33}$$

Then, using (4.33) along with the lossless property of the filters shown in (4.18) and the fact that $\mathbf{r}_{h_{i_k}}(t) = \mathbf{r}_{m_{i_k}}(t)$, for (4.32) in any period $(t_k, t_{k+1}]$ we obtain,

$$\dot{V}_T(t) = \mathbf{r}_{s_{i_k}}^{\mathrm{T}}(t-T)(\mathbf{r}_q - \mathbf{y}_{h_k}(t-T)) - \mathbf{r}_{m_{i_k}}^{\mathrm{T}}(t)\mathbf{f}_{h_{i_k}}(t) + \mathbf{r}_{m_{i_k}}^{\mathrm{T}}(t)\mathbf{f}_{h_{i_k}}(t)$$

$$-\mathbf{r}_{m_{i_k}}^{\mathrm{T}}(t)\mathbf{f}_{m_{i_k}}(t) + \mathbf{r}_{m_{i_k}}^{\mathrm{T}}(t)\mathbf{f}_{m_{i_k}}(t) - \hat{\mathbf{r}}_{m_{i_k}}^{\mathrm{T}}(t)\hat{\mathbf{f}}_{m_{i_k}}(t) + \hat{\mathbf{r}}_{m_{i_k}}^{\mathrm{T}}(t)\hat{\mathbf{f}}_{m_{i_k}}(t)$$

$$-\hat{\mathbf{r}}_{s_{i_k}}^{\mathrm{T}}(t)\hat{\mathbf{f}}_{s_{i_k}}(t) + \hat{\mathbf{r}}_{s_{i_k}}^{\mathrm{T}}(t)\hat{\mathbf{f}}_{s_{i_k}}(t) - \mathbf{r}_{s_{i_k}}^{\mathrm{T}}(t)\mathbf{f}_{s_{i_k}}(t)$$

$$-\mathbf{q}^{\mathrm{T}}(t)(L \otimes I_3)(L \otimes I_3)\mathbf{q}(t) + \mathbf{q}^{\mathrm{T}}(t)(L \otimes I_3)(D_{i_k} \otimes I_3)\mathbf{r}_{s_{i_k}}(t)$$

$$-\overline{\mathbf{q}}^{\mathrm{T}}(t-T)(L \otimes I_3)\overline{\mathbf{q}}(t-T) + \overline{\mathbf{q}}^{\mathrm{T}}(t-T)(D_{i_k}(t-T) \otimes I_3)\mathbf{r}_{s_{i_k}}(t-T). \tag{4.34}$$

104

Substituting (4.27) and (4.24) in (4.34) results in

$$\dot{V}_T(t) = -\mathbf{q}^{\mathrm{T}}(t)(L \otimes I_3)(L \otimes I_3)\mathbf{q}(t) - \overline{\mathbf{q}}^{\mathrm{T}}(t-T)(L \otimes I_3)\overline{\mathbf{q}}(t-T). \qquad (4.35)$$

Therefore, $\dot{V}_T = 0$ whenever $(L \otimes I_3)\overline{\mathbf{q}}(t-T) = 0$ and $(L \otimes I_3)\mathbf{q}(t) = 0$, both of which indicate position synchronization of robots but not necessarily the fulfillment of the tracking goal in (4.20). If in addition to $\dot{V}_T = 0$, we can show that $\mathbf{r}_{s_{i_k}}(t-T) = 0$ and $\mathbf{r}_{s_{i_k}}(t) = 0$, according to *Assumption 4.b*, the proof of convergence under the manual control is complete. In the following, we prove $\mathbf{r}_{s_{i_k}}(t - T) = 0$ and then extend to $\mathbf{r}_{s_{i_k}}(t) = 0$. Consider the case that the following holds

$$(L \otimes I_3)\overline{\mathbf{q}}(t-T) = 0. \qquad (4.36)$$

Using the dynamics (4.28), time derivative of (4.36) is given by

$$(L \otimes I_3)\big[-(L \otimes I_3)\overline{\mathbf{q}}(t-T) + (L \otimes I_3)\zeta(t-T) + (D_{i_k}(t-T) \otimes I_3)\mathbf{r}_{s_{i_k}}(t-T)\big] = 0.$$

Substitute (4.36) and the above equation becomes

$$(L \otimes I_3)\big[(L \otimes I_3)\zeta(t-T) + (D_{i_k}(t-T) \otimes I_3)\mathbf{r}_{s_{i_k}}(t-T)\big] = 0,$$

which accordingly, under the graph connectivity assumption (i.e. $L\mathbf{1}_N = 0$), results in

$$\underbrace{(L \otimes I_3)\zeta(t-T) + (D_{i_k}(t-T) \otimes I_3)\mathbf{r}_{s_{i_k}}(t-T)}_{\dot{\overline{\mathbf{q}}}(t-T)} = (\mathbf{1}_N \otimes I_3)\mathbf{c}(t-T) \qquad (4.37)$$

where $\mathbf{c}(t-T) \in \mathbb{R}^3 \ \forall t-T > 0$. Multiplying both sides of (4.37) by $(\mathbf{1}_N \otimes I_3)^{\mathrm{T}}$ gives

$$(\mathbf{1}_N \otimes I_3)^{\mathrm{T}}(D_{i_k}(t-T) \otimes I_3)\mathbf{r}_{s_{i_k}}(t-T) = (\mathbf{1}_N \otimes I_3)^{\mathrm{T}}(\mathbf{1}_N \otimes I_3)\mathbf{c}(t-T)$$

which means $\mathbf{r}_{s_{i_k}}(t-T) = N\mathbf{c}(t-T)$. Substituting this in (4.37) results in

$$(L \otimes I_3)\zeta(t-T) = ((\mathbf{1}_N \otimes I_3) - N(D_{i_k}(t-T) \otimes I_3))\mathbf{c}(t-T). \qquad (4.38)$$

Notice that when $(L \otimes I_3)\overline{\mathbf{q}}(t-T) = 0$ happens in (4.36), according to (4.28), $\zeta(t-T)$ is a constant. Thus, according to (4.38), $\mathbf{c}(t-T)$ and hence $\mathbf{r}_{s_{i_k}}(t-T)$ is a constant. If $\mathbf{c}(t-T) = 0$ and hence $\mathbf{r}_{s_{i_k}}(t-T) = 0$, then we know that according to *Assumption 4.b*, the goal (4.20) is achieved at $t-T$. Next we show that $\mathbf{c}(t-T) = 0$. To prove this, we use proof by contradiction. Consider the case that $\mathbf{c}(t-T) \neq 0$. Then if we differentiate the term $\overline{\mathbf{q}}^{\mathrm{T}}(t-T)(D_{i_k}(t-T) \otimes I_3)\mathbf{r}_{s_{i_k}}(t-T)$ and considering that $\mathbf{r}_{s_{i_k}}(t-T)$ is constant and $D_{i_k}(t-T)$ is piecewise constant, we obtain

$$\frac{d}{dt}\overline{\mathbf{q}}^{\mathrm{T}}(t-T)(D_{i_k}(t-T) \otimes I_3)\mathbf{r}_{s_{i_k}}(t-T) = \dot{\overline{\mathbf{q}}}^{\mathrm{T}}(t-T)(D_{i_k}(t-T) \otimes I_3)\mathbf{r}_{s_{i_k}}(t-T)$$

which by using (4.37) and $\mathbf{r}_{s_{i_k}}(t-T) = N\mathbf{c}(t-T)$ becomes

$$= \mathbf{c}^{\mathrm{T}}(t-T)(\mathbf{1}_N \otimes I_3)^{\mathrm{T}}(D_{i_k}(t-T) \otimes I_3)\frac{\mathbf{c}(t-T)}{N}$$
$$= \frac{\|c(t-T)\|_2^2}{N} > 0.$$

This along with (4.27) implies that $\overline{\mathbf{q}}^{\mathrm{T}}(t-T)(D_{i_k}(t-T) \otimes I_3)\mathbf{r}_{s_{i_k}}(t-T) = -\mathbf{r}_{s_{i_k}}^{\mathrm{T}}(t-T)(\mathbf{r}_q - \mathbf{y}_{h_k}(t-T))$ is monotonically increasing which, considering (4.31), violates (4.30). Therefore, $\mathbf{r}_{s_{i_k}}(t-T) = 0$ which according to *Assumption 4*.b implies $\mathbf{y}_{h_k}(t-T) = \mathbf{r}_q$. Therefore, when (4.36) holds convergence and synchronization occur at $t-T$. Now, we just need to prove that convergence at $t-T$ results in convergence at t according to what follows. Considering that $c(t-T) = \mathbf{0}$, according to (4.38), $\zeta(t-T)$ is synchronized. Thus, when both $\zeta(t-T)$ and $\overline{\mathbf{q}}(t-T)$ (similarly $\mathbf{q}(t-T)$) reach synchronization (i.e. $(L \otimes I_3)\zeta(t-T) = 0$ and $(L \otimes I_3)\overline{\mathbf{q}}(t-T) = 0$) and we also know that $\mathbf{r}_{s_{i_k}}(t-T) = 0$, the dynamics in (4.28) (similarly (4.22)) reaches an equilibrium and stays there which results in $(L \otimes I_3)\mathbf{q}(t) = 0$ in (4.35). In this case, all the control inputs and force feedbacks are identically zero. Therefore, when $\dot{V}_T = 0$ in (4.35) occurs, the goal (4.20) is achieved. ∎

Remark 13 *When human is not taking part in the control, i.e. human is not applying any control force to the haptic device ($\mathbf{f}_h(t) = 0, \forall t > 0$), we can define $V_{Ta}(t) = V_{hd}(t) + V_{hd}(0) + V_{ch}(t) + V_{f_s}(t) \geq 0$ as the storage function for the team of robots. Thus, with a similar approach as for $\dot{V}_T$, for any $t \in (t_k, t_{k+1}]$ we obtain $\dot{V}_{Ta}(t) = -\mathbf{q}^{\mathrm{T}}(t)(L \otimes I_3)(L \otimes I_3)\mathbf{q}(t)$ which only implies position synchronization when $(L \otimes I_3)\mathbf{q}(t) = 0$ (i.e. $\dot{V}_{Ta}(t) = 0$) but not necessarily at the desired location $\mathbf{r}_q$ since that position is only known to the human and is not considered in the $\mathbf{v}_{ai}$ control law for the robots. This justifies having a human-in-the-loop for improved performance.* •

4.9 Conclusion

In this chapter, we developed a trust-based leader switching scheme for multi-robot bilateral teleoperation. We guaranteed the stability of the entire closed-loop system under the effects of delay, filtering, and trust-based variable scaling and switching. We also proved the collective position tracking and synchronization performance of the multi-robot team under manual control via the proposed switching scheme. Our future work will include robot experiments with human-in-the-loop similar to [85] and [86] as well as investigate different models of trust.

Chapter 5

Conclusions and Future Work

5.1   Conclusions

In this dissertation, several methods for decision-making aids in (semi)autonomous control of mobile robotics systems via computational trust-based measures were developed and tested. It was demonstrated that generally these types of decision aids seem more natural to human than performance maximization methods. Moreover, they can improve the overall task performance of the control system compared to manual autonomy allocation by eliminating the undesired effects of subjective bias and uncertainty. The result of subjective questionnaires such as trust and preference are strong indicative of such a claim. Meanwhile, the proposed decision aids can reduce the operator workload in decision-making about the allocation of autonomy. This results is also reflected in the workload measurements via the NASA TLX questionnaire. Along the way of realizing such trust-based decision aids systems, several control engineering concepts and theories such as dwell time, steady-state bounds on the states, and passivity were utilized in order to predict the outcome of the proposed schemes as well as to guarantee their stability. Based on the intuitions and insights gained throughout accomplishing the previous steps, several new ideas can be proposed for the further extensions of these works. These ideas are presented, in the following.

5.2 Future Works

In Chapter 4, we extended the trust-based mixed-initiative scheme to the multi-robot applications and proved how the robots can converge to a desired formation under the proposed scheme. As the next step, similar to the Chapters 2 and 3, a testbed can be developed to test the proposed control scheme with multiple human subjects. The proposed method includes the development of a team of Robotino ground robots in the Gazebo [102] 3D simulator integrated with a Novint Falcon device. This design matches the assumptions of the robot dynamics in (4.19) and also provides a bilateral teleoperation scheme in order to apply force feedback to the operator according to the (4.24). Another challenge in the implementation of the proposed scheme is related to the operator's perception of performances and trust while s/he is controlling multiple robots. This case is different than the single-robot case in which the operator can easily focus on the performance of the specific controlled robot and keep track of the trust and allocation. Therefore, developing methods for improving the transparency of the performances as well as trust models in the multi-robot case is an interesting problem to be considered. Moreover, various trust-based correct allocation schemes in the multi-robot case can be considered. In Chapter 4, we briefly introduces a leader selection policy based on the trust. A separate study can include various trust-based leader selection policies to evaluate identify which policies are more consistent with human decision-making pattern in the multi-robot cases.

In experiments carried out in Chapters 2 and 3, we compared the proposed trust-based schemes against various optimal or performance maximization schemes. The trust-based schemes generally lead to higher preference and trust of the operator and guarantee an improved range of performance while the optimal methods result in lower human acceptance but higher task performance. A combinations of these two methods may result in a more effective scheme which yields high acceptance by human as well as a very high task performance. This requires more precise models of trust since the optimization methods rely on the system dynamic model to provide a reasonable outcome. Therefore, achieving this goal necessitates tackling two new problems: i) identifying more accurate models of trust which can become task specific, and ii) utilizing the model identification results in a real-time optimal algorithm such as MPC and evaluating the results.

Appendices

Appendix A   Optimal Allocation Mixed-Initiative (OMI) Control Scheme

We provide the details of the optimal allocation mixed-initiative (OMI) control scheme utilized in the experiments of Chapter 3 in this appendix. In order to apply this control scheme on the testbed shown in Figure 3.15, we first conduct a simple identification test on the Parrot AR. Drone 2.0. In the identification tests, we try to identify linear models of the dynamics of this UAV which will be later used in a Model Predictive Control scheme to apply an optimal blending between the manual and autonomous control commands of the UAV (i.e., to find an $\alpha(t)$ that minimizes the tracking error as well as the deviations from the manual commands sent by human). These linear models are precise enough to predict the dynamics of the UAV in the normal flight conditions (i.e. when the UAV is not used to perform flips or any other fast maneuver which is the case in the experiments done in this paper) [30, 55, 87]. However, since four pairs of Phasespace markers are added to the UAV used in the experiments, we redo the identification in order to obtain a more accurate model for the current test. Therefore, a collection of continuous control commands are send to the UAV and the resulting velocities of the UAV on the body frame are measured. This information is then used in the MATLAB System Identification Toolbox [104] to find the linear models that best fit the measurements. After the parameter identification process, the following linear models were identified

$$
\begin{aligned}
\frac{v_x}{u_{uav_x}} &= \frac{9.22}{s^2 + 1.475s + 0.2214}, \\
\frac{v_y}{u_{uav_y}} &= \frac{3.806}{s^2 + 0.4706s + 2.457}, \\
\frac{v_z}{u_{uav_z}} &= \frac{0.985}{s + 0.4952},
\end{aligned}
\tag{1}
$$

where u_{uav_x}, u_{uav_y}, and u_{uav_z} are the input commands to the UAV and v_x, v_y, and v_z are the output velocites of the UAV. Next, we explain the details of the optimal blending method based on the identified dynamic models of the UAV.

Since we utilized the optimal blending method proposed in [98], we define the following states and inputs and assume that the manual control input from human, i.e. $\mathbf{u}_h$, remains constant during the 0.2-second prediction horizon

x_1: manual control input along X axis (i.e. u_{hx})

x_2: manual control input along Y axis (i.e. u_{hy})

x_3: manual control input along Z axis (i.e. u_{hz})

x_4: autonomous control input along X axis (i.e. u_{ax})

x_5: autonomous control input along Y axis (i.e. u_{ay})

x_6: autonomous control input along Z axis (i.e. u_{az})

x_7: tracking error along X axis (i.e. e_x)

x_8: tracking error along Y axis (i.e. e_y)

x_9: tracking error along Z axis (i.e. e_z)

x_{10}: velocity error along X axis (i.e. $\dot{e}_x$)

x_{11}: velocity error along Y axis (i.e. $\dot{e}_y$)

x_{12}: velocity error along Z axis (i.e. $\dot{e}_z$)

x_{13}: acceleration error along X axis (i.e. $\ddot{e}_x$)

x_{14}: acceleration error along y axis (i.e. $\ddot{e}_y$)

u_1: the allocation function (i.e. $\alpha(t)$)

Considering that the total input to the UAV is $\mathbf{u}_{uav} = \alpha(t)\mathbf{u}_h + (1 - \alpha(t))\mathbf{u}_a$, we substitute this value in transfer functions (1) and obtain the following state dynamics

$$
\begin{aligned}
\dot{x}_1(t) &= 0 \\
\dot{x}_2(t) &= 0 \\
\dot{x}_3(t) &= 0 \\
\dot{x}_4(t) &= 0.5x_{10}(t) + 0.02x_{13}(t) \\
\dot{x}_5(t) &= 0.5x_{11}(t) + 0.02x_{14}(t) \\
\dot{x}_6(t) &= 1.5x_{12}(t)
\end{aligned}
$$

$$\dot{x}_7(t) = x_{10}(t)$$

$$\dot{x}_8(t) = x_{11}(t)$$

$$\dot{x}_9(t) = x_{12}(t)$$

$$\dot{x}_{10}(t) = x_{13}(t)$$

$$\dot{x}_{11}(t) = x_{14}(t)$$

$$\dot{x}_{12}(t) = -0.495x_{12}(t) - 0.985\big(x_3(t)u_1(t) + x_6(t)(1 - u_1(t))\big)$$

$$\dot{x}_{13}(t) = -1.473x_{13}(t) - 0.2214x_{10} - 9.22\big(x_1(t)u_1(t) + x_4(t)(1 - u_1(t))\big)$$

$$\dot{x}_{14}(t) = -0.4706x_{14}(t) - 2.457x_{11} - 3.806\big(x_2(t)u_1(t) + x_5(t)(1 - u_1(t))\big)$$

According to [98], we define the following cost function such that the tracking error as well as the deviation of the UAV commands from the manual control commands are minimized

$$J(t) = \int_0^t \mathbf{x}^{\mathrm{T}}(\tau)Q\mathbf{x}(\tau) + \big(\mathbf{u}_{uav}(\tau) - \mathbf{u}_h(\tau)\big)^{\mathrm{T}} R\big(\mathbf{u}_{uav}(\tau) - \mathbf{u}_h(\tau)\big)d\tau, \qquad (2)$$

with the weight matrices R and Q chosen as

$$R = \mathrm{diag}[1, 1, 1], \quad Q = \mathrm{diag}[0, 0, 0, 0, 0, 0, 200, 200, 200, 0, 0, 0, 0, 0]$$

such that the tracking error decreases and the total control input does not deviate too much from human input. Since $\mathbf{u}_{uav} = \alpha(t)\mathbf{u}_h + (1 - \alpha(t))\mathbf{u}_a$, the cost function (2) becomes

$$
\begin{aligned}
J(t) &= \int_0^t \mathbf{x}^{\mathrm{T}}(\tau)Q\mathbf{x}(\tau) + (1 - \alpha(\tau))^2\big(\mathbf{u}_a(\tau) - \mathbf{u}_h(\tau)\big)^{\mathrm{T}}(\tau)R\big(\mathbf{u}_a(\tau) - \mathbf{u}_h(\tau)\big)d\tau \\
&= \int_0^t \mathbf{x}^{\mathrm{T}}(\tau)Q\mathbf{x}(\tau) + (1 - u_1(\tau))^2\big((x_1 - x_4)^2 + (x_2 - x_5)^2 + (x_3 - x_6)^2\big)d\tau \qquad (3)
\end{aligned}
$$

We utilize the state dynamics (2) and the cost function (3) to implement the OMI allocation scheme on the testbed in Figure 3.15. The real-time codes are applied using the NMPC solvers provided by [1] which are integrated with the other components of the experimental setup of Figure 3.15 via Robot Operating System (ROS).

Bibliography

[1] F. Allgöwer and A. Zheng. *Nonlinear Model Predictive Control*, volume 26. Birkhäuser, 2012.

[2] R.J. Anderson and M.W. Spong. Bilateral control of teleoperators with time delay. *IEEE Transactions on Automatic Control*, 34(5):494–501, 1989.

[3] S.J. Anderson, S.C. Peters, T.E. Pilutti, and K. Iagnemma. An optimal-control-based framework for trajectory planning, threat assessment, and semi-autonomous control of passenger vehicles in hazard avoidance scenarios. *International Journal of Vehicle Autonomous Systems*, 8(2-4):190–216, 2010.

[4] S. Arogeti and N. Berman. Path following of autonomous vehicles in the presence of sliding effects. *IEEE Transactions on Vehicular Technology*, 61(4):1481–1492, 2012.

[5] D. Billman, M. Feary, and J. Rochlis Zumbado. Evidence report: Risk of inadequate design of human and automation/robotic integration, 2011.

[6] A.M. Bisantz and Y. Seong. Assessment of operator trust in and utilization of automated decision-aids under different framing conditions. *International Journal of Industrial Ergonomics*, 28(2):85–97, 2001.

[7] D. Botturi, M. Vicentini, M. Righele, and C. Secchi. Perception-centric force scaling in bilateral teleoperation. *Mechatronics*, 20(7):802–811, 2010.

[8] M.M. Botvinick, S. Huffstetler, and J.T. McGuire. Effort discounting in human nucleus accumbens. *Cognitive, Affective, & Behavioral Neuroscience*, 9(1):16–27, 2009.

[9] M.S. Branicky. Multiple lyapunov functions and other analysis tools for switched and hybrid systems. *IEEE Transactions on Automatic Control*, 43(4):475–482, 1998.

[10] D.J. Bruemmer, D.D. Dudenhoeffer, and J.L. Marble. Dynamic-autonomy for urban search and rescue. In *AAAI Mobile Robot Competition*, pages 33–37, 2002.

[11] S.P. Buerger and N. Hogan. Complementary stability and loop shaping for improved human–robot interaction. *IEEE Transactions on Robotics*, 23(2):232–244, 2007.

[12] J.R. Busemeyer and T.J. Pleskac. Theoretical tools for understanding and aiding dynamic decision making. *Journal of Mathematical Psychology*, 53(3):126–138, 2009.

[13] M. Cao, A. Stewart, and N.E. Leonard. Integrating human and robot decision-making dynamics with feedback: Models and convergence analysis. In *Proceedings of 47th IEEE Conference on Decision and Control (CDC)*, pages 1127–1132. IEEE, 2008.

[14] G. Charalambous, S. Fletcher, and P. Webb. The development of a scale to evaluate trust in industrial human-robot collaboration. *International Journal of Social Robotics*, pages 1–17, 2015.

[15] J.Y. Chen, K. Procci, M. Boyce, J. Wright, A. Garcia, and M. Barnes. Situation awareness-based agent transparency. Technical report, DTIC Document, 2014.

[16] J.Y.C. Chen and M.J. Barnes. Human-agent teaming for multirobot control: a review of human factors issues. *IEEE Transactions on Human-Machine Systems*, 44(1):13–29, 2014.

[17] J.Y.C. Chen, E.C. Haas, and M.J. Barnes. Human performance issues and user interface design for teleoperated robots. *IEEE Transactions on Systems, Man, and Cybernetics, Part C: Applications and Reviews*, 37(6):1231–1245, 2007.

[18] R. Chipalkatty, G. Droge, and M.B. Egerstedt. Less is more: Mixed-initiative model-predictive control with human inputs. *IEEE Transactions on Robotics*, 29(3):695–703, 2013.

[19] A.S. Clare. Modeling real-time human-automation collaborative scheduling of unmanned vehicles. Technical report, DTIC Document, 2013.

[20] J. Corredor, Sofrony, and A. Peer. Deciding on optimal assistance policies in haptic shared control tasks. In *IEEE International Conference on Robotics and Automation (ICRA)*, pages 2679–2684. IEEE, 2014.

[21] J.W. Crandall, M.L. Cummings, P. Della, d.J. Mauro, and M.A. Paul. Computing the effects of operator attention allocation in human control of multiple robots. *IEEE Transactions on Systems, Man, and Cybernetics-Part A: Systems and Humans*, 41(3):385–397, 2011.

[22] J.W. Crandall, M. Goodrich, D.R. Olsen Jr, and C.W. Nielsen. Validating human-robot interaction schemes in multitasking environments. *Systems, Man and Cybernetics, Part A: Systems and Humans, IEEE Transactions on*, 35(4):438–449, 2005.

[23] J.W. Crandall and M.A. Goodrich. Characterizing efficiency of human robot interaction: A case study of shared-control teleoperation. In *Intelligent Robots and Systems, 2002. IEEE/RSJ International Conference on*, volume 2, pages 1290–1295. IEEE, 2002.

[24] J.W. Crandall, C.W. Nielsen, and M. Goodrich. Towards predicting robot team performance. In *IEEE International Conference on Systems, Man and Cybernetics*, volume 1, pages 906–911. IEEE, 2003.

[25] E. de Visser and R. Parasuraman. Adaptive aiding of human-robot teaming effects of imperfect automation on performance, trust, and workload. *Journal of Cognitive Engineering and Decision Making*, 5(2):209–231, 2011.

[26] P. de Vries, C. Midden, and D. Bouwhuis. The effects of errors on system trust, self-confidence, and the allocation of control in route planning. *International Journal of Human-Computer Studies*, 58(6):719–735, 2003.

[27] X.C. Ding, M. Powers, M. Egerstedt, S.Y. Young, and T. Balch. Executive decision support. *Robotics & Automation Magazine, IEEE*, 16(2):73–81, 2009.

[28] C. Duma, N. Shahmehri, and G. Caronni. Dynamic trust metrics for peer-to-peer systems. In *Proceedings. Sixteenth International Workshop on Database and Expert Systems Applications*, pages 776–781. IEEE, 2005.

[29] M.T. Dzindolet, S.A. Peterson, R.A. Pomranky, L.G. Pierce, and H.P. Beck. The role of trust in automation reliance. *International Journal of Human-Computer Studies*, 58(6):697–718, 2003.

[30] J. Engel, J. Sturm, and D. Cremers. Camera-based navigation of a low-cost quadrocopter. In *2012 IEEE/RSJ International Conference on Intelligent Robots and Systems*, pages 2815–2821. IEEE, 2012.

[31] A. Fernández, A. Barreiro, A. Banos, and J. Carrasco. Reset control for passive teleoperation. In *Industrial Electronics, 2008. IECON 2008. 34th Annual Conference of IEEE*, pages 2935–2940. IEEE, 2008.

[32] F. Flemisch, M. Heesen, T. Hesse, J. Kelsch, A. Schieben, and J. Beller. Towards a dynamic balance between humans and automation: Authority, ability, responsibility and control in shared and cooperative control situations. *Cognition, Technology & Work*, 14(1):3–18, 2012.

[33] A. Franchi, H.H. Bülthoff, and P.R. Giordano. Distributed online leader selection in the bilateral teleoperation of multiple uavs. In *2011 50th IEEE Conference on Decision and Control and European Control Conference*, pages 3559–3565. IEEE, 2011.

[34] A. Franchi, C. Secchi, M. Ryll, H.H. Bülthoff, and P.R. Giordano. Shared control: Balancing autonomy and human assistance with a group of quadrotor uavs. *Proceedings of IEEE on Robotics & Automation Magazine*, 19(3):57–68, 2012.

[35] A. Freedy, E. DeVisser, G. Weltman, and N. Coeyman. Measurement of trust in human-robot collaboration. In *International Symposium on Collaborative Technologies and Systems (CTS)*, pages 106–114. IEEE, 2007.

[36] S. Fu, H. Saeidi, E. Sand, B. Sadrfaridpour, J. Rodriguez, Y. Wang, and J.R. Wagner. A haptic interface with adjustable feedback for unmanned aerial vehicles (uavs)model, control, and test. In *accepted for presentation in American Control Conference*, pages 467–472. IEEE, 2016.

[37] F. Gao, A.S. Clare, J.C. Macbeth, and M.L. Cummings. Modeling the impact of operator trust on performance in multiple robot control. AAAI, 2013.

[38] J. Gao and J.D. Lee. Extending the decision field theory to model operators' reliance on automation in supervisory control situations. *IEEE Transactions on Systems, Man and Cybernetics, Part A: Systems and Humans*, 36(5):943–959, 2006.

[39] W. Gao, Y. Wang, and A. Homaifa. Discrete-time variable structure control systems. *IEEE Transactions on Industrial Electronics*, 42(2):117–122, 1995.

[40] C. Gonzalez. Decision support for real-time, dynamic decision-making tasks. *Organizational Behavior and Human Decision Processes*, 96(2):142–154, 2005.

[41] P.A. Hancock, D.R. Billings, K.E. Schaefer, J.Y.C. Chen, E.J. De Visser, and R. Parasuraman. A meta-analysis of factors affecting trust in human-robot interaction. *Human Factors: The Journal of the Human Factors and Ergonomics Society*, 53(5):517–527, 2011.

[42] B. Hannaford and J.H. Ryu. Time-domain passivity control of haptic interfaces. *IEEE Transactions on Robotics and Automation*, 18(1):1–10, 2002.

[43] T. Hatanaka, N. Chopra, and M. Fujita. Passivity-based bilateral human-swarm-interactions for cooperative robotic networks and human passivity analysis. In *Proceedings of 54th IEEE Conference on Decision and Control (CDC)*, pages 1033–1039. IEEE, 2015.

[44] S. Hayati and S.T. Venkataraman. Design and implementation of a robot control system with traded and shared control capability. In *Robotics and Automation, 1989. Proceedings., 1989 IEEE International Conference on*, pages 1310–1315. IEEE, 1989.

[45] D. Hill and P. Moylan. The stability of nonlinear dissipative systems. *IEEE Transactions on Automatic Control*, 21(5):708–711, 1976.

[46] S. Hirche and M. Buss. Human-oriented control for haptic teleoperation. *Proceedings of the IEEE*, 100(3):623–647, 2012.

[47] A.M. Howard. Role allocation in human-robot interaction schemes for mission scenario execution. In *Proceedings of IEEE International Conference on Robotics and Automation (ICRA)*, pages 3588–3594. IEEE, 2006.

[48] M.D. Hua, T. Hamel, P. Morin, and C. Samson. A control approach for thrust-propelled underactuated vehicles and its application to vtol drones. *IEEE Transactions on Automatic Control*, 54(8):1837–1853, 2009.

[49] M. Itoh and K. Tanaka. Mathematical modeling of trust in automation: Trust, distrust, and mistrust. In *Proceedings of the Human Factors and Ergonomics Society Annual Meeting*, volume 44, pages 9–12. SAGE Publications, 2000.

[50] J.Y. Jian, A.M. Bisantz, and D.G. Drury. Foundations for an empirically determined scale of trust in automated systems. *International Journal of Cognitive Ergonomics*, 4(1):53–71, 2000.

[51] D.R. Olsen Jr and S.B. Wood. Fan-out: Measuring human control of multiple robots. In *Proceedings of the SIGCHI conference on Human factors in computing systems*, pages 231–238. ACM, 2004.

[52] D.B. Kaber and M.R. Endsley. Out-of-the-loop performance problems and the use of intermediate levels of automation for improved control system functioning and safety. *Process Safety Progress*, 16(3):126–131, 1997.

[53] W. Kool, J.T. McGuire, Z.B. Rosen, and M.M. Botvinick. Decision making and the avoidance of cognitive demand. *Journal of Experimental Psychology: General*, 139(4):665–682, 2010.

[54] D. Kortenkamp, R.P. Bonasso, D. Ryan, and D. Schreckenghost. Traded control with autonomous robots as mixed initiative interaction. In *AAAI Symposium on Mixed Initiative Interaction*, 1997.

[55] T. Krajník, V. Vonásek, D. Fišer, and J. Faigl. Ar-drone as a platform for robotic research and education. In *International Conference on Research and Education in Robotics*, pages 172–186. Springer, 2011.

[56] M.G. Lagoudakis, M. Berhault, S. Koenig, P. Keskinocak, and A.J. Kleywegt. Simple auctions with performance guarantees for multi-robot task allocation. In *Proceedings of IEEE/RSJ International Conference on Intelligent Robots and Systems.(IROS)*, volume 1, pages 698–705. IEEE, 2004.

[57] P. Lally and B. Gardner. Promoting habit formation. *Health Psychology Review*, 7(sup1):S137–S158, 2013.

[58] T.M Lam, H.W. Boschloo, M. Mulder, and M.M. Van Paassen. Artificial force field for haptic feedback in uav teleoperation. *IEEE Transactions on Systems, Man and Cybernetics, Part A: Systems and Humans*, 39(6):1316–1330, 2009.

[59] D. Lee and M.W. Spong. Bilateral teleoperation of multiple cooperative robots over delayed communication networks: Theory. In *Proceedings of IEEE International Conference on Robotics and Automation (ICRA)*, pages 360–365. IEEE, 2005.

[60] D. Lee and D. Xu. Feedback r-passivity of lagrangian systems for mobile robot teleoperation. In *IEEE International Conference on Robotics and Automation (ICRA)*, pages 2118–2123. IEEE, 2011.

[61] J. Lee and N. Moray. Trust, self-confidence and supervisory control in a process control simulation. In *Systems, Man, and Cybernetics, 1991.'Decision Aiding for Complex Systems, Conference Proceedings., 1991 IEEE International Conference on*, pages 291–295. IEEE, 1991.

[62] J. Lee and N. Moray. Trust, control strategies and allocation of function in human-machine systems. *Ergonomics*, 35(10):1243–1270, 1992.

[63] J.D. Lee and N. Moray. Trust, self-confidence, and operators' adaptation to automation. *International journal of human-computer studies*, 40(1):153–184, 1994.

[64] P. Leitão. Agent-based distributed manufacturing control: A state-of-the-art survey. *Engineering Applications of Artificial Intelligence*, 22(7):979–991, 2009.

[65] J.R. Lewis. Ibm computer usability satisfaction questionnaires: Psychometric evaluation and instructions for use. *International Journal of Human-Computer Interaction*, 7(1):57–78, 1995.

[66] Z. Li, L. Ding, H. Gao, G. Duan, and C.Y. Su. Trilateral teleoperation of adaptive fuzzy force/motion control for nonlinear teleoperators with communication random delays. *IEEE Transactions on Fuzzy Systems*, 21(4):610–624, 2013.

[67] G. Liu. Control of robot manipulators with consideration of actuator performance degradation and failures. In *IEEE International Conference on Robotics and Automation (ICRA)*, volume 3, pages 2566–2571. IEEE, 2001.

[68] S.G. Loizou and V. Kumar. Mixed initiative control of autonomous vehicles. In *IEEE International Conference on Robotics and Automation*, pages 1431–1436. IEEE, 2007.

[69] R. Lozano, N. Chopra, and M.W. Spong. Passivation of force reflecting bilateral teleoperators with time varying delay. In *Proceedings of the 8. Mechatronics Forum*, pages 954–962. Citeseer, 2002.

[70] S.M. Merritt and D.R. Ilgen. Not all trust is created equal: Dispositional and history-based trust in human-automation interactions. *Human Factors: The Journal of the Human Factors and Ergonomics Society*, 50(2):194–210, 2008.

[71] A.I. Mouaddib. Controlling and sharing authority in a multi-robot system. In *Proceedings of the first conference on Humans Operating Unmanned Systems (HUMOUS08)*, 2014.

[72] G. Niemeyer, C. Preusche, and G. Hirzinger. Telerobotics. In *Springer handbook of robotics*, pages 741–757. Springer, 2008.

[73] G. Niemeyer and J.J.E. Slotine. Stable adaptive teleoperation. *IEEE Journal of Oceanic Engineering*, 16(1):152–162, 1991.

[74] S. Nikolaidis and J. Shah. Human-robot cross-training: Computational formulation, modeling and evaluation of a human team training strategy. In *Proceedings of the 8th ACM/IEEE international conference on Human-robot interaction*, pages 33–40. IEEE Press, 2013.

[75] R. Pak, N. Fink, M. Price, B. Bass, and L. Sturre. Decision support aids with anthropomorphic characteristics influence trust and performance in younger and older adults. *Ergonomics*, 55(9):1059–1072, 2012.

[76] R. Parasuraman, M. Barnes, K. Cosenzo, and S. Mulgund. Adaptive automation for human-robot teaming in future command and control systems. Technical report, DTIC Document, 2007.

[77] R. Parasuraman, M. Mouloua, and B. Hilburn. Adaptive aiding and adaptive task allocation enhance human-machine interaction. *Automation technology and human performance: Current research and trends*, pages 119–123, 1999.

[78] R. Parasuraman and V. Riley. Humans and automation: Use, misuse, disuse, abuse. *Human Factors: The Journal of the Human Factors and Ergonomics Society*, 39(2):230–253, 1997.

[79] C. Passenberg, A. Glaser, and A. Peer. Exploring the design space of haptic assistants: the assistance policy module. *IEEE Transactions on Haptics*, 6(4):440–452, 2013.

[80] J. Philips, J.D.R Millán, G. Vanacker, E. Lew, F. Galán, P.W. Ferrez, H.V. Brussel, and M. Nuttin. Adaptive shared control of a brain-actuated simulated wheelchair. In *IEEE 10th International Conference on Rehabilitation Robotics (ICORR)*, pages 408–414. IEEE, 2007.

[81] C. Phillips-Grafflin, H.B. Suay, J. Mainprice, N. Alunni, D. Lofaro, D. Berenson, S. Chernova, R.W. Lindeman, and P. Oh. From autonomy to cooperative traded control of humanoid manipulation tasks with unreliable communication. *Journal of Intelligent & Robotic Systems*, 82(3-4):341–361, 2016.

[82] S.M.M. Rahman, B. Sadrfaridpour, and Y. Wang. Trust-based optimal subtask allocation and model predictive control for human-robot collaborative assembly in manufacturing. In *ASME 2015 Dynamic Systems and Control Conference*, pages V002T32A004–V002T32A004. American Society of Mechanical Engineers, 2015.

[83] B. Sadrfaridpour, J. Burke, and Y. Wang. Human and robot collaborative assembly manufacturing: Trust dynamics and control. In *RSS 2014 Workshop on Human-Robot Collaboration for Industrial Manufacturing*, 2014.

[84] B. Sadrfaridpour, H. Saeidi, Y. Wang, and J. Burke. Modeling and control of trust in human and robot collaborative manufacturing. In *AAAI Spring Symposium Series*, 2014.

[85] H. Saeidi, F. McLane, B. Sadrfaridpour, E. Sand, S. Fu, J. Rodriguez, J.R. Wagner, and Y. Wang. Trust-based mixed-initiative bilateral teleoperation of mobile robotic systems. In *American Control Conference*, pages 6177–6182. IEEE, 2016.

[86] H. Saeidi and Y. Wang. Trust and self-confidence based autonomy allocation of robotic systems. In *Proceedings of 54th IEEE Conference on Decision and Control (CDC)*, pages 6052–6057. IEEE, 2015.

[87] L.V. Santanao, A.S. Brandao, M. Sarcinelli-Filho, and R. Carelli. A trajectory tracking and 3d positioning controller for the ar. drone quadrotor. In *Unmanned Aircraft Systems (ICUAS), 2014 International Conference on*, pages 756–767. IEEE, 2014.

[88] K. Savla and E. Frazzoli. A dynamical queue approach to intelligent task management for human operators. *Proceedings of the IEEE*, 100(3):672–686, 2012.

[89] C. Secchi, S. Stramigioli, and C. Fantuzzi. Intrinsically passive force scaling in haptic interfaces. In *IEEE/RSJ International Conference on Intelligent Robots and Systems*, pages 2121–2126. IEEE, 2006.

[90] C. Secchi, S. Stramigioli, and C. Fantuzzi. *Control of Interactive Robotic Interfaces: A Port-Hamiltonian Approach*, volume 29. Springer Science & Business Media, 2007.

[91] B. Sellner, F.W. Heger, L.M. Hiatt, R. Simmons, and S. Singh. Coordinated multiagent teams and sliding autonomy for large-scale assembly. *Proceedings of the IEEE*, 94(7):1425–1444, 2006.

[92] T. Setter, H. Kawashima, and M. Egerstedt. Team-level properties for haptic human-swarm interactions. In *2015 American Control Conference (ACC)*, pages 453–458. IEEE, 2015.

[93] T.B. Sheridan. Adaptive automation, level of automation, allocation authority, supervisory control, and adaptive control: Distinctions and modes of adaptation. *IEEE Transactions on Systems, Man and Cybernetics, Part A: Systems and Humans*, 41(4):662–667, 2011.

[94] S. Sirouspour and P. Setoodeh. Multi-operator/multi-robot teleoperation: an adaptive nonlinear control approach. In *IEEE/RSJ International Conference on Intelligent Robots and Systems (IROS)*, pages 1576–1581. IEEE, 2005.

[95] J.J.E Slotine and W. Li. *Applied Nonlinear Control*, volume 199. Prentice-hall Englewood Cliffs, NJ, 1991.

[96] J. Smisek, W. Mugge, J.B.J. Smeets, M.M. van Paassen, and A. Schiele. Adapting haptic guidance authority based on user grip. In *IEEE International Conference on Systems, Man and Cybernetics (SMC)*, pages 1516–1521. IEEE, 2014.

[97] D.A. Spencer and Y. Wang. Slqr suboptimal human-robot collaborative guidance and navigation for autonomous underwater vehicles. In *2015 American Control Conference (ACC)*, pages 2131–2136. IEEE, 2015.

[98] J.G. Storms and D.M. Tilbury. Blending of human and obstacle avoidance control for a high speed mobile robot. In *American Control Conference (ACC)*, pages 3488–3493. IEEE, 2014.

[99] K. Tervo. Human adaptive mechatronics methods for mobile working machines. 2010.

[100] A. Tversky and D. Kahneman. Judgment under uncertainty: Heuristics and biases. In *Utility, probability, and human decision making*, pages 141–162. Springer, 1975.

[101] C. Urdiales, A. Poncela, I. Sanchez-Tato, F. Galluppi, M. Olivetti, and F. Sandoval. Efficiency based reactive shared control for collaborative human/robot navigation. In *2007 IEEE/RSJ International Conference on Intelligent Robots and Systems*, pages 3586–3591. IEEE, 2007.

[102] http://gazebosim.org.

[103] http://humansystems.arc.nasa.gov/groups/tlx/.

[104] http://www.mathworks.com/products/sysid/.

[105] http://www.ros.org/.

[106] F.M.F. Verberne, J. Ham, and C.J.H. Midden. Trust in smart systems sharing driving goals and giving information to increase trustworthiness and acceptability of smart systems in cars. *Human Factors: The Journal of the Human Factors and Ergonomics Society*, 54(5):799–810, 2012.

[107] X. Wang, Z. Shi, F. Zhang, and Y. Wang. Mutual trust based scheduling for (semi)autonomous multi-agent systems. In *2015 American Control Conference (ACC)*, pages 459–464. IEEE, 2015.

[108] Y. Wang. Regret-based bayesian sequential decision-making for human-agent collaborative search tasks. In *American Control Conference (ACC)*, pages 5738–5743. IEEE, 2015.

[109] Y. Wang. Regret-based automated decision-making aids for domain search tasks using human-agent collaborative teams. *IEEE Trans. on Control Systems Technology*, PP(99):1–16, 2016.

[110] Y. Wang, Z. Shi, C. Wang, and F. Zhang. Human-robot mutual trust in (semi)autonomous underwater robots. In *Cooperative Robots and Sensor Networks*, pages 115–137. Springer, 2014.

[111] R. Wegner and J. Anderson. Agent-based support for balancing teleoperation and autonomy in urban search and rescue. *International Journal of Robotics and Automation*, 21(2):120–128, 2006.

[112] J. Wise, A. Rio, and M. Fedouach. What really happened aboard air france 447. *Popular Mechanics*, 6, 2011.

[113] D.H. Won, S. Chun, S. Sung, T. Kang, and Y.J. Lee. Improving mobile robot navigation performance using vision based slam and distributed filters. In *International Conference on Control, Automation and Systems (ICCAS)*, pages 186–191. IEEE, 2008.

[114] H.W. Wopereis, M. Fumagalli, S. Stramigioli, and R. Carloni. Bilateral human-robot control for semi-autonomous uav navigation. In *Intelligent Robots and Systems (IROS), 2015 IEEE/RSJ International Conference on*, pages 5234–5240. IEEE, 2015.

[115] A. Xu and G. Dudek. Trust-driven interactive visual navigation for autonomous robots. In *IEEE International Conference on Robotics and Automation (ICRA)*, pages 3922–3929. IEEE, 2012.

[116] A. Xu and G. Dudek. Optimo: Online probabilistic trust inference model for asymmetric human-robot collaborations. In *Proceedings of the Tenth Annual ACM/IEEE International Conference on Human-Robot Interaction*, pages 221–228. ACM, 2015.

[117] R.M. Yerkes and J. Dodson. The relation of strength of stimulus to rapidity of habit-formation. *Journal of comparative neurology and psychology*, 18:459–482, 1908.

[118] J. Zhao and D.J. Hill. Dissipativity theory for switched systems. *IEEE Transactions on Automatic Control*, 53(4):941–953, 2008.